

SILICON NANOCRYSTALS: OPTICAL PROPERTIES AND SELF-ASSEMBLY

A Dissertation
Submitted to the Graduate Faculty
of the
North Dakota State University
of Agriculture and Applied Science

By

Samuel Lynn Brown

In Partial Fulfillment of the Requirements
for the Degree of
DOCTOR OF PHILOSOPHY

Major Program:
Materials and Nanotechnology

March 2018

Fargo, North Dakota

North Dakota State University
Graduate School

Title

SILICON NANOCRYSTALS: OPTICAL PROPERTIES AND SELF-
ASSEMBLY

By

Samuel Lynn Brown

The Supervisory Committee certifies that this *disquisition* complies with North Dakota
State University's regulations and meets the accepted standards for the degree of

DOCTOR OF PHILOSOPHY

SUPERVISORY COMMITTEE:

Erik Hobbie

Chair

Alan Denton

Yongki Choi

Svetlana Kilina

Seth Rasmussen

Approved:

4/10/18

Date

Erik Hobbie

Department Chair

ABSTRACT

Silicon nanocrystal's (SiNCs) size dependent optical properties and nontoxic nature portend potential applications across a broad range of industries. With any of these applications, a thorough understanding of SiNC photophysics is desirable to tune their optical properties while optimizing quantum yield. However, a detailed understanding of the photoluminescence (PL) from SiNCs is convoluted by the complexity of the decay mechanisms, including a stretched-exponential relaxation and the presence of both nanosecond and microsecond decays.

In this dissertation, a brief history of semiconductor nanocrystals is given, leading up to the first discovery of room temperature PL in SiNCs. This is then followed by an introduction to the various nanocrystal synthetic schemes and a discussion of quantum dot photophysics in general. Three different studies on the PL from SiNCs are then presented. In the first study, the stretched nature of the time dependent PL is analyzed *via* chromatically-resolved and full-spectrum PL decay measurements. The second study analyzes the size dependence of the bimodal PL decay, where the amplitude of the nanosecond and microsecond decay are related to nanocrystal size, while the third project analyzes the temperature and microstructure dependencies of the PL from SiNC solids.

After an indepth look at the PL from SiNCs, this report examines preliminary results of SiNC and silver nanocrystal self-assembly. When compared to metal and metal chalcogenide nanoparticles, there is a dearth of literature on the self-assembly of SiNCs. To understand these phenomena, we analyze the size dependent ability of SiNCs to form a 'superlattice' and compare this with silver nanocrystals. Although the results on self-assembly are still somewhat preliminary, it appears that factors such as SiNC concentration and size dispersity play a key role in SiNC self-

assembly, while suggesting intrinsic differences between the self-assembly of SiNCs and silver nanocrystals.

Finally, at the end of this dissertation, a corollary project is presented on the computational analysis of fluorescent silver nanoclusters (AgNCs). Due to their small size and non-toxic nature, AgNCs are an ideal fluorophore for biological systems, yet there is a limited understanding of their photophysics, which is the focus of this part of the dissertation.

ACKNOWLEDGEMENTS

The work contained within this dissertation would not have been possible without the guidance, patience, and help of Dr. Erik Hobbie. He has been a great resource and has always been in my corner in any situation. He has given me direction in my research and has pushed me throughout the process. I'm thankful for the all that he has done.

During this time, I have met many great colleagues and friends and without their support this would have been a significantly less enjoyable time. Joe Miller mentored me through the first year of my doctoral work, guiding me though the ins and out of the lab, while also teaching me the important nuances of sand volleyball, softball, tennis, and racquetball. Thanks to Ahmed Elbaradei for the time studying together as well as teaching me about the finer things in life such as photography and diverse philosophical and cultural perspectives. Thanks to Matt Semler for the help with g-code, laser cutting, and mask making and to Damith Roziaro for helping me with any of my fluid dynamics questions and experimental set-ups. Thanks to the both of you for teaching me the 'trivial' things in physics and for all the racquetball and Settlers of Catan® games. Thanks to Anthony Clay for the fruitful chemistry discussion and always being a point of contact for any synthetic or general chemistry questions. Thanks to Maria Goriacheva for working through the growing pains of nanoparticle synthesis while teaching me a little bit of Russian along the way. I would also like to thank Tim Twohig, Theresa Elder and Jaime Froberg for always being willing to discuss how the Broncos were better than the Packers...

Computational work is scattered throughout this report and I would like to thank the many collaborators for their help and contributions, particularly Dmitri Kilin for giving me a glimpse inside the black box of computational chemistry. I would also like to thank Scott Payne for his help with all aspects of electron microscopy, as well as the other members of the Materials and

Nanotechnology Program. I would also like to thank the members of my doctoral committee for the guidance and help they have given me along the way. And most importantly, I would like to give all the credit to God for,

“I can do all things through Christ who strengthens me.” -- Philippians 4:13

DEDICATION

This work is dedicated to my wife Lisa for putting up with me through the ups and downs of life while being my suga' mama during this time. And to Cooper, the little pain in my butt that was always wagging his butt when I came home to see him.

TABLE OF CONTENTS

ABSTRACT.....	iii
ACKNOWLEDGEMENTS.....	v
DEDICATION.....	vii
LIST OF TABLES.....	xii
LIST OF FIGURES.....	xiii
LIST OF ABBREVIATIONS.....	xxiii
LIST OF APPENDIX FIGURES.....	xxvi
CHAPTER 1. INTRODUCTION TO NANOPARTICLES AND NANOTECHNOLOGY.....	1
1.1. Introduction.....	1
1.2. History of Nanotechnology.....	2
1.3. What are Quantum Dots.....	4
1.4. Applications of Quantum Dots.....	6
1.4.1. Quantum Dot Solar Cells.....	7
1.4.2. Light Emitting Diodes and Displays.....	10
1.4.3. Fluorescent Biomarkers and Sensors.....	11
1.5. Toxicity and Environmental Concerns.....	13
1.6. Silicon Nanocrystals.....	15
CHAPTER 2. SILICON NANOCRYSTAL SYNTHESIS, PASSIVATION, AND SIZE SEPARATION.....	17
2.1. Introduction.....	17
2.2. Silicon Nanocrystal Synthesis.....	17
2.2.1. Non-Thermal Plasma Synthesis.....	18
2.2.2. Silicon Suboxide Anneal Synthesis.....	19

2.2.3. Reverse Micelle Synthesis	20
2.3. Passivation	21
2.4. Size Separation.....	23
CHAPTER 3. QUANTUM DOT PHYSICS	27
3.1. Introduction.....	27
3.2. Particle-in-a-Box.....	27
3.3. Particle in a Periodic Potential.....	29
3.4. Multi-Electron Systems	31
CHAPTER 4. ON THE ORIGIN OF THE STRETCHED EXPONENTIAL PHOTOLUMINESCENCE RELAXATION IN SIZE SEPARATED SILICON NANOCRYSTALS.....	35
4.1. Introduction.....	35
4.2. Results and Discussion	37
4.3. Conclusion	48
4.4. Experimental Methods.....	49
CHAPTER 5. SIZE DEPENDENT BIMODAL DECAY IN SILICON NANOCRYSTALS	52
5.1. Introduction.....	52
5.2. Results and Discussion	52
5.3. Conclusion	60
5.4. Experimental Methods.....	60
CHAPTER 6. MICROSTRUCTURE AND TEMPERTURE DEPENDENCE IN SILICON NANOCRYSTAL PHOTOLUMINESCENCE.....	62
6.1. Introduction.....	62
6.2. Results.....	62
6.3. Discussion	64

6.4. Conclusion	69
6.5. Experimental Methods	70
CHAPTER 7. NANOPARTICLE SUPERLATTICE: PRELIMINARY RESULTS.....	71
7.1. Introduction.....	71
7.2. Materials and Methods.....	73
7.3. Preliminary Results: Silver Nanoparticles	76
7.4. Preliminary Results: Silicon Nanocrystals.....	82
7.5. Discussion and Future Outlook.....	92
CHAPTER 8. SUPPLEMENTAL PROJECT: A COMPUTATIONAL STUDY ON THE FLUORESCENCE OF SILVER NANOCCLUSERS	95
8.1. Introduction.....	95
8.2. Methods.....	96
8.3. Results.....	100
8.4. Discussion	109
8.5. Conclusions.....	112
REFERENCES	114
APPENDIX A. EQUIPMENT	138
A1. Upright Microscope	138
A2. Inverted Microscope	140
A3. Ultracentrifuge	142
A4. 3D Printers	143
A5. Linear Variable Filters	144
A6. Excitation Source	144
A7. Detector	145

APPENDIX B. METHODS AND PROCEDURES	147
B1. Photoluminescence Measurement	147
B2. Lifetime Measurement	148
B3. Quantum Yield Measurement	149
B4. Preparation of a Self-Assembled Monolayer	151
B5. Density Gradient Ultracentrifugation.....	153
APPENDIX C. MATHEMATICA DISCRETE EXPONENTIAL CODE	156

LIST OF TABLES

<u>Table</u>	<u>Page</u>
4.1. Solvent and Corresponding Quantum Yield.	39
7.1. Duration and Rotor Speed for Each Nanoparticle Separation.	83
8.1. Representative inter-band excitations under independent orbital approximation represented by pairs of occupied (hole) and unoccupied (electron) orbitals.	105

LIST OF FIGURES

<u>Figure</u>	<u>Page</u>
1.1. Timeline of Nanotechnology	2
1.2. Nanoparticles have been used in ancient instruments throughout time. Damascus blacksmiths were able to create strong and light (a) ‘Damascus saber blades’ that had aligned carbon nanotubes in the blade. Reprinted from Ref. [10] with permission from Springer Nature. In ancient Rome, gold and silver nanoparticles were created in situ in the Lycurgus Cup of Rome. (b) Light reflected from this cup would appear opaque green while (c) transmitted light would be scattered due to the embedded plasmonic nanoparticles giving the cup a translucent red appearance. © Trustees of the British Museum.....	3
1.3. Quantum dots of increasing size will emit, when properly excited, with increasingly lower energy photons due to the quantum confinement effect. Quantum dots above were produced by PlasmaChem and are reprinted under the Creative Commons Attribution-Share Alike 3.0 Unported License.....	4
1.4. Typically, a quantum dot or nanoparticle consists of two main components, the inorganic core and the outer ligand layer. The size of the inorganic core is used to control various optical properties while the ligand is most typically used to invoke colloidal stability. In some cases, an inorganic shell can cap the inorganic core to help improve optical properties or to limit the toxic effects of the core. Panel (b) shows a model nanoparticle with a core (black), shell (gray), and ligand layer, while (a) shows a transmission electron micrograph of two silicon nanocrystals on a graphene substrate, where one can see both the crystalline planes of the silicon atoms as well as the brush-like layer of the ligands surrounding the nanoparticles. Reprinted with permission from Ref. [28].....	5
1.5. Nanoparticles can be used in several applications ranging from energy capture to biological markers. In panel (a), quantum dots are used as a solar cell collector to gather light from a window and direct it to an inline photovoltaic. Reprinted with permission from Ref. [48]. (b) Nanoparticles with the appropriate passivation are attached to different parts of the cell, demonstrating their applicability as biomarkers. Reprinted with permission from Ref. [57]. (c) Typical monocrystalline solar cells with a band gap of approximately 1.1 eV can only achieve an overall efficiency of 33 %. Quantum dot solar cells on the other hand, due to the confined nature of the exciton, can excite two electrons into the valance band, through a process known as multiple exciton generation, effectively doubling the possible overall efficiency. In (d), PbS quantum dots are shown to have external quantum efficiencies greater than 100 %, indicative of multiple exciton generation in these devices. Reprinted with permission from Ref. [38].....	6

1.6.	The synthesis and self-assembly of nanoparticles, or superlattice development, both play a significant role in the performance of devices such as a quantum dot solar cell, field effect transistor, or light emitting diode. This inherently allows for several degrees a freedom in fabrication methods and tunability in the corresponding device.	8
1.7.	(a) A typical bulk heterojunction organic photovoltaic device consists of a positive and negative electrode, a hole transport layer and electron transport layer, as well as the active layer. Plasmonic nanoparticles can be incorporated into the (b) active layer, (c) hole transport layer, and at (d) the interface of the hole-transport layer and the active layer.	9
1.8.	The size tunable Gaussian emission of quantum dots makes them ideal candidates for applications in light emitting diodes and displays. The photoluminescence and electroluminescence of size separated silicon nanocrystals are compared (a) while the stacked light emitting device is shown in (b). (a) and (b) are reprinted with permission from Ref. [56] (c) Quantum dots can be found in commercial displays such as the Samsung QLED TV. Typically a blue light-emitting diode is used to drive fluorescence in a layer of quantum dots to achieve the high-quality display.	11
1.9.	Silver nanoclusters have been shown to be ideal candidates for biological markers and sensors. The small size is ideal for intracellular transport while the photoluminescence is strong but highly sensitive to the surrounding environment. (a) Representation of a silver nanocluster with twelve cytosine molecules complexed to the surface while (b) shows the increase in photoluminescence of DNA complexed silver nanoclusters when they are hybridized with the appropriate target. (a) and (b) are reprinted with permission from Ref. [80] and Ref. [79], respectively.	12
1.10.	Many nanoparticles can present toxicity concerns. (a) In Michael Crichton’s book, Prey, he describes the tale of rogue nanoparticle robots terrorizing any living thing within reach. (b) The small size of nanoparticles allows for cellular uptake and decomposition inside the cell membrane. This highly localized concentration of ions can then be toxic to the cell. Reprinted from Ref. [96] with permission from Elsevier.	13
1.11.	Images of mouse stomach after a single oral gavage for 24 h of (a) nano-sized copper (b) micro-sized copper (c) ionic-sized copper and (d) no copper. The mouse that digested nanosized copper shows clear discoloration and swelling. Reprinted from Ref. [92] with permission from Elsevier.	15

2.1.	The synthesis of silicon nanocrystals can be done using a non-thermal plasma of silane and argon gas. (a) The apparatus used to make these nanocrystals is a quartz tube fitted with a vacuum line on the downstream end and a gas inlet line on the upstream end. Two leads of a radio frequency generator wrapped around the tube are used to generate the non-thermal plasma. (b) The product of this methods is crystalline silicon nanocrystals with diameters of approximately 3 to 4 nm (scale bar is 1 nm). Reprinted with permission from Ref. [106]. Copyright 2018 American Chemical Society	18
2.2.	The decomposition of a silicon suboxide precursor such as commercially available hydrogen silsesquioxane is used to produce monodisperse silicon nanocrystals. The silicon suboxide is first annealed at temperatures in excess of 1100 °C to decompose it into silicon nanocrystals encased in silicon dioxide. This silicon nanocrystal/silicon dioxide composite is then mechanically milled and etched in hydrofluoric acid to liberate the silicon nanocrystals. The extracted nanocrystals are then passivated, typically with short carbon chains. Reprinted with permission from Ref. [136]......	20
2.3.	Blue emitting SiNCs can be synthesized via a one pot synthetic scheme. (a) Silicon tetrachloride (black circle) and hexyltrichlorosilane (blue circle) create a (b) reverse micelle in toluene. The addition of a lithium aluminum halide reduces the silicon tetrachloride core creating (c) a silicon quantum dot. (d)-(e) These silicon quantum dots have blue photoluminescence typical of the single pot synthetic methods.....	21
2.4.	Nanoparticles can be separated by size or density through density gradient ultracentrifugation using differential centrifugation, rate-zonal centrifugation, or isopycnic centrifugation.....	25
2.5.	(a) The photoluminescence of silicon nanocrystals separated using density gradient ultracentrifugation with larger nanocrystals exhibiting red shifted gaussian photoluminescence. (b) To separate the as produced silicon nanocrystals, they are placed on top of a density gradient where, during ultracentrifugation, the nanocrystals move down the centrifuge tube. The nanocrystal terminal velocity is quadratically related to the nanoparticle radius, which is exploited to separate the nanoparticles based on size. (c) After the nanocrystals are size separated they are extracted layer by layer using a homemade jig.....	26
3.1.	Model of a particle-in-a-box with infinite potentials outside the box and zero potential inside	27
3.2.	The solution to the particle-in-a-box model results in a (a) simple sinusoidal wavefunction and (b) discrete energy levels.....	29
3.3.	Periodic potential model.	30

3.4.	(a) The function $P \frac{\sin(\alpha a)}{\alpha a} + \cos(\alpha a)$ versus αa , where any value of this function that is between -1 and 1 is plotted in blue. (b) Energy bands form from this periodic potential model.	31
3.5.	The coordinates of a helium atom with the nucleus at the origin.	32
3.6.	Algorithmic flow chart for the Hartree-Fock Method.	33
4.1.	QY of as produced SiNCs in various solvents, where the inset shows the QY in hexane (H), THF (T) and then in hexane (H) again, with the vertical axis normalized to the initial QY in hexane. (b) QY as a function of donor number for SiNCs dispersed in several different solvents. The inset is a TEM image of a single nanocrystal (scale bar is 2 nm). (c) The QY of size separated ‘super fractions’ as a function nanocrystal size and peak emission wavelength (inset). (d) PL spectrum of each super fraction.	38
4.2.	(a) Full-spectrum and spectrally resolved photoluminescence decay measurements of fraction SI fit with a single stretched exponential decay. (b) The same spectrally resolved decay from (a) with an expanded time scale. The full-spectrum and spectrally resolved photoluminescence lifetime (c) and stretching exponent (d) for each super-fraction plotted as a function of peak emission wavelength (note the curves are quadratic fits).....	42
4.3.	(a) Probability distribution functions for $\alpha = 0.6$ to $\alpha = 0.8$ increasing by increments of 0.05 in the direction of the red arrow. (b) Comparison of $I_{\text{cont}}(t)$ (solid lines) and $I_{\text{disc}}(t)$ (dashed lines) for $\alpha = 0.6$ and $\alpha = 0.8$ with lifetime values interpolated from the quadratic fits in Figure 4.2	44
4.4.	(a) Decay curve $I_{\text{disc}}(t)$ computed for $\alpha = 0.6$. The color-coded (yellow to blue) curves are the corresponding contributions from each lifetime in the distribution, which is shown both in terms of (b) dimensionless rate and (c) lifetime. (d)-(f) A similar set of plots for $\alpha = 0.8$. The vertical lines correspond to the values of τ_{str} indicated in Figure 4.3	45
4.5.	Full-spectrum probability distributions (solid black curves) and spectrally resolved probability distribution functions (red curves) for (a) $\alpha = 0.60$, (b) 0.65, (c) 0.70, (d) 0.75, and (e) 0.80. The vertical blue and green dashed lines represent τ_{str} and the cutoff, respectively. The shaded region is the portion used to approximate the SR data from the full distribution.	46
4.6.	(a) $I_{\text{cont}}(t)$ from the spectrally resolved data (solid blue line) and $I_{\text{disc}}(t)$ from the full-spectrum data with lower limit cutoffs applied (dashed black line). (b) The lower limit cutoffs used in (a).	47

4.7.	(a) Most probable photoluminescence lifetime for the resolved (gray curve) and full-spectrum (blue curve) data along with τ_{STR} from Figure 4.2c (black dashed curves). (b) The quantum yield for each fraction and the most probable lifetime for the full-spectrum data (green dashed line).....	47
4.8.	(a) Photoluminescence spectrum of fraction SF (black) and the three spectrally resolved regions used to measure photoluminescence relaxation. (b) The probability distribution function extracted from the stretched exponential relaxation based on the full spectrum (black), the ‘blue’ region (blue, $\alpha = 0.6$), the ‘peak’ region (green, $\alpha = 0.83$) and the ‘red’ region (red, $\alpha = 0.86$).....	49
5.1.	Room temperature (a) photoluminescence and (b) photoluminescence relaxation of size-separated, plasma-synthesized silicon nanocrystals with the (c) peak emission as a function of fraction number. A transmission electron micrograph of a plasma synthesized silicon nanocrystal can be seen in the inset of (c) with a scale bar of 1 nm. Reprinted with permission from Ref. [186]. Copyright 2018 American Chemical Society.	53
5.2.	The photoluminescence relaxation fitting parameters of size-separated silicon nanocrystals based on Eq. 5.1 , with the (a) fast and slow lifetimes and the (b) fast and slow amplitudes. The (c) quantum yield, slow decay lifetime and slow decay amplitude plotted as a function of size. Reprinted with permission from Ref. [186]. Copyright 2018 American Chemical Society.	54
5.3.	(a) The amplitude of the fast decay has a strong dependence on size with (b) the ratio of the fast to slow amplitude having an exponential relationship with size. Reprinted with permission from Ref. [186]. Copyright 2018 American Chemical Society.....	54
5.4.	The temperature dependent photoluminescence spectra of (a) the small and (b) large silicon nanocrystals with the corresponding temperature dependent photoluminescence decay of (c) the small and (d) large samples. (e) The slow microsecond decay contributes most of the total emission regardless of size or temperature. Reprinted with permission from Ref. [186]. Copyright 2018 American Chemical Society.	56
5.5.	(a) Photoluminescence relaxation lifetimes of the ‘small’ and ‘large’ samples at -80 °C, (b) the temperature dependent amplitudes of the slow and fast decay and (c) their corresponding ratio. Reprinted with permission from Ref. [186]. Copyright 2018 American Chemical Society.	57

5.6.	(a) DFT derived phonon density of states for two different sized silicon nanocrystals with the corresponding electronic density of states for the (b) small and (c) large silicon nanocrystal. Note: the green and red colored electronic density of states are calculated with and without electron hole interactions, respectively. Reprinted with permission from Ref. [186]. Copyright 2018 American Chemical Society.....	58
5.7.	(a) Illustration of the proposed mechanism for exciton recombination with a resonant fast (yellow) and a non-resonant slow (red) decay. (b) An energy diagram of the proposed model where recombination via Kasha's rule is artificially blocked to mimic the long lifetime associated with the indirect band gap. Modeled photoluminescence relaxation curves at a temperature of (c) $T = 0.025$ eV and (d) $T = 0.010$ eV. Note the key in (d) corresponds to room temperature quantum yield. (e) Measured and calculated photoluminescence relaxation amplitudes of the fast and slow decay as a function of size. The calculated amplitudes are shown at two different temperatures (solid: $T = 0.025$ eV; dashed: $T = 0.010$ eV). Reprinted with permission from Ref. [186]. Copyright 2018 American Chemical Society.	59
6.1.	(a) The photoluminescence of size separated silicon nanocrystal fractions (solid) and the photoluminescence of the as-produced parent (dashed). (b) Transmission electron micrograph of a single nanocrystal (top; scale bar is 1 nm) and an ensemble of silicon nanocrystals (bottom). Reprinted with permission from Ref. [108]. Copyright 2018 American Chemical Society.	63
6.2.	(a) The time dependent photoluminescence of a 'small' and 'large' diameter fraction measured at 193 K. The inset shows the photoluminescence lifetime of the small and large fraction as a function of temperature. (b) The maximum photoluminescence intensity as a function of temperature for several size-separated fractions with the inset showing the corresponding lifetime as a function of peak emission. (c) An optical micrograph showing a (left) drop cast silicon nanocrystal ensemble prior to (right) crack formation. Note the temperature in the top left corner of each micrograph. (d) The cracks that formed in the larger diameter nanocrystal ensembles would persist even when cycled back to room temperature allowing for atomic force microscopy images to be taken. Taken with permission from Ref. [108]. Copyright 2018 American Chemical Society.....	64
6.3.	(a) The temperature dependent photoluminescence of the 'small' sample showing the photoluminescence jump. (b) and (c) Successive sessions of vacuum annealing were able to effectively remove the photoluminescence jump. Reprinted with permission from Ref. [108]. Copyright 2018 American Chemical Society.	65

6.4.	The temperature dependent photoluminescence of a (a) pure, as-produced sample and the sample in (b) excess 1-dodecene and in (c) excess decane. Note that the photoluminescence for (a), (b) and (c) are all normalized to the max photoluminescence in (c). (d) Optical micrographs of the photoluminescence in an as-produced silicon nanocrystal/decane matrix immediately before (top) and after (bottom) freezing. Reprinted with permission from Ref. [108]. Copyright 2018 American Chemical Society.	67
6.5.	Temperature dependent extinction spectra of pure (a) 1-dodecene and (b) decane. Reprinted with permission from Ref. [108]. Copyright 2018 American Chemical Society.....	67
6.6.	Thermal fluctuations in a (a) ‘small’ and (b) ‘large’ SiNC modeled at 300 K (top) and 77 K (bottom), where the surface atoms experience a greater degree of fluctuations. Note that to view the thermal fluctuations, snapshots from a molecular dynamics simulation were superimposed. Here we only show two models for simplicity, yet three different sized models were used. (c) The photoluminescence of these three different sized silicon nanocrystals are determined using computational methods where the green, blue and red PL curves correspond to the small, medium, and large sized silicon nanocrystal models while the dashed and solid curves correspond to photoluminescence calculated at 300 K and 77 K, respectively. In accordance with experimental results, the photoluminescence red shifted with increasing size and the photoluminescence intensity decreases with increasing temperature. Note that the small, medium, and large silicon nanocrystal consisted of 29, 66, and 220 silicon atoms, respectively. Reprinted with permission from Ref. [108]. Copyright 2018 American Chemical Society.	68
7.1.	To develop nanocrystalline superlattice, two experimental setups were designed. (a) The first experimental setup is used to control the temperature and evaporation rate of sessile drops. Two chambers with independent heating sources are connected by a small hole. The first chamber holds solvent while the second chamber houses the sessile drop. Varied substrates can be used while the temperature of the substrate can be controlled to within a tenth of a degree. The temperature control on the second chamber or solvent reservoir can be used to push solvent vapor through the small hole connecting the two chambers, thereby controlling the evaporation rate of the sessile drop. The second experimental set up is a Langmuir Blodgett trough. (b) The diameter of the trough is 1/2" or 3/8" while (c) the trough depth is approximately 1/4".	75
7.2.	(a) The plasmon peak of nanocrystalline silver exhibits a size dependent red shift (b) such that the as the size of the nanoparticle decreases the plasmon peak wavelength increases. (c) – (f) By simply drop casting silver nanoparticle solution on a TEM grid, 3D superlattice structures can form. Note: (c) and (d) were prepared from samples synthesized via Method I, while (e) and (f) were prepared from nanocrystals synthesized via Method II.	77

7.3.	Simultaneous control of both substrate temperature and solvent vapor is an effective way to influence sessile drop drying. For low solvent vapor and high substrate temperature, the nanoparticle solutions dry in constant contact area mode, while at high solvent vapor and low temperature, the nanoparticle sessile drop can dry in constant contact angle mode. Note in these samples the substrate is a fluorinated SAM on a glass slide and the solvent and solvent vapor are toluene.	79
7.4.	Drop casting silver nanoparticle suspensions in toluene on pure glass substrates at room temperature results in sessile drops drying in constant contact area mode. Within the coffee ring, droplets of excess ligand and silver nanoparticles can form. Inside of these droplets, silver nanocrystal superlattices can form.....	80
7.5.	Drop casting the same parent silver nanoparticle solution from xylene onto substrates of progressively increasing temperatures (i.e. the initial temperature was 25 °C and each progressive sample was increased by 10 °C) in a high xylene vapor pressure atmosphere resulted in various morphologies and spectroscopic absorption peaks. As the temperature of the substrate was increased for each individual sample, the resulting sample's plasmonic spectra would exhibit a second peak (Note that the plasmonic spectra was measured after the sample had returned to room temperature).	82
7.6.	As-produced samples of silicon nanocrystals were passivated with different lengths of carbon chains ranging from 12 carbon atoms to 20 carbon atoms. These different samples were then separated into distinct fractions using density gradient ultracentrifugation. The peak of the resulting photoluminescence from these samples is then plotted here where one can see that the peak emission increases with increasing fraction number. The duration of these spins was varied from 1 to 2 to 5 hours and the final letter in the key corresponds to the spin in Table 7.1	84
7.7.	Silicon nanocrystals with a ligand length of twelve carbon atoms (Spin D from Table 7.1 and Fraction 7)	85
7.8.	Silicon nanocrystals with a ligand length of fifteen carbon atoms (Spin B from Table 7.1 Fraction 7 Image 1)	85
7.9.	Silicon nanocrystals with a ligand length of fifteen carbon atoms (Spin B from Table 7.1 Fraction 7 Image 2)	86
7.10.	Silicon nanocrystals with a ligand length of eighteen carbon atoms (Spin F from Table 7.1 Fraction 9 Image 1)	86
7.11.	Silicon nanocrystals with a ligand length of eighteen carbon atoms (Spin F from Table 7.1 Fraction 9 Image 2).	87
7.12.	Silicon nanocrystals with a ligand length of eighteen carbon atoms (Spin F from Table 7.1 Fraction 9 Image 3).	87

7.13.	Silicon nanocrystals with a ligand length of eighteen carbon atoms (Spin F from Table 7.1 Fraction 9 Image 4).	88
7.14.	A representative image for fractions of the same parent taken at approximately the same centrifuge tube depth (a) but with a different spin duration of (b) 5 hours, (c) 2 hours, and (d) 1 hour.	89
7.15.	Once the particle centers are determined, various structural quantities can be computed. Here we show an example of a (a) TEM image with the (b) particle outlines selected using ImageJ. Various order parameters such as (c) m_6 and (d) n_6 can then be determined for each particle and mapped back onto the original image.	90
7.16.	Drop cast films of silicon nanocrystals with a sufficiently high concentration of material exhibit birefringent domains	92
8.1.	The (a) total energy as a function of charge for the modeled nanocluster (inset) with the corresponding (b) first (c) and second derivative. The purple dashed lines in (b) are linear fits of the form $\frac{dE}{dN} = A_1 + BN$ and $\frac{dE}{dN} = A_2 + BN$ such that $A_1 < A_2$. The jump discontinuity here represents a deviation from classic electrostatics as quantum mechanical effects become important. (d) Charge constrained DFT was used for each calculation where an electron is removed from the silver nanocluster. Green circle, blue cross, and black dot stand for PBE, HSE06, and B3LYP data, respectively. Reprinted with permission from Ref. [80] Copyright 2017 American Chemical Society	100
8.2.	The spin resolved band gap as a function of charge for the (a) singlet (b) doublet (c) triplet and (d) quartet ground state configuration. Note that the band gap for beta electrons is multiplied by -1 for clarity. (e) To compare classical results with first principle calculations, we replot Figure 8.1a with a linear background removed ($\frac{dE}{dN} = A_1 + BN$). The jump discontinuity here is very similar in magnitude to the first principles calculation of the band gap. Note that for each first principle calculation, PBE, HSE06, and B3LYP functionals were used where the same key used to differentiate functional from Figure 8.1 applies here: circle, cross, and dot stand for PBE, HSE06, and B3LYP data, respectively. Reprinted with permission from Ref. [80] Copyright 2017 American Chemical Society.	103

8.3.	(a) Spin resolved band gaps for the singlet ground state configuration for charges of 5+, 7+, 9+ and 11+. (b) The absorption spectra for a silver nanocluster in the 5+ charge state and neutral state are compared to the spin resolved density of states for the (c) charged and (d) neutral state, for reference. Note that in (c) and (d) the beta electronic states are multiplied by -1 and the shaded and unshaded regions represent occupied and unoccupied KS-orbitals, respectively. The vertical dashed lines in (b) are the four most probable optical transitions. In (d), labels 1 and 2 represent the pseudogaps while label 3 represents the formal gap (which is nearly zero in this case). Reprinted with permission from Ref. [80] Copyright 2017 American Chemical Society...	104
8.4.	Room temperature molecular dynamics simulations were conducted for the 5+ singlet ground state configuration silver nanocluster. The (a) total energy as well as the distance from the center silver atom (b) to outer silver atoms and (c) to nitrogen atoms in cytosine were determined. The colors in (b) and (c) are coded to match the inset of (b). From the molecular simulations, spin resolved time dependent Kohn-Sham orbitals were determined for (d) alpha and (e) beta electrons under PBE functionals. Reprinted with permission from Ref. [80] Copyright 2017 American Chemical Society...	107
8.5.	The orbital occupation for alpha (a) electrons and (b) holes as a function of time calculated for the silver nanocluster in the 5+ singlet ground state configuration, thermalizing from LUMO+25 to the LUMO and HOMO + 25 to the HOMO, respectively. (c) Calculated electron and hole thermalization lifetimes as a function of the energy difference between the corresponding band edge and the initial excitation level. The solid and open circles represent alpha and beta electrons, respectively, while the black and purple symbols are electron lifetimes and the green and blue symbols represent hole lifetimes. The alpha and beta electrons of both the hole and electron lifetimes are fit with an exponential function (red dashed line). Reprinted with permission from Ref. [80] Copyright 2017 American Chemical Society	108
8.6.	Normalized calculated PL (solid red line) and absorption (solid black line) spectra for the 5+ singlet model with experimental PL (dashed red line) and absorption spectra (dashed black line) from Petty (Ref [75]). Reprinted with permission from Ref. [80] Copyright 2017 American Chemical Society.....	109

LIST OF ABBREVIATIONS

AFM.....	Atomic force microscopy
AgNC	Silver nanocluster
AgNP.....	Silver nanoparticle
B3LYP	Beck, 3-parameter, Lee-Yang-Parr
CNT.....	Carbon nanotube
DEG	Diethylene glycol
DFT	Density functional theory
DGU	Density gradient ultracentrifugation
DOS.....	Density of states
EL.....	Electroluminescence
ETL	Electron transport layer
FRET.....	Förster resonance energy transfer
FS	Full spectrum
FWHM	Full width at half max
GGA	Generalized gradient approximation
GS	Ground state
HOMO	Highest occupied molecular orbital
HF	Hartree Fock
HSE06	Heyd-Scuseria-Ernzerhof
HSQ.....	Hydrogen silsequioxane
HTL.....	Hole transport layer
IOA	Independent Orbital Approximation

IR.....	Infrared
KS	Kohn Sham
LB	Langmuir-Blodgett
LED.....	Light emitting diode
LL.....	Lower limit
LUMO.....	Lowest unoccupied molecular orbital
LVF	Linear variable filter
MEG.....	Multiple exciton generation
MD	Molecular dynamics
NAC	Nonadiabatic couplings
OPV.....	Organic photovoltaic
PAW	Projector augmented wave
PBC.....	Periodic boundary conditions
PBE	Perdew-Burke-Ernzerhof
PDF	Probability distribution function
PM.....	Photomultiplier
PL.....	Photoluminescence
QY.....	Quantum yield
SAM.....	Self-assembled monolayer
SCC.....	Solar cell concentrator
SCF	Self consistent field
SEM	Scanning electron microscope
SiNC.....	Silicon Nanocrystals

SQSchockly-Queisser
SR.....Spectrally resolved
STMScanning tunneling microscope
TEMTransmission electron microscope
ULUpper limit
VASPVienna ab initio simulation package

LIST OF APPENDIX FIGURES

<u>Figure</u>	<u>Page</u>
A1. Typical light path for the upright microscope.....	138
A2. The various controls that can be changed for each measurement: (1) Fine and Course Focus, (2) Pre-sample filter, typically a notch or band pass filter, (3) Sample stage, (4) Objective, (5) Post sample filter, typically a long pass filter, (6) Pull used to direct signal to the camera or detector.	139
A3. Hex wrench and hidden hex bolt used to loosen the filter and dichroic lens housing.....	141
A4. (a) The upright microscope with numbers highlighting the various controls mentioned in the text. (r) The source and signal path for the upright microscope	142
A5. Ultracentrifuge with rotor.	142
A6. 3D printing has been used to engineer several pieces to help develop and optimize processes in this report. (a) Printed attachment to help control the evaporation rate of sessile drops. (b) 3D printed attachments are made to retrofit different linear variable filters with various filter holders (c) 3D printed components to a jig used to extract size-specific fractions after DGU. (d) A mask used in the process outlined in Appendix B5 . (e) A glass cover slip holder; (f), (g), and (h) are images of the stereolithography or .stl files used to print (d), (e) and (c), respectively.....	143
A7. Linear variable filters in a retrofitted housing.	144
A8. (a) The Xcite lamp produces broad-spectrum white light. (b) The blue housing excitation source can contain two different LED drivers, a blue 365 nm LED and a broad-spectrum white light. (c) The PhoxX 375 nm laser is typically used during quantum yield measurements, while (d) the pulse laser is used for lifetime measurements.....	145
A9. Fiber coupled spectrometer.....	145
A10. Photomultiplier tube used to measure sample lifetimes.	146
A11. (a) Standard and (b) ProEM low-light resolution camera.....	146
B1. Light path for a photoluminescence measurement.	147
B2. Light path for a lifetime measurement.....	148

B3.	Light path for a quantum yield measurement. Note that the sample is inside of an integrating sphere.....	149
B4.	Tray to hold clean glass cover slips during self-assembled monolayer coating.	151
B5.	A (a) clean glass cover slip is coated with a (b) self-assembled monolayer. (c) Ultraviolet oxygen plasma exposure of a treated glass slide and mask will (d) effectively remove specific areas of the monolayer.	152
B6.	Patterned self-assembled monolayers on glass cover slips revealing a (a) series of lines and (b) the NDSU Bison mascot after dip coating in solvent.	153

CHAPTER 1. INTRODUCTION TO NANOPARTICLES AND NANOTECHNOLOGY

1.1. Introduction

At the turn of the 20th century, viewing and manipulating atoms was only the talk of science fiction. Yet, in 1959, famous American physicist Richard Feynman gave credibility to this idea in his famed speech “There’s plenty of room at the bottom”.^{1,2} In this speech, Feynman discusses the possibility of controlling small hands that controlled even smaller hands that would control yet smaller hands, until the hands were small enough to manipulate atoms. At this scale, Feynman reasoned, the entirety of the Encyclopedia Britannica could be printed on the head of a pin. Since this speech, atoms have in fact been manipulated through the use of scanning tunneling microscopy (STM)³, while the advent of the integrated circuit has drastically reduced the space required to store data, thanks in part to Moore’s Law.

At the atomic length scales described by Feynman, the physics of quantum mechanics starts to play a crucial role, and due to quantum confinement, the optical and electrical properties of materials become size dependent. These size dependent systems were predicted in the early 1900’s with the development of quantum mechanics and Schrodinger’s equation⁴, yet it wasn’t until the second half of the twentieth century before synthetic schemes were able to fully realize these nanomaterials.⁵⁻⁷ The timeline in **Figure 1.1** highlights some of the major nanomaterial ‘discoveries’ while the following section goes over a brief history of the field of nanotechnology.

1.2. History of Nanotechnology

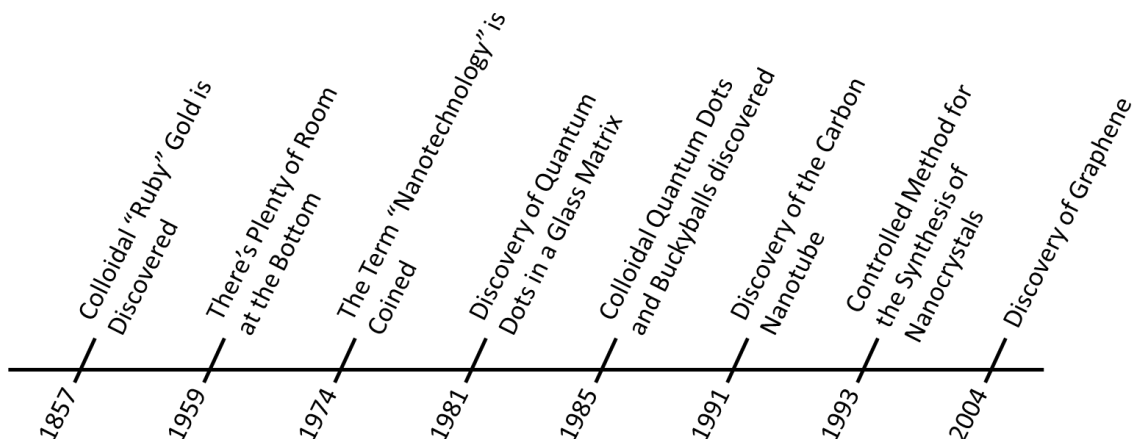


Figure 1.1. Timeline of Nanotechnology

The term discovery is placed in quotes in the previous section because several of these nanoparticles have been unknowingly used or can be found in nature. The discovery aspect comes in the ability to characterize and isolate such materials. For instance, graphene was under scientists' noses for decades as graphite, the material used for pencil lead. It was not until 2004 when Novoselov and Geim used tape to mechanically exfoliate graphene sheets from graphite that they were able to characterize the material, earning them a Nobel prize six years later.⁸ Looking further back, ancient sword makers and cup designers unknowingly used nanotechnology as part of their craft. The Damascus saber blade, known for its light weight yet durable blade, was a result of the alignment of carbon nanotubes (**Figure 1.2a-b**)^{9, 10}, while the Lycurgus Cup of Rome is an example of plasmonic gold and silver nanoparticles interacting with light (**Figure 1.2c-d**).¹¹

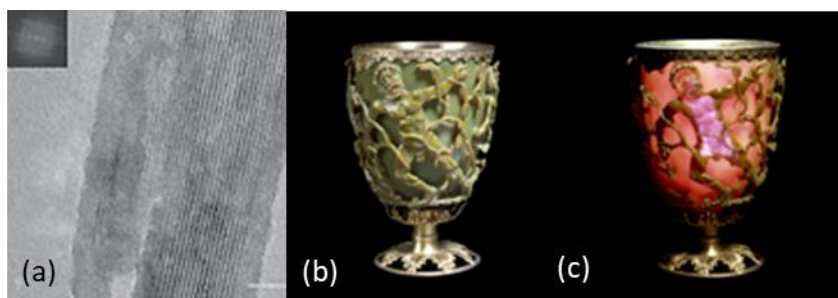


Figure 1.2. Nanoparticles have been used in ancient instruments throughout time. Damascus blacksmiths were able to create strong and light (a) ‘Damascus saber blades’ that had aligned carbon nanotubes in the blade. Reprinted from Ref. [10] with permission from Springer Nature. In ancient Rome, gold and silver nanoparticles were created in situ in the Lycurgus Cup of Rome. (b) Light reflected from this cup would appear opaque green while (c) transmitted light would be scattered due to the embedded plasmonic nanoparticles giving the cup a translucent red appearance. © Trustees of the British Museum

Although more modern examples of scientists working within the current definition of nanotechnology existed prior to Feynman’s 1959 speech, such as Richard Zsigmondy’s work on colloids¹²⁻¹⁴ and Irving Langmuir and Katherine Blodgett’s work on nanometer sized coatings¹⁵⁻¹⁷, Feynman’s ‘Plenty of Room at the Bottom’ speech is most often recognized as the starting point for the field of nanotechnology. The term nanotechnology was coined fifteen years later, in 1974, when Japanese scientist Norio Taniguchi used it to describe semiconductor processes that occurred on the nanoscale.¹⁸ After that, a series of ground-breaking discoveries were made related to nanoparticles. In 1985, Richard Smalley, a major proponent of the field of nanotechnology, helped discover the Buckminster fullerene or buckyball, the first of the nanoscale carbon allotropes.¹⁹ The buckyball is a series of sp^2 hybridized carbon atoms that resemble a soccer ball. That same year, Louis Brus discovered colloiddally stable quantum dots, a hallmark material in nanotechnology, and the effect of quantum confinement in nanoparticles.²⁰ In 1990, Canham discovered room temperature photoluminescence (PL) in silicon quantum wires, signaling the first observation of room temperature PL from silicon, which represents a significant breakthrough pertinent to this

report.²¹ A year later, the second major nanocarbon allotrope was discovered, the carbon nanotube (CNT), by Sumio Iijima using arc-discharge synthetic methods similar to those used for the synthesis of the Buckminster fullerene.²² At this point in time, although nanomaterials exhibited highly size dependent properties, very few synthetic protocols were able to fully exploit these effects. However, in 1993 Mounji Bawendi and coworkers developed a method for the controlled synthesis of quantum dots, while significant synthetic improvements related to the size and morphology of metal nanoparticles were observed over this same time period.^{5, 23-25} In 2004, as discussed earlier, the last of the major nanocarbon allotropes, graphene, was discovered by Novoselov and Geim.⁸ Two years later, in 2006, a non-thermal plasma synthetic method was developed by Mangolini *et. al.* which was capable of producing silicon nanocrystals (SiNCs), a nontoxic alternative to metal-chalcogenide quantum dots, with quantum yields (QYs) greater than 60 %.²⁶ Since then, several commercial applications of nanoparticles have been developed, such as ultralight sports equipment, transparent sunscreen, and high definition TV screens, to name a few.

1.3. What are Quantum Dots



Figure 1.3. Quantum dots of increasing size will emit, when properly excited, with increasingly lower energy photons due to the quantum confinement effect. Quantum dots above were produced by PlasmaChem and are reprinted under the Creative Commons Attribution-Share Alike 3.0 Unported License.

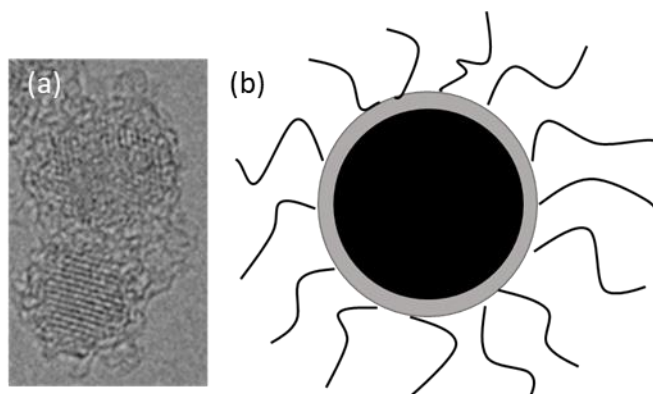


Figure 1.4. Typically, a quantum dot or nanoparticle consists of two main components, the inorganic core and the outer ligand layer. The size of the inorganic core is used to control various optical properties while the ligand is most typically used to invoke colloidal stability. In some cases, an inorganic shell can cap the inorganic core to help improve optical properties or to limit the toxic effects of the core. Panel (b) shows a model nanoparticle with a core (black), shell (gray), and ligand layer, while (a) shows a transmission electron micrograph of two silicon nanocrystals on a graphene substrate, where one can see both the crystalline planes of the silicon atoms as well as the brush-like layer of the ligands surrounding the nanoparticles. Reprinted with permission from Ref. [28]

Quantum dots are a form of semiconducting material where, because of their small size, the quantum confinement effect plays a significant role in the observed optical and electrical properties. The electronic structures of these nanoparticles can be modeled, in the simplest of senses, as a particle-in-a-box, although, in practice this is not strictly the case due to the presence of surface states, chelating ligands, and the nature of the bulk band gap. A basic quantum dot can consist of just the inorganic semiconductor core material, such as CdTe, PbS, or silicon, with a ligand layer surrounding this core material for colloidal stability. These ligands are typically short carbon chains (such as dodecene or octadecene) that sterically prevent nanoparticles from aggregating.^{27, 28} Ligands have also been used to affect the photophysics of the quantum dot itself,^{29, 30} while work by Talapin *et al.* showed that inorganic ligands can be used to enhance the inter-nanocrystal coupling in nanocrystal solids.³¹ In other cases, the semiconducting core of the quantum dot will be surrounded by another material, typically an insulating material (**Figure 1.6b**)

referred to as the shell, to limit the number of surface states on the quantum dot surface^{32, 33} or as an engineering control to limit the toxicity of the core.³⁴

1.4. Applications of Quantum Dots

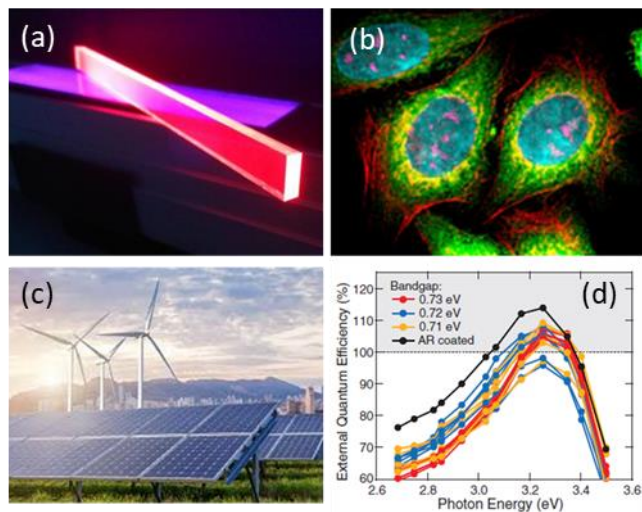


Figure 1.5. Nanoparticles can be used in several applications ranging from energy capture to biological markers. In panel (a), quantum dots are used as a solar cell collector to gather light from a window and direct it to an inline photovoltaic. Reprinted with permission from Ref. [48]. (b) Nanoparticles with the appropriate passivation are attached to different parts of the cell, demonstrating their applicability as biomarkers. Reprinted with permission from Ref. [57]. (c) Typical monocrystalline solar cells with a band gap of approximately 1.1 eV can only achieve an overall efficiency of 33 %. Quantum dot solar cells on the other hand, due to the confined nature of the exciton, can excite two electrons into the valance band, through a process known as multiple exciton generation, effectively doubling the possible overall efficiency. In (d), PbS quantum dots are shown to have external quantum efficiencies greater than 100 %, indicative of multiple exciton generation in these devices. Reprinted with permission from Ref. [38].

Due to their unique size dependent properties, nanoparticles have promising applications in several commercial sectors. In this section, however, we will only focus on one particular type of nanoparticle, the quantum dot, as the SiNC is part of this family of nanoparticles. Furthermore, we will only focus on three promising technologies for this material: photovoltaic cells, light emitting diodes (LEDs), and fluorescent biomarkers and sensors.

1.4.1. Quantum Dot Solar Cells

With global temperatures on the rise, the need for clean renewable energy is a priority, and although several renewable energy sources exist, the photovoltaic cell offers the most freedom in form factor while boasting some of the greatest energy potentials. For example, the sun delivers 165,000 terawatts of clean power to the earth at every instant.³⁵ To put that in perspective, the total global energy consumption in 2016 was 154,000 terawatt hours.³⁶ This means that in one hour, the sun has provided enough energy to power the earth for one entire year. Unfortunately, typical crystalline silicon solar cells are expensive to manufacture and can only reach a maximum efficiency of 33 % due to the Shockley-Queisser (SQ) limit.³⁷ Fortunately, the current generation of photovoltaic cells are working on this challenge, attempting to reduce manufacturing costs while also overcoming this SQ limit.

Quantum dot solar cells show promise for both lowering manufacturing costs and exceeding the SQ limit. The polycrystalline silicon solar cell uses expensive high-temperature processes while requiring a relatively clean environment for manufacturing, which raises the cost of production. Colloidally stable quantum dots, on the other hand, can ideally be manufactured using wet processing techniques under ambient conditions. Furthermore, the small size of quantum dots give rise to several key mechanisms that can overcome the SQ limit. Multiple exciton generation (MEG), for example, limits thermalization energy loss by producing two or more excitons from a single photon of sufficient energy³⁸⁻⁴³, while theoretical reports have indicated that ordered arrays of quantum dots can produce minibands between the valence and conduction band, where lower energy excitons can occupy these states until another photon excites them into the conduction band.⁴³⁻⁴⁷ These mechanisms highlight the tunability of quantum dots, where size and microstructure play a role in the final device performance (**Figure 1.7**).

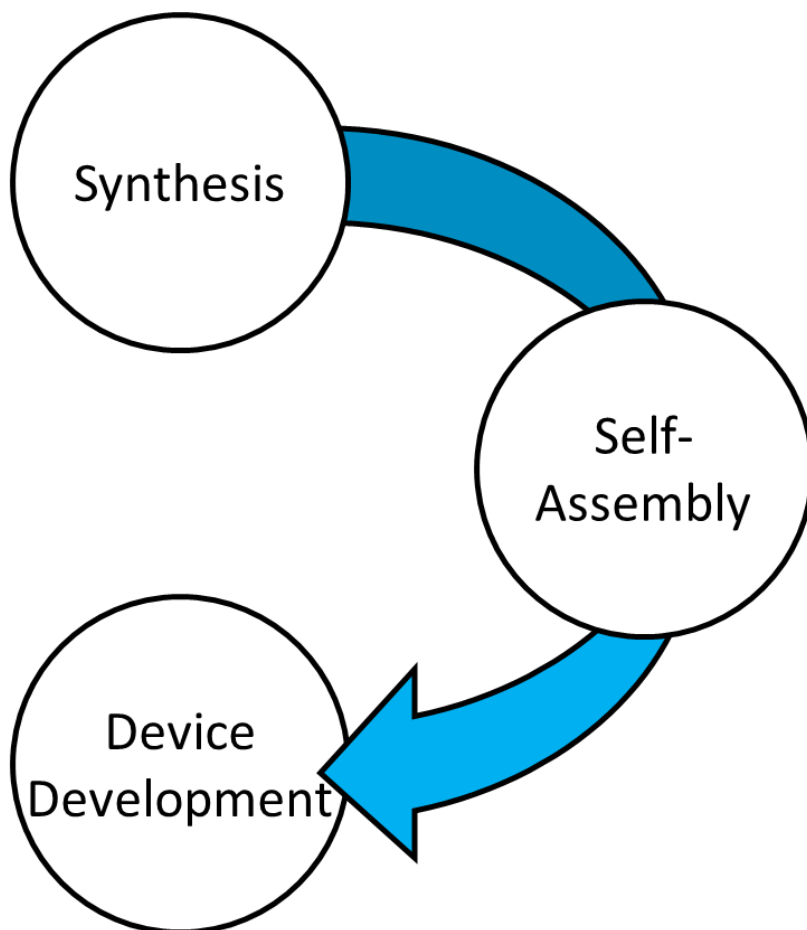


Figure 1.6. The synthesis and self-assembly of nanoparticles, or superlattice development, both play a significant role in the performance of devices such as a quantum dot solar cell, field effect transistor, or light emitting diode. This inherently allows for several degrees a freedom in fabrication methods and tunability in the corresponding device.

Another promising application of quantum dots in energy generation comes in the form of solar cell concentrators (SCC) (**Figure 1.5a**). Glass or plastic quantum dot composites can absorb high-energy radiant light and then re-emit light at a lower energy.⁴⁸⁻⁵⁰ A solar panel strategically placed along the edge of this glass pane can then collect all the fluorescence from the embedded nanoparticles for conversion into electric energy. This SCC could be used in sky scrapers, effectively turning every window into an energy collection source.

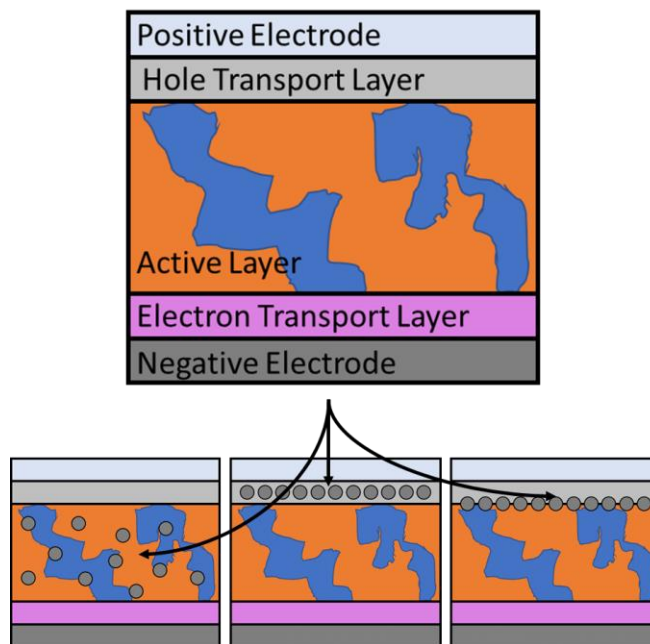


Figure 1.7. (a) A typical bulk heterojunction organic photovoltaic device consists of a positive and negative electrode, a hole transport layer and electron transport layer, as well as the active layer. Plasmonic nanoparticles can be incorporated into the (b) active layer, (c) hole transport layer, and (d) the interface of the hole transport layer and the active layer.

One final application of nanoparticles in photovoltaic cells is the incorporation of plasmonic nanoparticles into organic photovoltaics (OPVs). Although plasmonic nanoparticles are not considered to be quantum dots, this application of nanoparticles in solar energy harvesting is still in line with the current discussion. Solution-based methods to produce OPVs have proven to be considerably cheaper than many other photovoltaic processing techniques, due in part to the scalability of polymer synthesis and the processability of polymers.^{51, 52} Although the typical efficiencies of these devices currently pale in comparison to traditional silicon based devices, the extremely low price of roll-to-roll manufacturing techniques makes these materials a viable competitor.⁵² To boost efficiency in these devices, plasmonic nanoparticles have been shown to be quite effective.⁵³ **Figure 1.7a** shows a typical OPV device consisting of a positive and negative electrode, hole transport layer (HTL) and electron transport layer (ETL), as well as the active layer,

while **Figure 1.7b-d** shows the diverse ways in which plasmonic nanoparticles can be incorporated into the device, all of which impact the final device performance.

1.4.2. Light Emitting Diodes and Displays

LEDs are another promising application of quantum dots. LEDs are extremely energy efficient lighting sources that have a host of benefits over more traditional incandescent and fluorescent light sources. The superior energy efficiency could have huge energy savings, with predictions that by 2030, the widespread use of LEDs could save about 190 terawatt hours of electricity per year.⁵⁴ Furthermore, the considerably long lifetime of these devices lowers the maintenance costs, while its semiconducting nature makes for simple electronics incorporation. Also, the solution processing of colloidal quantum dots could lower the cost of manufacturing, further improving the marketability of these materials.⁵⁵

However, one of the biggest advantages for using quantum dots as the emitting material in LED displays comes from the size-dependent band gap. Where many traditional fluorophores exhibit multiplex/broad emission, quantum dots give single-peak emission with a narrow linewidth. **Figure 1.8a-b** shows the gaussian PL and electroluminescence (EL) of size separated SiNCs, where it is clear that the PL emission matches the electrically driven EL emission.⁵⁶ Note that the typical emission linewidth from QD-LEDs is usually much narrower, but electron-phonon coupling across the indirect band gap of SiNCs results in a much broader peak. Commercial applications of quantum dot displays have already been realized, such as the QLED TV from Samsung (**Figure 1.8c**), yet many of these current displays use quantum dots only as a fluorophore layer, with a blue pumping LED behind the QD layer to drive the nanoparticle emission.

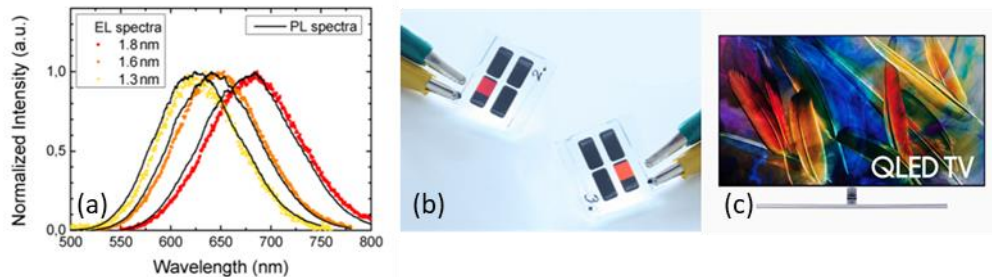


Figure 1.8. The size tunable Gaussian emission of quantum dots makes them ideal candidates for applications in light emitting diodes and displays. The photoluminescence and electroluminescence of size separated silicon nanocrystals are compared (a) while the stacked light emitting device is shown in (b). (a) and (b) are reprinted with permission from Ref. [56] (c) Quantum dots can be found in commercial displays such as the Samsung QLED TV. Typically a blue light-emitting diode is used to drive fluorescence in a layer of quantum dots to achieve the high-quality display.

1.4.3. Fluorescent Biomarkers and Sensors

The anatomy of a nanoparticle has key features that are well suited for applications as biomarkers and biosensors. The small size allows for permeation throughout the body while specific biotags can be grafted to the surface to steer the nanoparticles to specific targets.⁵⁷⁻⁵⁹ All the while, the core can be chosen based on the specific application. For instance, Halas and coworkers developed a bio-nanoparticle system for the treatment of cancer using silica nanoparticles with a gold shell.⁶⁰ Because of their size, these nanoparticles assimilate in cancer cells due to the ‘enhanced permeability and retention’ effect,^{61, 62} absorb infrared (IR) light that easily passes through bodily tissue, and photothermally ablate the local cancer cells.⁶⁰ There had been several attempts at using photothermal treatments for cancer prior to this work, but these were hindered by the inability to achieve focused heating.⁶³⁻⁶⁵

Quantum dots can also be used as fluorescent sensors by exploiting mechanisms such as Förster resonance energy transfer (FRET). FRET describes the energy transfer between two fluorophores. The first fluorophore, in an excited state, can transfer energy to the second

fluorophore, which then emits light in accordance with Kasha's rule.⁶⁶ The efficiency of FRET and the rate of this process are strongly coupled to the distance between each fluorophore, making it an ideal sensor. This concept can be applied to quantum dots by attaching a fluorescent molecule at a known distance from the quantum dot surface and measuring the associated FRET for the system.⁶⁷⁻⁷¹ Any changes to the distance between the quantum dot and attached fluorophore can be detected, so if the attached ligand has a cleavage site, one can determine the concentration of bio-analytes, for example, based on the rates at which the quantum dot and fluorophores are dissociated.

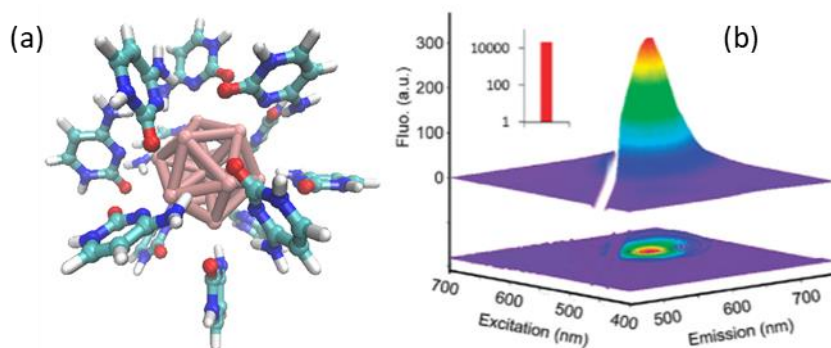


Figure 1.9. Silver nanoclusters have been shown to be ideal candidates for biological markers and sensors. The small size is ideal for intracellular transport while the photoluminescence is strong but highly sensitive to the surrounding environment. (a) Representation of a silver nanocluster with twelve cytosine molecules complexed to the surface while (b) shows the increase in photoluminescence of DNA complexed silver nanoclusters when they are hybridized with the appropriate target. (a) and (b) are reprinted with permission from Ref. [80] and Ref. [79], respectively.

Although not strictly classified as a quantum dot, fluorescent-DNA-complexed silver nanoclusters (**Figure 1.10a**) have started carving out a niche in nanoparticle sensor and fluorophore research for biological applications, due in part to the non-toxic nature of silver and its unique PL.⁷²⁻⁸¹ Furthermore, the small size (~ 1nm in diameter) and the typical ligand used for passivation (DNA) allow for easy intracellular transport and bioconjugation, respectively.⁷² The PL in these silver nanoclusters, albeit not fully understood, appears to be strongly dependent on

the shape⁷⁷, charge^{80, 81} and surrounding passivation.^{77, 79, 82} The strong dependence of PL on the nanocluster's local environment has been shown to be a good means for developing silver nanocluster sensors. For instance, in one particular example by Yeh *et al.*, the PL of silver nanoclusters would increase 100-fold upon DNA hybridization with a specific target material (Figure 1.10b).⁷⁹

1.5. Toxicity and Environmental Concerns

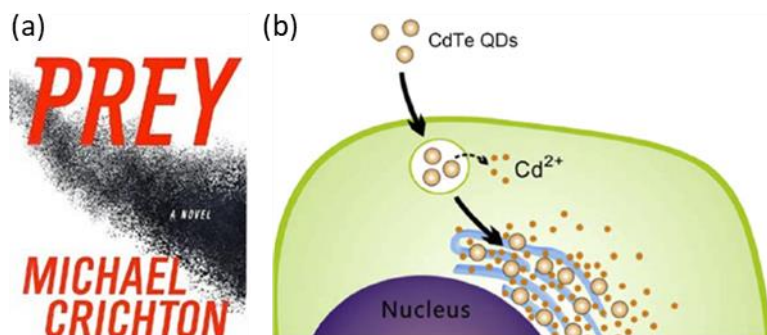


Figure 1.10. Many nanoparticles can present toxicity concerns. (a) In Michael Crichton's book, *Prey*, he describes the tale of rogue nanoparticle robots terrorizing any living thing within reach. (b) The small size of nanoparticles allows for cellular uptake and decomposition inside the cell membrane. This highly localized concentration of ions can then be toxic to the cell. Reprinted from Ref. [96] with permission from Elsevier.

In 2002, two years after President Clinton launched the National Nanotechnology Initiative (NNI), Michael Crichton, author of the classic *Jurassic Park* series, wrote about the potential hazards associated with nanotechnology. In his book, *Prey*, a nanorobotics company develops a method to produce mass quantities of nanorobots. Initially designed with good intentions, these nanorobots turn on the company, becoming self-replicating and self-sufficient. The nanoparticles work together in swarms, wreaking havoc across the company campus and threatening the safety of the greater public.

Crichton's fears in *Prey* may be farfetched, but toxicity concerns in nanomaterials are warranted. For example, at the end of the 19th century, asbestos was used in various applications

requiring thermal insulation. Yet, as is now known, this fibrous mineral with a high aspect ratio and needle-like structure causes mesothelioma in the lungs. Unfortunately, CNTs share a similar needle-like structure and have thus been dogged by some of the associated carcinogenic concerns.⁸³⁻⁸⁵ This potential toxicity is not limited to needlelike nanoparticles such as CNTs, as spherical nanoparticles have been shown to be toxic as well.^{84, 86, 87} Many of the semiconducting nanoparticles or quantum dots are made with cadmium and lead, both known toxic substances, and the size scale characteristic of these nanoparticles can result in an enhanced toxicity (**Figure 1.3b**).^{86, 88-95} Due to their small size, some nanoparticles can pass through the cell membrane, and once inside the cell, the nanoparticles breakdown, resulting in an abnormally high concentration of ions, which in turn leads to cellular mortality.⁹⁶ In dramatic fashion, **Figure 1.4** shows the effects that size alone can have on the resulting toxicity. In this study Meng *et al.* analyzed the size dependent effects that copper particles had on mice, using micro, nano and ionic sized samples.⁹² The stomach of the mouse that ingested the copper nanoparticles showed the greatest damage, indicating the potential dangers of nanoparticles as a result of the unique size scale alone.

It is important to emphasize that studies such as the one cited above are not intended to scare away researchers in the field of nanotechnology, but to highlight the importance of finding safe and viable solutions in the field. In fact, many solutions have already been developed. For example, instead of using toxic starting materials such as lead and cadmium, many nanoparticles are developed using safe alternatives, such as InP and silicon. SiNCs, the topic of this dissertation, have in fact gone through several different toxicity studies, including tests on mice and macaques, where no harmful effects were identified, suggesting that silicon might offer a safe alternative to materials derived from the metal-chalcogenides.⁹⁷

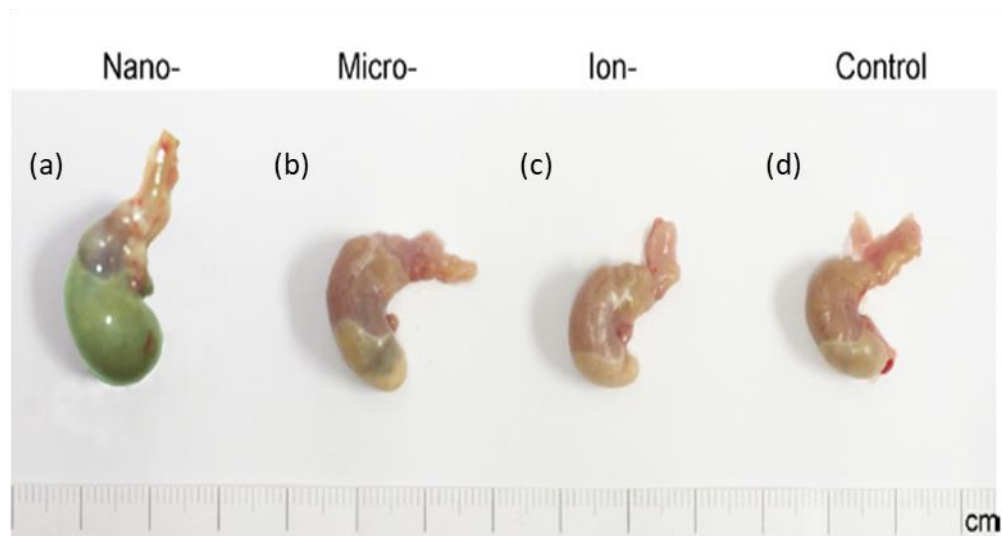


Figure 1.11. Images of mouse stomach after a single oral gavage for 24 h of (a) nano-sized copper (b) micro-sized copper (c) ionic-sized copper and (d) no copper. The mouse that digested nanosized copper shows clear discoloration and swelling. Reprinted from Ref. [92] with permission from Elsevier.

1.6. Silicon Nanocrystals

This introduction has mainly focused on nanotechnology and quantum dots in general, and we have discussed the main topic of this report, SiNCs, only in passing. SiNCs are a subset of the quantum dot family sharing many of the potential applications mentioned earlier, such as solar cells^{39, 98-101}, LED displays⁵⁶, and biological markers.¹⁰² However, because of their nontoxic nature,⁹⁷ SiNCs avoid many of the environmental and toxicological pitfalls associated with metal chalcogenide quantum dots outlined above.

Although bulk silicon is currently the king of the electronics and microelectronics sector, very little ground has been made with silicon in the photonics sectors. This is primarily due to inefficient electron hole recombination in bulk silicon in part because of the indirect band gap. Unlike a direct band gap semiconductor, an indirect semiconductor requires the participation of a phonon to facilitate electron hole recombination. This phonon dependence appeared to be relaxed

when room-temperature PL from silicon quantum wires was first observed in 1990 by L.T. Canham.²¹ The quantum wires in question had nanosized structures that confined the exciton, allowing for efficient recombination and thus PL. Although this was very intriguing, it was a few years before research on colloidal SiNCs could really begin, as practical synthetic schemes were not yet available. As synthetic techniques for SiNCs have become more refined,^{103, 104} coupled with the advances in purification and size separation,¹⁰⁵⁻¹⁰⁷ the analysis and understanding of the mechanisms of electron-hole recombination in SiNCs has also improved. As such, several studies have now been completed on the subject of electron-hole recombination in SiNCs, but many researchers are still at odds on the subject.^{30, 105, 106, 108-128} As a result, this report will focus mainly on fully understanding the mechanisms of PL in SiNCs.

CHAPTER 2. SILICON NANOCRYSTAL SYNTHESIS, PASSIVATION, AND SIZE SEPARATION

2.1. Introduction

Several nanoparticles are currently synthesized using what is referred to as the “hot injection” method.^{2, 129} Although this synthetic technique has been quite successful for a variety of nanoparticles, unfortunately the same chemistry cannot be easily applied to silicon. Thus, several alternative methods have been developed, including a non-thermal plasma,^{103, 130, 131} laser ablation,^{132, 133} CO₂ laser pyrolysis of silane,¹³⁴ silicon suboxide annealing,^{104, 135, 136} and several simple single-pot methods.¹³⁷⁻¹³⁹ Three of these methods will now be discussed in greater detail, as they represent the diverse methods by which SiNCs are made and highlight the pros and cons of each approach.

Additionally, this chapter will discuss the passivation and size separation of SiNCs. Surface passivation plays a key role in SiNC colloidal stability,²⁷ charge transport¹⁴⁰ and self-assembly,¹⁴¹ as well as strongly influencing SiNC photophysics.^{142, 143} Finally, this chapter will discuss the size separation of colloidal SiNC nanoparticles using density gradient ultracentrifugation (DGU), a technique that has been useful for the separation of several types of nanomaterials.^{107, 144-147}

2.2. Silicon Nanocrystal Synthesis

The optical and electrical properties of SiNCs appear to be somewhat dependent upon the synthetic method.^{131, 136, 148, 149} For example, the synthesis of SiNCs *via* a non-thermal plasma method typically produces pseudo-spherical particles of crystalline silicon with a diameter of 3-4 nanometers.¹³¹ These nanocrystals have size dependent photoluminescence in the red region of the visible spectrum (600 – 800 nm) with at least two different modes of decay, a fast nanosecond

decay and a slow microsecond decay.^{108, 109} In contrast, the synthesis of SiNCs *via* the reduction of a reverse micelle containing silicon tetrachloride produces blue emitting (400-500 nm) crystalline silicon quantum dots that are 2-3 nm in diameter and have one fast (nanosecond) mode of decay.¹³⁷ The following three sections (2.1.1 – 2.1.3) will describe these synthetic methods, as well as the synthesis of SiNCs *via* the thermal annealing of a silicon suboxide.

2.2.1. Non-Thermal Plasma Synthesis

The non-thermal plasma synthesis pioneered by the Kortshagen group produces highly crystalline SiNCs (**Figure 2.1b**) with exceptional electrical and optical properties.^{103, 131} In this case, a non-thermal plasma is achieved by flowing a mixture of silane (SiH_4) and argon gas through a small quartz tube that is under reduced pressure.¹³¹ Two leads from a radio frequency power source are wrapped around this quartz tube and spaced one quarter of an inch apart from each other (**Figure 2.1a**).

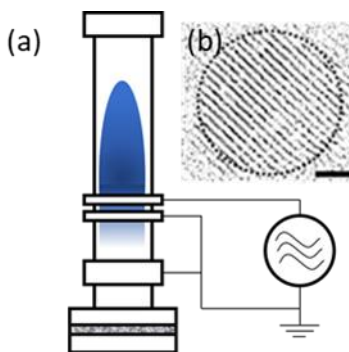


Figure 2.1. The synthesis of silicon nanocrystals can be done using a non-thermal plasma of silane and argon gas. (a) The apparatus used to make these nanocrystals is a quartz tube fitted with a vacuum line on the downstream end and a gas inlet line on the upstream end. Two leads of a radio frequency generator wrapped around the tube are used to generate the non-thermal plasma. (b) The product of this method is crystalline silicon nanocrystals with diameters of approximately 3 to 4 nm (scale bar is 1 nm). Reprinted with permission from Ref. [106]. Copyright 2018 American Chemical Society.

As the mixture of silane and argon gas flows through the quartz tube, a plasma is initiated near the wire leads. In this plasma, the gaseous molecules disassociate into charged silicon and hydrogen ions, where the argon gas is used to stabilize the plasma. These ions travel down the tube, where nanoparticle nucleation and growth occur. Once the nanoparticles pass through the tube they are collected on a substrate where they can be later dispersed in an organic solvent and passivated. Nanocrystal size control is achieved by regulating the residence time of the nanoparticles, controlling the power in the plasma, or changing the partial pressures of silane and argon in the reactor.^{103, 131} This method almost exclusively uses silane gas as the precursor, with some exception for silicon tetrachloride (SiCl_4)¹⁵⁰ and recent efforts at NDSU using cyclohexasilane (Si_6H_{12}).

2.2.2. Silicon Suboxide Anneal Synthesis

Another robust method for the synthesis of SiNCs is the decomposition of a silicon suboxide ($\text{HSiO}_{1.5}$).^{104, 105, 136} A silicon suboxide material can be made synthetically *via* the controlled reduction of silicon tetrachloride with water in an inert atmosphere.¹⁰⁵ Otherwise, commercially available hydrogen silsesquioxane (HSQ) can also be used as a silicon suboxide (**Figure 2.2a**).¹³⁶ These silicon suboxides are annealed at temperatures in excess of 1100 °C, depending on the desired nanocrystal size. For instance, properly milled HSQ annealed at 1100 °C, 1200 °C, and 1300 °C will produce nanocrystals with a diameter of approximately 3.1 nm, 7.3 nm, and 10.3 nm, respectively, when the crystalline SiNC cores are liberated from the silicon dioxide shell.¹³⁶ Employing more advanced annealing schemes, Yu *et al.* were able to synthesize cuboctahedral shaped nanoparticles, which were shown to have a high propensity for self-assembly.¹⁵¹ The annealing process causes the decomposition of the silicon suboxide into silicon nanocrystals encased by a silicon dioxide shell (**Figure 2.2b**). The SiNC/silicon dioxide composite

is then mechanically broken down, first by a mortar and pestle¹⁴⁴ and then ball milled for greater monodispersity in the final product.¹³⁶ After the mechanical breakdown, the SiNCs are liberated from the encasing silicon dioxide layer *via* concentrated hydrofluoric acid etching. These bare SiNCs are then extracted in toluene and passivated accordingly.

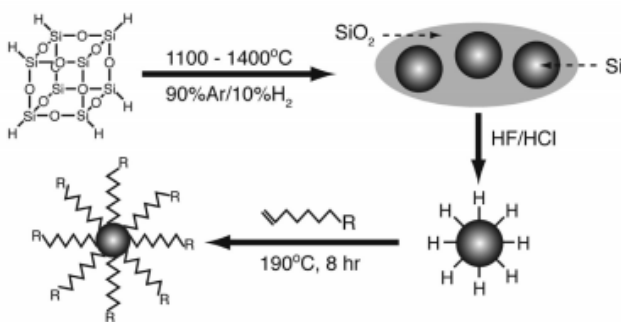


Figure 2.2. The decomposition of a silicon suboxide precursor such as commercially available hydrogen silsesquioxane is used to produce monodisperse silicon nanocrystals. The silicon suboxide is first annealed at temperatures in excess of 1100 °C to decompose it into silicon nanocrystals encased in silicon dioxide. This silicon nanocrystal/silicon dioxide composite is then mechanically milled and etched in hydrofluoric acid to liberate the silicon nanocrystals. The extracted nanocrystals are then passivated, typically with short carbon chains. Reprinted with permission from Ref [136].

2.2.3. Reverse Micelle Synthesis

The synthesis of SiNCs via the reduction of a reverse micelle somewhat resembles the hot injection method used for metal-chalcogenide quantum dots. In this method, silicon tetrachloride (SiCl_4) and hexyltrichlorosilane ($\text{C}_6\text{H}_{13}\text{SiCl}_3$) are mixed in toluene and sonicated for thirty minutes. The hexyltrichlorosilane emulsifies the silicon tetrachloride, creating a reverse micelle (**Figure 2.3b**). A reducing agent, such as lithium aluminum hydride, is then added to create 2-3 nm diameter silicon quantum dots. It should be noted that pyrophoric silane gas can be produced as a byproduct of this synthetic method and care should be taken. The final product is a blue emitting SiNC (**Figure 2.3d-e**) with a hexyl organic capping layer. There exist several variations

of this single-pot synthetic scheme that differ primarily in the reducing agents and surfactants used during synthesis.^{148, 152-154}

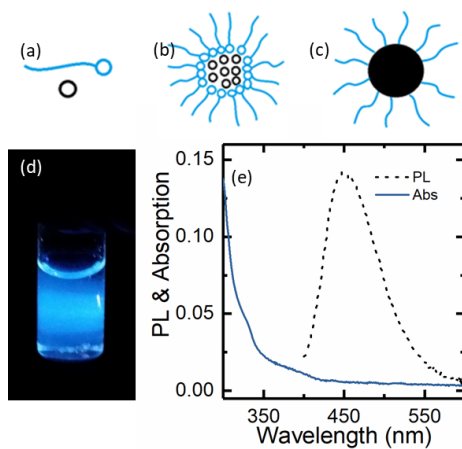


Figure 2.3. Blue emitting SiNCs can be synthesized via a one pot synthetic scheme. (a) Silicon tetrachloride (black circle) and hexyltrichlorosilane (blue circle) create a (b) reverse micelle in toluene. The addition of a lithium aluminum halide reduces the silicon tetrachloride core creating (c) a silicon quantum dot. These silicon quantum dots have (d) - (e) blue photoluminescence typical of the single pot synthetic methods.

2.3. Passivation

Typical quantum dot ligand interactions can be classified into three different categories, X-type, L-type, and Z-type,¹⁵⁵ which is in reference to the covalent bonding classification developed by Green *et al.*¹⁵⁶ In this classification, X-type ligands form normal covalent bonds, L-type ligands are coordinate covalent bonds or a neutral Lewis base, and Z-type ligands are two electron acceptors or Lewis acids. Typical metal-chalcogenide quantum dots have L-type ligands, where the ligand is acting as a Lewis acid. The facile nature of these L-ligands for bonding to metal and semiconducting nanoparticles allows for easy ‘ligand exchanges’, which can be used to influence nanocrystal self-assembly and optical properties.¹⁵⁷⁻¹⁵⁹ Ligand exchange can also be done in solid-state nanocrystal films, which has been shown to be very beneficial for making devices¹⁶⁰⁻¹⁶⁴ because carrier mobility through nanoparticle solids is dependent upon interparticle coupling and distance.¹⁴⁰ On the other hand, SiNC ligands can be classified as X-type. These normal covalent

bonds are less facile than the L-type ligands, which is beneficial for keeping the SiNCs stable in liquid suspensions but limits the possibility for ligand exchange in solution and in solid films. In order to achieve some semblance of ligand exchange in SiNCs, thiolene click chemistry has been employed.¹⁴⁹ In another attempt, chlorine-terminated SiNCs were colloidally stabilized through hypervalent interactions with the solvent (e.g., solvents containing nitrile or ketone groups will bond with the surface of SiNCs, keeping the nanoparticles colloidally stable for over a year).¹⁶⁵ This allows the nanoparticles to remain colloidally stable without explicitly grafting carbon chains to the SiNC surface.

Practical and common methods for the passivation of SiNCs typically use the mechanism of hydrosilylation. Hydrosilylation describes the addition of a Si-H bond across an unsaturated bond and there are currently four different methods used for SiNCs: (1) thermal, (2) photoinitiated, (3) catalyst initiated, and (4) plasma hydrosilylation. In the first and most popular method, thermal hydrosilylation, the bare SiNCs are refluxed with the ligand in a high boiling point solvent, such as mesitylene, at around 180 °C.¹⁶⁶ In the second method, photoinitiated hydrosilylation is similar to the thermal hydrosilylation method, but uses ultraviolet light to overcome the activation energy instead of heat.¹⁶⁷ This allows for lower temperature passivation that can be carried out in lower boiling point solvents. In an interesting variation of this method, Miyano *et al.* left a small amount of hydrofluoric acid in the reaction mixture so any surface oxidation would be removed *in situ*.¹⁶⁸ The third method is relatively new, but has been able to produce SiNCs with three times greater PL compared to its thermally passivated counterparts. This method uses phosphorus pentachloride (PCl₅) as a catalyst to initiate the functionalization of SiNCs.¹⁶⁹ The final method, a gas phase plasma method, has had limited applicability due to the complexity of the experimental set up, requiring non-thermal plasma synthesized SiNCs to pass into a second plasma chamber

where the ligand is in the gas phase.¹³⁰ This method allowed for the passivation of short carbon chain ligands but in general produced a worse surface coverage than the thermally passivated SiNCs.

2.4. Size Separation

Due to the size dependent properties of semiconductor nanocrystals, it is important to have samples of high size resolution. The first and best way to achieve a high size resolution is synthetically. But when synthetic methods fail, post synthetic methods are required. Here the size separation method known as density gradient ultracentrifugation (DGU) is discussed, as it has been successful in size separating several types of nanoparticles.^{107, 144-147, 170}

While in suspension, colloidal particles typically experience two simple forces; a gravitational force and a viscous (hydrodynamic) drag force acting in opposition to the particles motion. In the case of nanoparticles, because of the very low Reynolds number, the drag force will be dominated by viscous effects and is given by Stokes' Law as $F_d = 6\pi\eta av$, where F_d is the drag force, η is the viscosity of the fluid, a is the radius of the colloidal particle, and v is the velocity at which the particle travels.¹⁷¹ The gravitational or buoyant force, F_g , for a colloidal particle whose density differs from that of the solvent by $\Delta\rho$ is given by $F_g = \frac{4}{3}\pi a^3 \Delta\rho g$, where g is the acceleration due to gravity. When the drag force and the gravitational force are in balance, the particle will have reached its terminal velocity. Therefore $F_g = F_d$ implies $\frac{4}{3}\pi a^3 \Delta\rho g = 6\pi\eta av_t$, and solving for the terminal velocity and replacing the acceleration due to gravity with the centrifugal acceleration ($\omega^2 r$) yields

$$v_t = \frac{2a^2 \Delta\rho \omega^2 r}{9\eta} \quad (2.1.)$$

where ω is the angular velocity and r is the distance from the center of the centrifuge to the particle. The terminal velocity of the nanoparticle is directly related to the square of the nanoparticle radius. Because of this, a nonlinear distribution of sizes would be present in the centrifuged sample and, to counteract this, a density gradient is used. This gradient, being denser toward the bottom of the centrifuge tube, will slow the motion of larger nanoparticles at greater depths in the tube by decreasing the value of $\Delta\rho$ in **Eq. 2.1**.

There are three primary techniques in which ultracentrifugation is used to separate nanoparticles; differential centrifugation, rate-zonal centrifugation, and isopycnic centrifugation (**Figure 2.4**).¹⁷² Differential centrifugation exploits the fact that larger and denser particles will sediment more quickly than their smaller and less dense counterparts. This method works well to achieve quick separations but does not achieve the degree of size purity of the other two methods. This is because some smaller particles will become trapped in the pellet that is formed from the larger sedimented particles. For the rate-zonal separation technique, a concentrated volume of the nanoparticles is placed at the top of a density gradient. As the separation begins, the larger nanoparticles will have a greater terminal velocity, per **Eq. 2.1**, and as a result will travel through the centrifuge tube more quickly. These particles can then be separated into discrete fractions. The final method, isopycnic DGU, has been quite successful in the purification of CNTs.^{145, 146} This method relies heavily on an accurate knowledge of the density of the material to be separated in order to develop a density gradient that spans that of the material. The density range of the gradient used must be such that the densest part of the gradient is denser than the material to be separated, and the least dense part of the gradient is less dense than the material of interest.

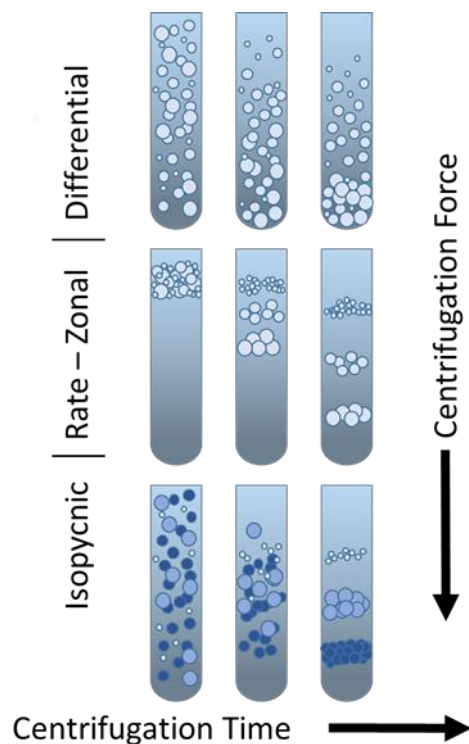


Figure 2.4. Nanoparticles can be separated by size or density through density gradient ultracentrifugation using differential centrifugation, rate-zonal centrifugation, or isopycnic centrifugation.

For all the methods described, once the nanoparticles have been separated based on the desired property (i.e. size or density), they will still need to be removed as an appropriately sized fraction to separate them from the rest of the sample. For differential centrifugation, the top layers of particles that did not precipitate can be decanted for a later spin, while the pellet can then be extracted. With isopycnic separations, one can separate each fraction by carefully inserting a syringe to the appropriate height, being careful not to disturb or shake the sample, to draw in the fraction of interest. In some cases, the previous method is not ideal, and instead of collecting a specific layer, each layer of the tube is drawn off consecutively from the top to bottom. This approach is ideal for rate-zonal separations. **Figure 2.5a** shows size-separated fractions of SiNCs

extracted using a rate-zonal separation with the jig used to extract each layer depicted in **Figure 2.5c**.

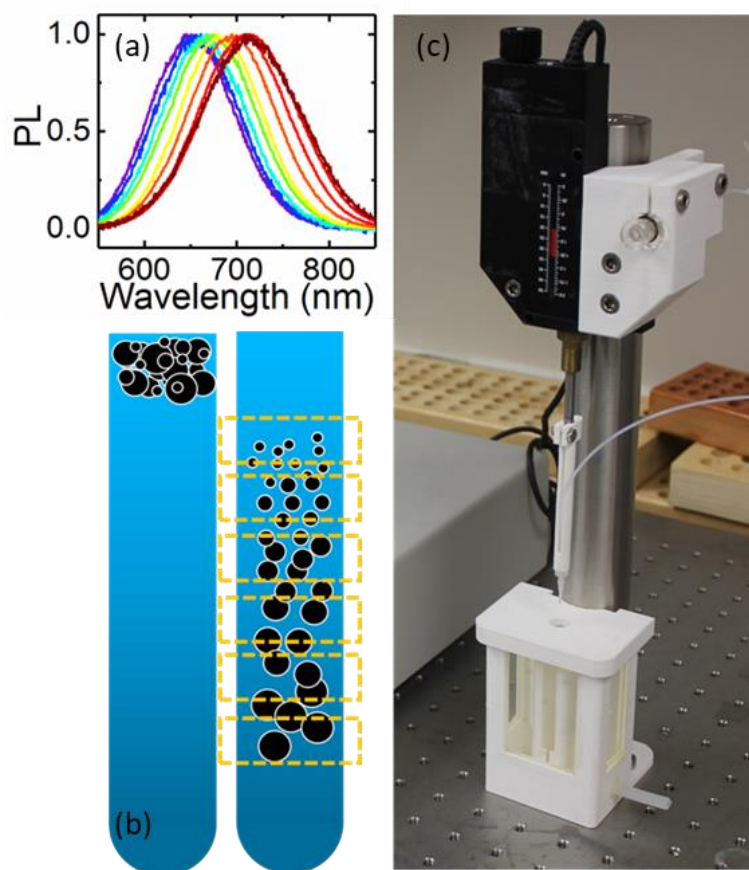


Figure 2.5. (a) The photoluminescence of silicon nanocrystals separated using density gradient ultracentrifugation with larger nanocrystals exhibiting red shifted gaussian photoluminescence. (b) To separate the as produced silicon nanocrystals, they are placed on top of a density gradient where, during ultracentrifugation, the nanocrystals move down the centrifuge tube. The nanocrystal terminal velocity is quadratically related to the nanoparticle radius, which is exploited to separate the nanoparticles based on size. (c) After the nanocrystals are size separated they are extracted layer by layer using a homemade jig.

CHAPTER 3. QUANTUM DOT PHYSICS

3.1. Introduction

The size dependent properties of quantum dots make them great candidates for applications in lighting, energy, and bio-fluorescent detection. On the most basic level, the size of the nanoparticles plays the largest role in their photophysics, yet various ligand schemes and shells have been shown to have a considerable impact on their photophysics. This chapter will discuss various quantum dot models, starting with the most basic, “a particle-in-a-box”, and then moving on to the more sophisticated and technical models that are used to quantify quantum dot photophysics.

3.2. Particle-in-a-Box

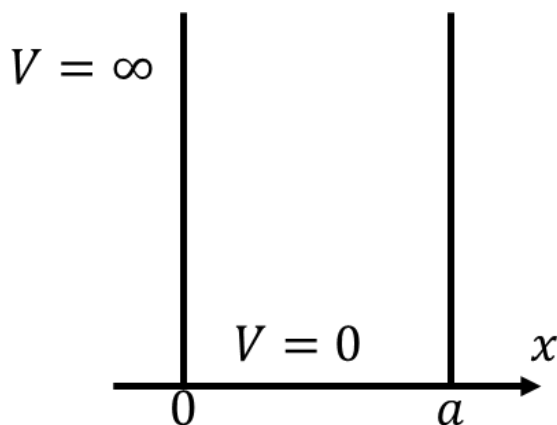


Figure 3.1. Model of a particle-in-a-box with infinite potentials outside the box and zero potential inside.

The particle-in-a-box model is one of the simplest applications of the Schrödinger equation, but it can portray one the most import aspects of quantum dot physics; the size dependent band gap. In this model, one assumes that an electron is bound to its nucleus, trapped inside a box of

length a . An infinite potential ($V = \infty$) exists outside of the box while there is no potential ($V = 0$) inside of the box (**Figure 3.1**). The Schrödinger equation for this example can be written as

$$\frac{d^2\psi}{dx^2} + \frac{2m}{\hbar^2}E\psi = 0 \quad (3.1.)$$

One can then assume that the wavefunction takes the general form of $\psi = A \exp[i\alpha x] + B \exp[-i\alpha x]$, where $\alpha = \left[\frac{2m}{\hbar^2}E\right]^{1/2}$. Determination of the constants A and B can be achieved by application of the boundary conditions. At $x \leq 0$ or $x \geq a$ the wavefunction must be zero ($\psi = 0$). Therefore, $0 = A \exp[0] + B \exp[0]$ which simplifies to $A = -B$. In the same fashion, at $x = a$, the wavefunction must also be zero, and therefore $0 = A \exp[i\alpha a] + B \exp[-i\alpha a]$. Using $A = -B$ and Euler's formula this can be simplified to $0 = 2Ai \sin \alpha a$, where we find that αa has infinitely many discrete solutions as

$$\alpha a = n\pi; n = 0,1,2,3 \dots \quad (3.2.)$$

$$\alpha = \frac{n\pi}{a}; n = 0,1,2,3 \dots \quad (3.3.)$$

Substituting $\alpha = \left[\frac{2m}{\hbar^2}E\right]^{1/2}$ into **Eq. 3.3** gives discrete energy values of

$$E_n = \frac{\hbar^2\pi^2}{2ma^2}n^2; n = 1,2,3 \dots \quad (3.4.)$$

where the wavefunction is

$$\psi(x) = \sin\left(\frac{n\pi}{a}x\right); n = 1,2,3 \dots \quad (3.5.)$$

Figure 3.1a plots the discrete wavefunctions from **Eq. 3.5** while **Figure 3.2b** plots the discrete energy levels from **Eq. 3.4**.

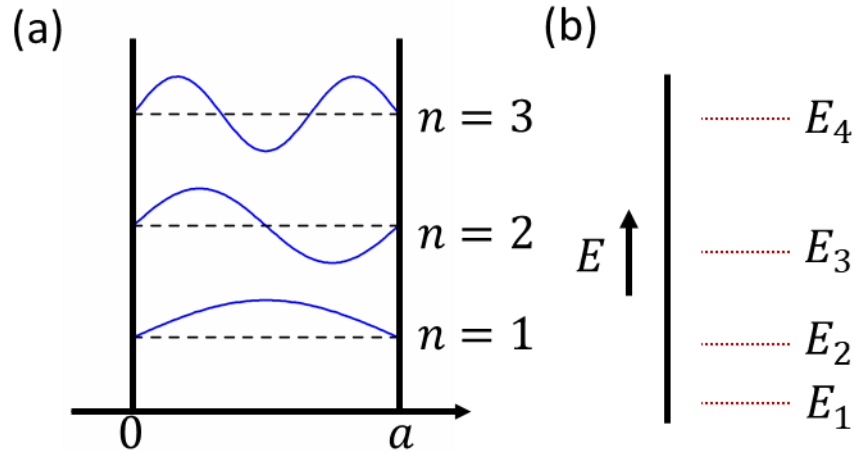


Figure 3.2. The solution to the particle-in-a-box model results in (a) simple sinusoidal wavefunction and (b) discrete energy levels.

From this model, we see two intriguing properties. Firstly, the discretization of the energy levels shows that there are certain energies that are forbidden to the electron. Secondly, we see that there is a quadratic relation between the energy and the size of the box (**Eq. 3.4**). This can be applied to a quantum dot, where the band gap quadratically increases as the size of the nanocrystal decreases.

3.3. Particle in a Periodic Potential

Although the previous model does a reasonable job of identifying the quadratic size dependence of the band gap in quantum dots, the discrete nature of the energy levels is more suitable for atomic electronic structure. The band structure of quantum dots can be more appropriately described using the Kronig-Penney model, which models an electron in a periodic potential, much like it would experience in a crystalline solid (**Figure 3.3**). Now in this case the potential is a constant value, $V = V_0$, and there are two different regions for the Schrödinger equation to be applied. The first periodic region has a width of b and is blue in **Figure 3.3**, while the second region is the space in between the potentials with a width of a . The Schrödinger

equation for these two regions are given in **Eq. 3.6** and **Eq. 3.7**, respectively, where $\alpha = \left[\frac{2m}{\hbar^2} E\right]^{1/2}$ and $\gamma^2 = \frac{2m}{\hbar^2} (V_0 - E)$.

$$\frac{d^2\psi}{dx^2} + \frac{2m}{\hbar^2} (E - V_0)\psi = 0 \quad (3.6)$$

$$\frac{d^2\psi}{dx^2} + \frac{2m}{\hbar^2} E\psi = 0 \quad (3.7)$$

Following a procedure similar to that in Chapter 4, Section 4 of the text “Electronic Properties of Materials” by Hummel¹⁷³ and using Bloch functions of the form $\psi(x) = u(x) \exp[ikx]$, one can arrive at

$$P \frac{\sin(\alpha a)}{\alpha a} + \cos(\alpha a) = \cos(ka) \quad (3.8)$$

where

$$P = \frac{maV_0b}{\hbar^2}. \quad (3.9)$$

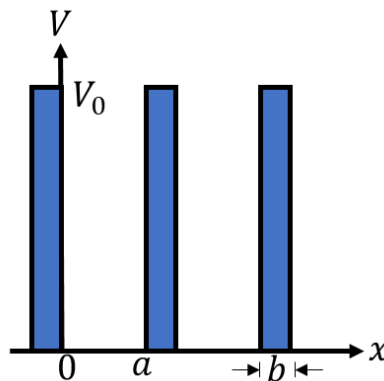


Figure 3.3. Periodic potential model.

In this case one again finds discrete solutions to αa , as in the previous example, and in order to better understand **Eq. 3.8** we plot the left-hand side as a function of αa in **Figure 3.4a**.

Now, because $-1 < \cos(ka) < 1$ we know that for **Eq. 3.8** to hold, $P \frac{\sin(\alpha a)}{\alpha a} + \cos(\alpha a)$ must also be between -1 and 1 . The possible values of αa are colored blue in **Figure 3.4a** and the possible energy levels according to **Eq. 3.6** and **Eq. 3.7** are plotted in **Figure 3.3b**. In a similar fashion to the discrete energy levels from the particle-in-a-box model, one can see that the energy bands increase in a quadratic fashion. Though, unlike the particle-in-a-box, energy bands as opposed to energy levels are now present, which more accurately describes the electronic structure in a quantum dot.

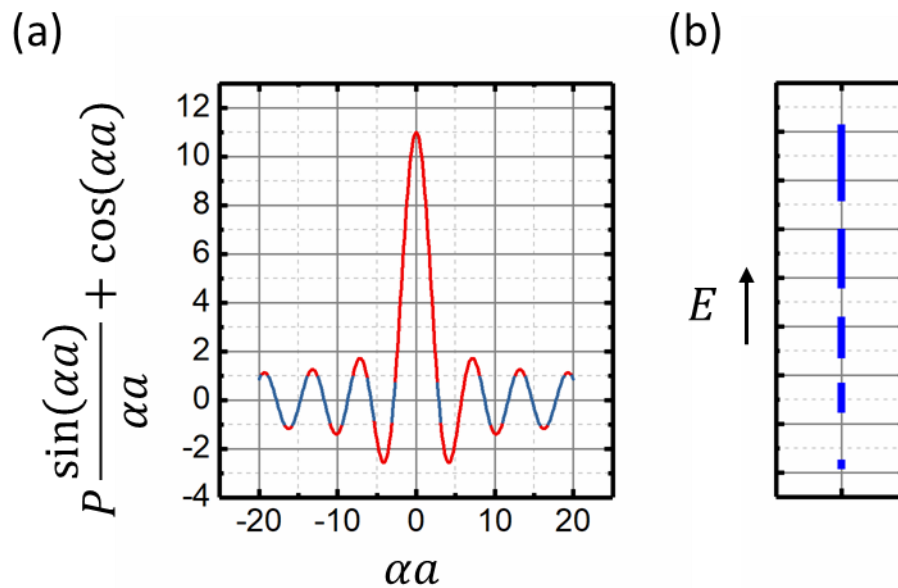


Figure 3.4. (a) The function $P \frac{\sin(\alpha a)}{\alpha a} + \cos(\alpha a)$ versus αa , where any value of this function that is between -1 and 1 is plotted in blue. (b) Energy bands form from this periodic potential model.

3.4. Multi-Electron Systems

In 1929, three years after the derivation of the Schrödinger equation, Paul Dirac noted that, “The general theory of quantum mechanics is now almost complete,... . The underlying physical laws necessary for the mathematical theory of a large part of physics and the whole of chemistry are thus completely known, and the difficulty is only that the exact application of these laws lead

to equations much too complicated to be soluble. It therefore becomes desirable that the approximated practical methods of applying quantum mechanics should be developed...”.¹⁷⁴ This is stated because the previous examples show examples of quantum mechanics being applied to a system with an exact solution as the result. Although this is useful for qualitative analysis and understanding, very few practical cases, as Dirac pointed out, have such simple solutions. Simply increasing the number of electrons from one to two greatly increases the complexity of the calculation. This section will briefly examine the modeling of helium-like atoms using simple approximations of the wavefunction to discuss the more complex methods used to computationally determine the electronic structure.

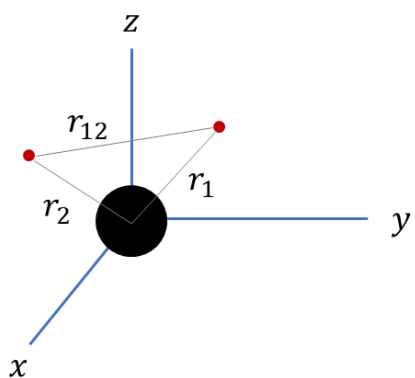


Figure 3.5. The coordinates of a helium atom with the nucleus at the origin.

Increasing the number of electrons surrounding the nucleus of an atom greatly increases the complexity of the Hamiltonian due to the increased number of electron-nucleus interactions and electron-electron interactions, making these calculations impossible to solve analytically. In the case of heliumlike atoms with a Hamiltonian of $\hat{H} = -\frac{\hbar^2}{2m_e}(\nabla_1^2 - \nabla_2^2) - \frac{1}{4\pi\epsilon_0}\left(\frac{Ze^2}{r_1} + \frac{Ze^2}{r_2} - \frac{e^2}{r_{12}}\right)$ where r_1 , r_2 , and r_{12} correspond to the distances between electrons and the nucleus per **Figure 3.5**, a few approximations can be taken to calculate the wavefunctions and corresponding energies

levels. Such approximations include ignoring the electron-electron repulsion term, $\frac{e^2}{4\pi\epsilon_0 r_{12}}$, and approximating the wavefunction as the product of two 1s orbitals, $\psi = \frac{1}{\pi^{1/2}} \left(\frac{Z}{a_0}\right)^{3/2} e^{-Zr_1/a_0} \frac{1}{\pi^{1/2}} \left(\frac{Z}{a_0}\right)^{3/2} e^{-Zr_2/a_0}$ without concern for spin.¹⁷⁵ These approximations can give reasonable calculations to the total energy of the helium atom at -74.8 eV when compared to the exact value of -79.0 eV. The approximation accuracy can be increased by adding higher order hydrogen orbitals such as the 2p, 3p, and 3d orbital or by using the variational method.¹⁷⁵

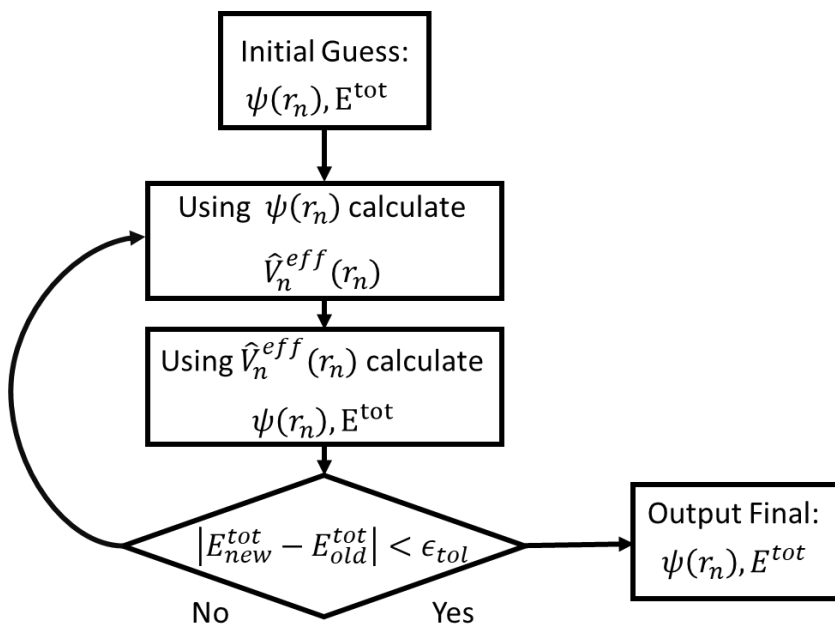


Figure 3.6. Algorithmic flow chart for the Hartree-Fock Method.

For systems with more than two electrons, the approximations used for calculating the total energy in the heliumlike atom also become too impractical. Because of this, the self-consistent field (SCF) method was introduced by Hartree.¹⁷⁶⁻¹⁷⁸ In this method an effective Hamiltonian, \hat{H}_n^{eff} , is developed for each electron, n , in the system. This electron only feels an effective

averaged potential, \hat{V}_n^{eff} , from the other electrons resulting in a Hamiltonian as such: $\hat{H}_n^{eff} = -\frac{\hbar^2}{2m_e}\nabla_n^2 - \frac{1}{4\pi\epsilon_0}\frac{Ze^2}{r_n} + \hat{V}_n^{eff}(\hat{r}_n)$.¹⁷⁵ The Schrödinger equation for an n -electron atom can now be separated into n one-electron equations which are solved using the SCF method outlined in **Figure 3.6**. First an approximation of the electronic wavefunction is made. This wavefunction is then used to calculate the effective potential where this effective potential is then used to calculate a new wavefunction. If the difference between the eigenenergies of the new and old wavefunctions is below the given tolerance, the new wavefunction and its corresponding eigenenergies give the desired output. This is the basis for the Hartree-Fock (HF) method. For a more accurate description of the electronic structure of a system, more advanced computational methods that include exchange correlation functions can be used, such as DFT. DFT builds upon the HF method by including an approximate treatment of the correlated motions of electrons and has been proven to be very practical in calculating the electronic structure of molecules and materials.¹⁷⁹⁻¹⁸¹ In the chapters to follow, many of the experimental data is corroborated with computational simulations using DFT.

CHAPTER 4. ON THE ORIGIN OF THE STRETCHED EXPONENTIAL PHOTOLUMINESCENCE RELAXATION IN SIZE SEPARATED SILICON NANOCRYSTALS

4.1. Introduction

SiNCs offer a potential green alternative to metal chalcogenide quantum dots due to the non-toxicity,⁹⁷ earth abundance, and technological familiarity of silicon. With opportunities for applications in photovoltaics,^{39, 41, 43, 100} LEDs,^{55, 56, 182, 183} and biological sensors,^{67, 184, 185} a thorough understanding of exciton recombination mechanisms in SiNCs will be important for optimizing their potential in future technologies. However, unlike the metal chalcogenides, bulk silicon has an indirect bandgap, which requires a finite momentum shift for radiative recombination. To complicate things further, additional much faster radiative decays have also been observed.^{111, 113, 115, 186} It has been demonstrated that hydrocarbon-passivated SiNCs can exhibit both slow (μs) and fast (ns) PL relaxation, where both modes appear to impact the overall QY.¹⁸⁶ Similarly, other groups have demonstrated that with appropriate passivation, surface related relaxation channels give rise to fast relaxation modes with nanosecond lifetimes.^{29, 30, 113} It is now commonly accepted that these surface effects can have considerable influence on the overall luminescent properties, leading to several interesting topics of research.¹¹⁴ For instance, Dasog and coworkers were able to exploit different passivation schemes to achieve ligand dependent emission across the entire visible spectrum.³⁰ In another recent study, Li *et. al.*, showed that surface related relaxation channels can be highly emissive, reaching QYs greater than 90 % while maintaining a relatively narrow full width at half max (FWHM).²⁹ Although several interesting and potentially fruitful opportunities related to the surface passivation of SiNCs exist, a complete understanding

of both the surface and core emission is necessary to further optimize the recombination dynamics of these potentially useful materials.

Linking specific emission pathways to either the core or surface of SiNCs has not been without controversy, yet the most modern pictures point to the long microsecond decay as arising from the core.^{30, 111, 113, 115, 116, 125, 126, 187} However, even within this widely accepted view, the stretched nature of the decay has not been fully reconciled or explained. Reported values for the stretching exponent vary from 0.4 to 1, with precise explanations invoking both size polydispersity or electron-phonon coupling.^{120, 121, 128} These challenges primarily arise from the indirect band structure of silicon, the sensitivity of the optical and electrical properties to surface passivation, and the challenges associated with synthesizing and preparing monodisperse samples. Synthetic methods for SiNCs^{103, 131, 136, 149, 168} are more complex or hazardous than the hot injection methods allowed by the metal-chalcogenide nanocrystals.⁵ This has led to the development of post synthetic size-separation methods, which are often necessary for probing the size dependent properties of SiNCs.^{107, 144}

In this work, we analyze both the solvated and solid state stretched microsecond decay of size-purified SiNCs by varying the spectral window of the measured response. Typically, the slow, microsecond radiative relaxation is modeled with the stretched exponential decay function, $I(t) = I_0 \exp \left[- \left(\frac{t}{\tau_{str}} \right)^\alpha \right]$. Here, we use the specific model formulated by Johnston to map the stretched exponential decay onto a continuous sum of exponential relaxations and the appropriate probability distribution function (PDF).¹⁸⁸ An interpretation of the stretched decay through a PDF and a continuous sum of exponential relaxations has been done previously,^{128, 189} as has the use of spectrally resolved lifetime measurements to study the radiative recombination kinetics of SiNCs.¹²¹ However, to the best of our knowledge, this is the first time that the two approaches

have been reconciled to analyze the radiative recombination dynamics of monodisperse, size-purified SiNCs. By doing so, we gain additional insight into the exciton-phonon coupling that underlies PL relaxation in quantum-confined SiNCs.¹⁹⁰

4.2. Results and Discussion

The SiNCs used here were chemically synthesized by annealing a silicon suboxide at 1100 °C as described in **Section 2.2.2**. The surface was passivated with 1-decene and then dispersed in hexane.¹⁴⁴ This produces nanocrystals that are approximately 3-4 nm in diameter, exhibiting size-dependent red PL (**Figure 4.1d**). The as produced SiNC solution had a solvent dependent QY of approximately 20 % in hexane, and although the colloidal SiNCs were stored in an inert atmosphere, a drop in QY, a slight blue shift in the PL, and the emergence of a weak blue emission pathway occurred over time, which we attribute to age-related processes such as oxidation. Aliquots of the parent sample were dispersed in various solvents under an inert atmosphere to limit oxidation. The dried samples were then dispersed in similar volumes of various solvents such as tetrahydrofuran (THF), toluene, and hexane; and the subsequent QY was measured (**Figure 4.1a**). Hexane showed the highest quantum yield, followed by toluene and then THF, which showed a considerable drop in the overall QY. One possible explanation for the observed drop in PL efficiency is surface oxidation resulting from the solvent itself. However, if this were the case one would expect that the drop in QY would be irreversible due to the permanent nature of oxidation. Yet, when one aliquot was 1) dispersed in hexane, 2) dried under inert conditions, 3) dispersed in THF, 4) dried again under inert conditions, and 5) re-dispersed in hexane, a degree of reversibility in the QY was observed (inset of **Figure 4.1a**). Although the sample did undergo a degree of irreversible degradation, there was an increase in the final QY relative to the QY in THF, indicating that this quenching was reversible and solvent specific. To further probe this, we measured the QY

of the parent material in several more solvents as reported in **Table 4.1**. Plotting the QY as a function of solvent donor number (**Figure 4.1b**) suggests that a larger donor number corresponds to a lower QY.

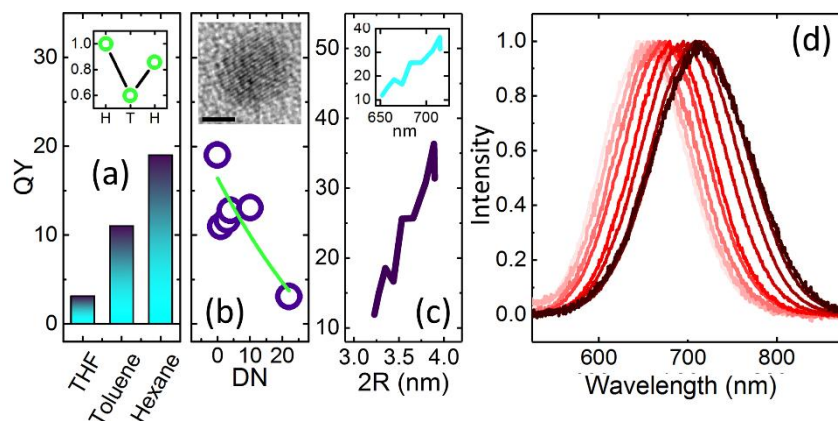


Figure 4.1. QY of as produced SiNCs in various solvents, where the inset shows the QY in hexane (H), THF (T) and then in hexane (H) again, with the vertical axis normalized to the initial QY in hexane. (b) QY as a function of donor number for SiNCs dispersed in several different solvents. The inset is a TEM image of a single nanocrystal (scale bar is 2 nm). (c) The QY of size separated super fractions as a function nanocrystal size and peak emission wavelength (inset). (d) PL spectrum of each super fraction.

Recent experimental work by Wheeler *et al.*, suggests that hypervalent bonding of the solvent (e.g. 2-butanone) through either the carbonyl- or nitrile- functional group to chlorine-passivated plasma-synthesized SiNCs effectively induces colloidal stability without the need for a long carbon chain passivating layer.¹⁹¹ Similarly, Shu *et al.* explained the dramatic increase in the PL of plasma synthesized SiNCs by describing a similar hypervalent interaction of silyl groups with the nanocrystal surface.¹²³ By heating the solution of SiNCs to relatively low temperatures (< 200 °C) they detected the desorption of such moieties from the nanocrystal surface as well as a corresponding substantial increase in PL. Conical intersections caused by changes to the potential energy surface due to hypervalent interactions were used to explain the substantial decrease in the observed PL when silyl moieties are present.¹²³

Table 4.1. Solvent and Corresponding Quantum Yield

Solvent	QY
THF	3.1
Toluene	11.6
1,2 Dichlorobenzene	11.7
Mesitylene	13.1
<i>m</i> -Xylene	14.5
Hexane	19.0

Furthermore, theoretical work by the Levine group has shed light on the impact that different defects have on the optical properties of SiNCs,¹²²⁻¹²⁴ with the finding that oxidation in SiNCs can open conical intersections that allow for an efficient non-radiative recombination channel. In the QY vs. solvent data presented here, a similar argument can be made. One could imagine that certain solvents would interact with the SiNC surface through hypervalent bonding. This interaction alters the native potential energy surface, resulting in a non-radiative conical intersection that subsequently reduces the overall QY. A solvent with a higher donor number would interact more strongly with the SiNC surface, causing a greater number of non-radiative pathways, which would in turn cause a greater decrease in QY (**Figure 4.1b**). Another possible explanation could invoke dielectric stabilization of the localized wavefunction at surface oxidation sites. As predicted by the Levine group, higher dielectric constant solvents stabilize the localized wavefunction near such a defect, increasing the likelihood of recombination through this type of channel.¹²⁴ In the simplest models, the QY can be related to the non-radiative (k_{nr}) and radiative (k_r) recombination rates as $QY = k_r / (k_r + k_{nr})$ with $\tau = (k_r + k_{nr})^{-1}$.¹²⁷ This would imply that higher dielectric constant solvents would increase k_{nr} and lower the overall QY.

Turning our attention to the precise mechanism of radiative relaxation in SiNCs, monodisperse ‘super-fractions’ were prepared by separating the as produced material into size-

resolved fractions using DGU. The DGU purification process was done nine separate times and individual fractions with near identical PL spectra were combined to form ‘super’ fractions. Each such fraction was labeled as SA, SB, SC for super-fraction A, super-fraction B, super-fraction C, ect. The PL of each super fraction can be seen in **Figure 4.1d**, where the wavelength of peak emission increases with size, typical of a quantum confined system. We used hexane, the solvent that induces the least amount of non-radiative relaxation, and measured the QY of each fraction. The inset to **Figure 4.1c** shows the QY as a function of the peak emission wavelength, while QY vs. size is plotted in **Figure 4.1c**, where the conversion from peak emission energy to nanocrystal size R was executed through $E = E_o + \frac{3.73}{(2R)^{1.39}}$ with $E_o = 1.17$ eV.¹⁰⁶ We note that the highest QY of the fractions, 40 %, is well above that of the parent suspension and that the QY quickly diminishes as the size of the nanocrystal decreases, indicating an increasing number of non-radiative relaxation channels.

The time dependent PL relaxation kinetics of each size-resolved SiNC suspension (excluding SA and SB for which the QY was deemed too low) were measured in two different states (solid and solvated) and the data were fitted with a stretched exponential relaxation; $I_{cont}(t) = A \exp[-(t/\tau_{str})^\alpha]$. In the solution state, the measured decays were spectrally resolved (SR), *i.e.* a monochromator was used to allow only the peak spectral emission from the samples to reach the detector (5 nm resolution). Slight difference was observed between the solution and solid-state decays. However, when comparing the SR peak emission to the full spectrum (FS) emission, the lifetime and stretching exponent both substantially increased, with α approaching 1 for the SR emission. (**Figure 4.2a**). The parameters τ_{str} and α are shown as a function of peak emission wavelength in **Figures 4.2c-d**.

To facilitate numerical interpolation, the data in **Figures 4.2c-d** were fit with a quadratic function of the form $y = A + Bx + Cx^2$. Because there was a negligible difference between the response of the solution vs. solid state but a strong dependence on the detection scheme (FS vs. SR), the FS data were fit to a quadratic function that included both solution and solid-state data, while the SR data was fit to a separate and distinct quadratic function. The quadratic fitting schemes have no physical significance but are used in the analysis to interpolate lifetime and stretching exponent as a function of peak emission wavelength.

Stretched exponential functions are typically used to model a system that contains a distribution of decay rates and lifetimes.¹⁹² Hence, the stretched exponential relaxation function can be written as a continuous sum of distinct exponential decays weighted by the appropriate PDF;

$$I_{cont}(t) = \exp\left[-\left(\frac{t}{\tau_{str}}\right)^\alpha\right] = \int_0^\infty P(s, \alpha) \exp\left[-\left(s \frac{t}{\tau_{str}}\right)\right] ds, \quad (4.1.)$$

where $P(s, \alpha)$ is the PDF, $s = \frac{\tau_{str}}{\tau}$ is a dimensionless rate, and $I_{cont}(t)$ is the total intensity at time t . The normalization of the PDF is chosen such that $\int_0^\infty P(s, \alpha) ds = 1$. The PDF can also be expressed as¹⁸⁸

$$P(s, \alpha) = \frac{1}{\pi} \sum_{n=1}^{\infty} \frac{(-1)^{n+1} \Gamma(n\alpha + 1)}{n! s^{n\alpha+1}} \sin(n\pi\alpha). \quad (4.2.)$$

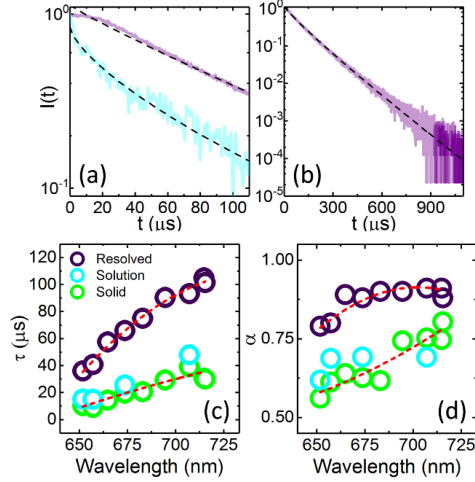


Figure 4.2. (a) Full-spectrum and spectrally resolved photoluminescence decay measurements of fraction SI fit with a single stretched exponential decay. (b) The same spectrally resolved decay from (a) with an expanded time scale. The full-spectrum and spectrally resolved photoluminescence lifetime (c) and stretching exponent (d) for each super-fraction plotted as a function of peak emission wavelength (note the curves are quadratic fits).

Johnston¹⁸⁸ gives significantly more detail on the origin of **Eq. 4.2** and the curious reader is directed to Ref. [188] for more details. For computational purposes, **Eq. 4.1** can be approximated as a discrete sum of exponential decays through

$$I_{cont_{FS}}(t) \approx I_{disc_{FS}}(t) = \sum_{i=1}^{\infty} P_{s_i}(\alpha) \exp \left[- \left(s_i \frac{t}{\tau_{str}} \right) \right] \Delta s. \quad (4.3.)$$

Adjusting the upper and lower limit, UL and LL , respectively, effectively acts as a theoretical lifetime ‘filter’ to map the decays in a SR measurement to their corresponding location in the PDF.

Thus, **Eq. 4.3** can be written as

$$I_{disc_{Res}}(t) = \sum_{i=LL}^{UL} P_{s_i}(\alpha) \exp \left[- \left(s_i \frac{t}{\tau_{str}} \right) \right] \Delta s. \quad (4.4.)$$

For the FS configuration, PDFs were generated from **Eq. 4.2** using Mathematica® and are plotted in **Figure 4.3a**. To demonstrate the equivalence of **Eq. 4.1** and **Eq. 4.4**, Mathematica® was again used to generate stretched exponential decays from **Eq. 4.4**, where the PDF used was on either

side of the experimentally relevant window, $\alpha_{FS} = 0.60$ and $\alpha_{FS} = 0.80$. An LL of 0.1, a UL of 20, and $\Delta s = 0.1$ were used to achieve a reasonable approximation to **Eq. 4.1**, as shown in **Figure 4.3b**. Johnston noted that the UL is related to τ_{FS} , and even though the function was summed to $UL = 20$ – significantly past the relevant decays – the fact that the summation is not infinite, combined with the discrete nature of **Eq. 4.4**, lead to the observed discrepancy between $I_{cont}(t)$ and $I_{disc}(t)$.

Simply changing UL and LL in **Eq. 4.4** can drastically alter the resulting decay. **Figures 4.4a-b** show the result from **Eq. 4.4** with the LL and UL set to 0.1 and 20, respectively, for $\alpha_{FS} = 0.60$ (**Figure 4.4a**) and $\alpha_{FS} = 0.80$ (**Figure 4.4c**) indicated in black. The colored background decays are matched with the corresponding region of the PDF found in **Figures 4.4b & e**. For example, a lower limit of $s = 0.01$ and an upper limit of $s = 0.10$ in **Figure 4.4b** is blue and corresponds to the longest blue decay in **Figure 4.4a**, while in a similar fashion setting the limits to $LL = 1.91$ and $UL = 2.00$ corresponds to the yellow part of the PDF and the corresponding decay. By changing the upper and lower limits in the sum, one can effectively modify the resulting decay curve. Furthermore, $P(s, \alpha_{FS})$ was converted to $P(\tau, \alpha_{FS})$ by noting that $s = \frac{\tau_{str}}{\tau}$ and then interpolating τ_{str} from **Figure 4.2c**. These are again color coded so that the appropriate limits match the resulting curve, $I_{discSR}(t)$.

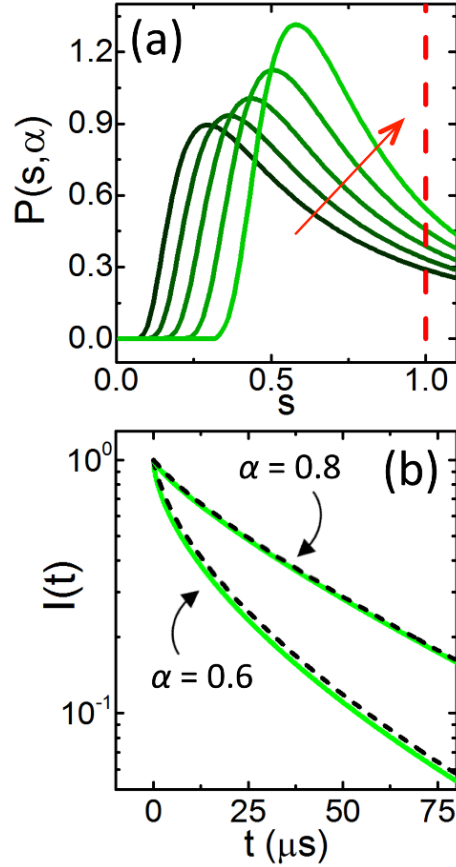


Figure 4.3. (a) Probability distribution functions for $\alpha = 0.6$ to $\alpha = 0.8$ increasing by increments of 0.05 in the direction of the red arrow. (b) Comparison of $I_{\text{cont}}(t)$ (solid lines) and $I_{\text{disc}}(t)$ (dashed lines) for $\alpha = 0.6$ and $\alpha = 0.8$ with lifetime values interpolated from the quadratic fits in **Figure 4.2**.

The stretched lifetime, τ_{str} , is commonly assumed to be either the most probable or the average lifetime τ , but it becomes apparent that this is not the case, as the most probable lifetime (the peak of the PDF) significantly differs from τ_{str} (black dotted lines in **Figure 4.4**). There is almost an order of magnitude difference between the most probable decay time and τ_{str} . The distribution of decay times matches intuition, however. As $\alpha \rightarrow 1$, the width of the PDF also decreases and approaches a delta function.

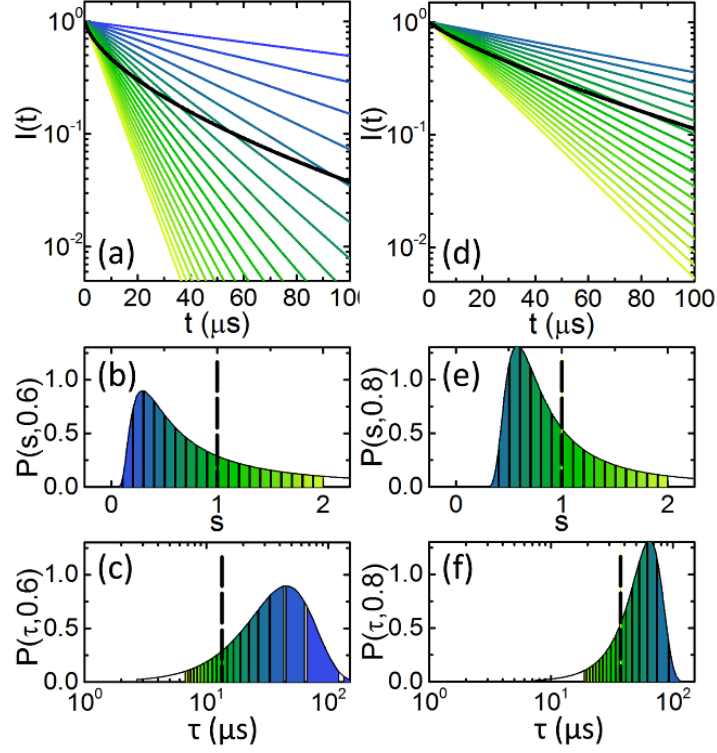


Figure 4.4. (a) Decay curve $I_{\text{disc}}(t)$ computed for $\alpha = 0.6$. The color-coded (yellow to blue) curves are the corresponding contributions from each lifetime in the distribution, which is shown both in terms of (b) dimensionless rate and (c) lifetime. (d)-(f) A similar set of plots for $\alpha = 0.8$. The vertical lines correspond to the values of τ_{str} indicated in **Figure 4.3**.

We then set out to fit the SR data using **Eq. 4.4** by only modifying the upper and lower limit:

$$I_{\text{cont}_{SR}}(t) = \exp\left[-\left(t/\tau_{\text{str}_{SR}}\right)^{\alpha_{SR}}\right] \approx \sum_{i=LL}^{UL} P_{S_i}(\alpha_{FS}) \exp\left[-\left(s_i \frac{t}{\tau_{\text{str}_{FS}}}\right)\right] \Delta s. \quad (4.5.)$$

The results are shown in **Figure 4.5**, where the full spectrum PDF is plotted as a function of τ for α_{FS} ranging from 0.60 to 0.80 in steps of 0.05. The vertical dashed blue and green line represents $\tau_{\text{str}_{FS}}$ and UL in **Eq. 4.5**, respectively (note that s and τ are the inverse of each other). The FS stretched lifetime increases in accordance with **Figure 4.2c** while UL similarly increases as a function of peak emission (**Figure 4.6b**).

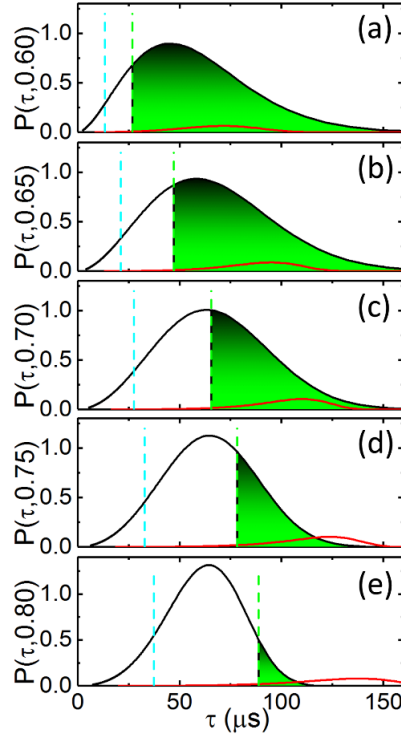


Figure 4.5. Full-spectrum probability distributions (solid black lines) and spectrally resolved probability distribution functions (red curves) for (a) $\alpha = 0.60$, (b) 0.65, (c) 0.70, (d) 0.75, and (e) 0.80. The vertical blue and green dashed lines represent τ_{str} and the cutoff, respectively. The shaded region is the portion used to approximate the SR data from the full distribution.

Interestingly, as the size of the nanocrystal increases so does the lower limit of lifetimes used to fit the spectrally resolved data (**Figure 4.6**), indicating that a small subset of the total decays make up the majority of the observed PL. At the same time, α_{FS} is also increasing and thus the PDF is becoming narrower towards the upper end of the spectral window examined in this study. As mentioned earlier, a simple model relating the QY to lifetime is $QY = k_r / (k_r + k_{nr})$ with $\tau = (k_r + k_{nr})^{-1}$. Typically, τ_{str} is compared to the QY to demonstrate this relationship, but we can see that τ_{str} does not represent the most meaningful decay time. Rather, a more appropriate value is the most probable decay time, which is shown in **Figure 4.7a**. The most probable decay time was thus found from the PDFs of **Figure 4.5** and is plotted next to the solvated QYs of the fractions in **Figure 4.7b**, demonstrating reasonable qualitative agreement.

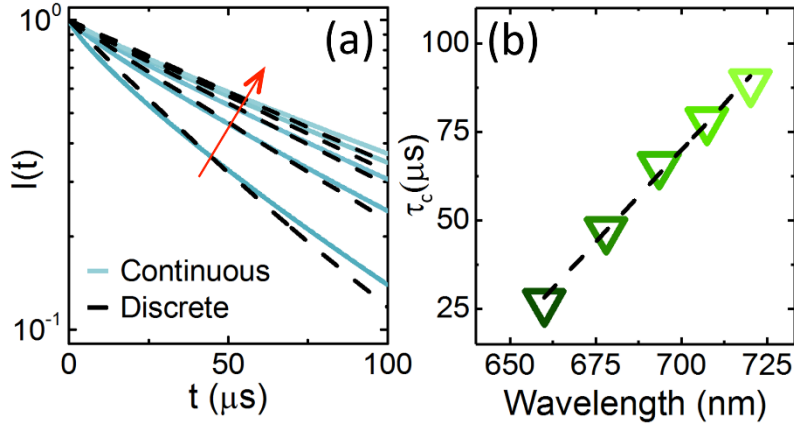


Figure 4.6. (a) $I_{\text{cont}}(t)$ from the spectrally resolved data (solid blue line) and $I_{\text{disc}}(t)$ from the full-spectrum data with lower limit cutoffs applied (dashed black line). (b) The lower limit cutoffs used in (a).

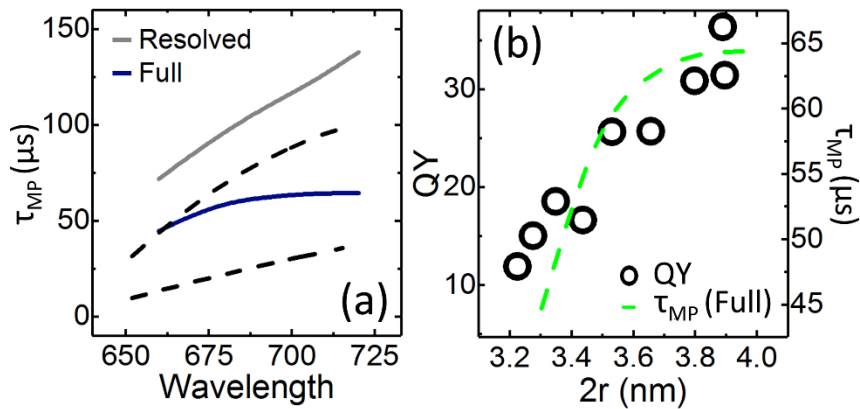


Figure 4.7. (a) Most probable photoluminescence lifetime for the resolved (gray curve) and full-spectrum (blue curve) data along with τ_{STR} from **Figure 4.2c** (black dashed curves). (b) The quantum yield for each fraction and the most probable lifetime for the full-spectrum data (green dashed line).

For further analysis of the stretched nature of PL relaxation, linear variable filters (LVFs) were used to select a ‘blue’, ‘peak’, and ‘red’ region of the PL spectrum and the subsequent spectrally resolved PL relaxation was measured. The results are shown in **Figure 4.8** for fraction SF. From this data, we see that the mapping of PL to PDF is such that higher energy photons correspond to shorter decay times and lower QY, while lower energy photons correlate with longer decay times and higher QY. Furthermore, the emission that is spectrally weighted toward the

‘peak’ and the ‘red’ end of the PL spectrum exhibits a stretching exponent closer to 1, while that closer to the ‘blue’ end of the spectrum is more stretched. Because the SiNCs used here are relatively monodisperse, we can ascribe the majority of the PL spectral line-width to electron-phonon coupling and the indirect nature of the bandgap. In this view, the results in **Figure 4.8** are telling and can be qualitatively interpreted within the context of a simple model of electron-phonon coupling.¹⁸⁶ For a given SiNC fraction or nanocrystal size, the ‘redder’ emission is more radiatively efficient and corresponds to a transition from the bottom of the band edge and the subsequent emission of a phonon to satisfy momentum conservation. In contrast, the ‘bluer’ emission is less radiatively efficient and corresponds to stronger phonon coupling from a slightly higher energy state associated with higher-order structure just above the band edge and/or the absorption of a phonon or even multiple phonons. In this simple picture, as nanocrystal size decreases, the latter effect would become more prominent.

4.3. Conclusion

Using size-resolved SiNC fractions dispersed in the optimal solvent for efficient radiative recombination, we have examined the role of nanocrystal size and spectral resolution in the slow, stretched-exponential PL relaxation of colloidal SiNCs. Based on the stretching exponents deduced from the measured PL decay, and using a concise model of stretched-exponential relaxation available in the literature, we were able to extract the PDF for radiative decay time as a function of both nanocrystal size and the energy of the emitted photons. Our results suggest a correlation between larger nanocrystals, ‘stretching’ exponents closer to unity, longer PL lifetime, and more efficient emission. For a given nanocrystal size, our results also suggest that the spectral portion of the PL that resides both near and on the ‘red’ or lower-energy side of the emission peak corresponds to a lesser degree of ‘stretching’, longer PL lifetime, and higher emission efficiency.

In contrast, the emission on the ‘bluer’ or higher-energy side of the PL peak correlates with shorter decay time, a greater degree of stretching, and lower overall emission efficiency. Because the fractions are monodisperse, we suggest that the underlying mechanism relates predominantly to nature of electron-phonon coupling. Our results help further clarify the multi-exponential nature of PL relaxation in nanocrystalline silicon while potentially providing additional insight into how the quantum yield might be further optimized.

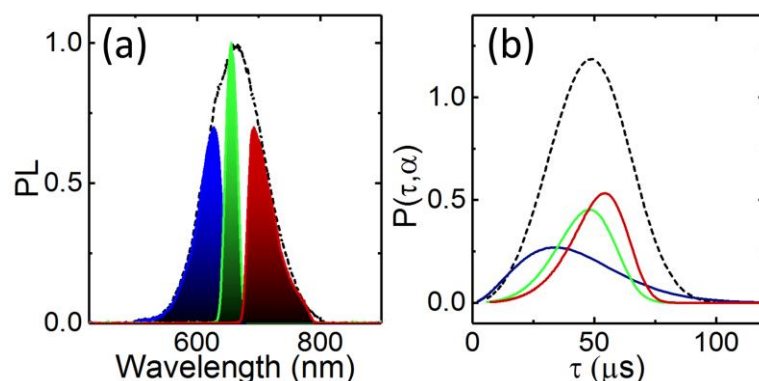


Figure 4.8. (a) Photoluminescence spectrum of fraction SF (black) and the three spectrally resolved regions used to measure photoluminescence relaxation. (b) The probability distribution function extracted from the stretched exponential relaxation based on the full spectrum (black), the ‘blue’ region (blue, $\alpha = 0.6$), the ‘peak’ region (green, $\alpha = 0.83$) and the ‘red’ region (red, $\alpha = 0.86$).

4.4. Experimental Methods

Synthesis and Size Separation: SiNC were synthesized from solution using methods described elsewhere.¹⁴⁴ Briefly, silicon tetrachloride was exposed to a controlled amount of water under a nitrogen atmosphere to create a silicon suboxide. This was then annealed in a tube furnace under a slightly reducing atmosphere of 5 % N_2 and 95 % Ar. Under these conditions, the silicon suboxide decomposes into SiNCs encased in a silicon dioxide layer. A mortar and pestle were used to mechanically breakdown the composite and then HF acid was used to liberate the nanoparticles from the silicon dioxide layer. The bare nanocrystals were transported to a round bottom flask

connected to a Schlenk line and then passivated with 1-decene *via* thermal hydrosilylation. Once passivated, the SiNC were separated into distinct fractions based on diameter as detailed in recent publications.^{108, 193, 194} Size purification was achieved through DGU using a Beckman Coulter centrifuge with a Ti41 rotor. A step gradient of 50 %, 60 %, 70 %, 80 %, and 90 % chloroform in m-xylene was used as the transport and separation medium for the nanocrystals. Nine different spins were conducted with speeds and times ranging from 30k-41k RPM and 10-35 hours, respectively, with the rate of 35k RPM and a time of 24 hours being used for most separations. Solution state PL was determined for the fractions of all nine spins and fractions of comparable peak emission were then combined to form super fractions.

Characterization: The super fractions were optically characterized in both the solvated and solvent free state, where the QY, PL and lifetime (spectrally resolved and full spectrum) were measured. For all solvent exchange processes carried out herein, an inert atmosphere of nitrogen was used to ensure the limited oxidation of the SiNCs. For all QY measurements, an integrating sphere was used with a fiber-coupled 20 mW Omicron PhoxX 375 nm laser for excitation and an Ocean Optics QE65000 spectrometer for detection. FS solvent-free lifetime measurements were conducted on a custom inverted microscope with a 60x water immersion objective and an in-house built sample holder using modulated pulsed excitation at 375 nm delivered through a notch filter at a rate of 1-5 kHz (Advanced Laser Diode Systems, PiL037, 30 ps pulse width, 140 mW peak power). A photomultiplier tube was coupled to a digital oscilloscope for detection. FS solution state lifetime measurements were performed using the same excitation and detection sources as the FS solvent-free samples previously mentioned, but on a customized upright microscope with a 4x objective. Delta LVFs with an in-house modified Ocean Optics LVF mount were positioned before the detector for the spectrally resolved measurements. Solution-state SR lifetime

measurements were collected using a Horiba Jobin Yvon Fluorolog-3 spectrofluorimeter with a 450-W xenon short-arc excitation source that was mounted vertically in an air-cooled housing. An off-axis mirror was used for light focusing and collection with double-grating excitation and emission Czerny-Turner spectrometers, kinematic classically ruled gratings, and all-reflective optics. The detector was an R928P for high sensitivity in photon-counting mode. For all lifetime measurements, the mean excitation power per unit area was kept well inside the regime of linear PL response. A JEOL JEM-2100 analytical transmission electron microscope operated at 200 kV with a GATAN Orius SC1000 CCD was used for all electron microscopy images.

CHAPTER 5. SIZE DEPENDENT BIMODAL DECAY IN SILICON NANOCRYSTALS

5.1. Introduction

The nature of PL in SiNCs has been an ongoing debate for the last 20 years since the first discovery of room temperature PL in silicon quantum wires by Canham.²¹ Part of the challenge in understanding the PL comes from the fact that at least two very different decay mechanisms exist, namely a fast and slow decay.^{30, 108, 109, 111, 121, 185} The assignments and explanations of these decay mechanisms have been diverse, ranging from surface related effects,^{30, 115, 195} impurities,¹¹¹ direct or quasi-direct behavior,^{112, 196} to core related effects.¹²⁶ To better understand this dichotomy, this chapter explores the size and temperature dependence of these two decay modes for plasma synthesized SiNCs purified by size through DGU.

5.2. Results and Discussion

As produced plasma-synthesized SiNCs were separated into fractions *via* DGU using a two-solvent density gradient. Specifically, a five-layer step gradient of 50 %, 60 %, 70 %, 80 % and 90 % chloroform in *m*-xylene were used with custom polyvinylidene fluoride ultracentrifugation tubes. After spinning for 14.5 hours at 30,000 rpm, the nanoparticles were extracted into 200 μ L fractions throughout the length of the ultracentrifuge tubes using a handheld pipette with a handmade pipette tip. **Figure 5.1a** shows the PL of the different solvated fractions while **Figure 5.1b** shows the lifetime of drop-cast size-separated fractions, where the two decay modes can easily be seen in the smallest fraction with a peak emission at 1.92 eV.

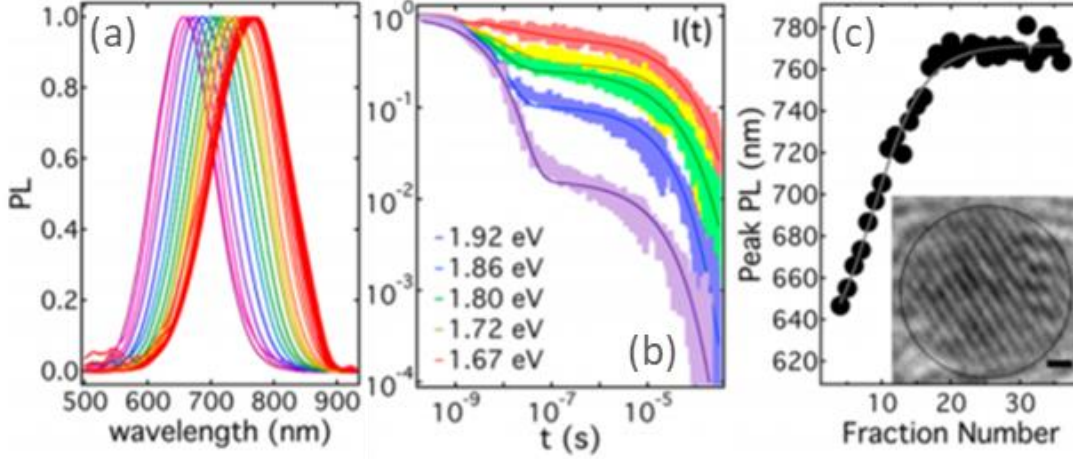


Figure 5.1. Room temperature (a) photoluminescence and (b) photoluminescence relaxation of size-separated, plasma-synthesized silicon nanocrystals with the (c) peak emission as a function of fraction number. A transmission electron micrograph of a plasma synthesized silicon nanocrystal can be seen in the inset of (c) with a scale bar of 1 nm. Reprinted with permission from Ref. [186]. Copyright 2018 American Chemical Society.

To find the lifetimes of the size-separated fractions, a stretched double exponential equation was fit to the time dependent decay,

$$I(t) = A_1 \exp[-(t/\tau_1)^{\alpha_1}] + A_2 \exp[-(t/\tau_2)^{\alpha_2}], \quad (5.1.)$$

where τ , α and A correspond to the lifetime, stretching exponent, and amplitude for each decay, respectively, and the subscripts 1 and 2 stand for the slow and fast decay, respectively. The stretching exponent α_2 is approximately 0.60 with little dependence on size, while α_1 varies from 0.5 to 0.8, increasing with size. Sanghaleh *et al.* suggested that the microsecond stretched behavior arises from polydispersity in the sample size¹²¹ and variations in structure.¹²⁰ However, the fact that we still observe a stretched-exponential relaxation for size-purified SiNCs suggests other factors, such as electron-phonon coupling, that are more intrinsic.¹¹⁰

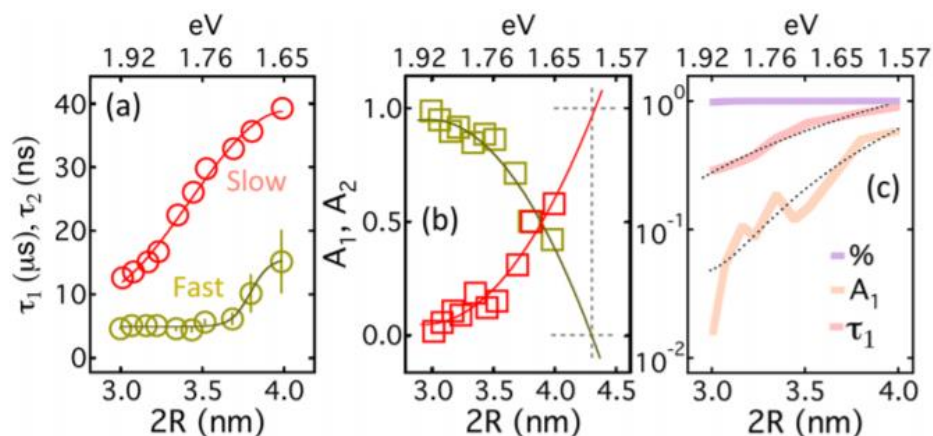


Figure 5.2. The photoluminescence relaxation fitting parameters of size-separated silicon nanocrystals based on Eq. 5.1, with the (a) fast and slow lifetimes and the (b) fast and slow amplitudes. The (c) quantum yield, slow decay lifetime and slow decay amplitude plotted as a function of size. Reprinted with permission from Ref. [186]. Copyright 2018 American Chemical Society.

Figure 5.2a shows both the fast and slow lifetimes as a function of size, where the slow decay has a strong, nearly exponential, relationship with nanocrystal diameter while the fast decay, although not completely independent of size, indicates little variation. In **Figure 5.2b**, the amplitudes of the fast and slow decay are plotted as a function of size, where the size of the SiNCs was determined from the PL.¹⁰⁶ The size of the nanocrystal and A_1 and A_2 are directly and indirectly related, respectively. Extrapolations of these two trends show that as the nanocrystals approach the exciton Bohr radius of silicon, the slow decay would completely dominate ($A_1 = 1$ and $A_2 = 0$).

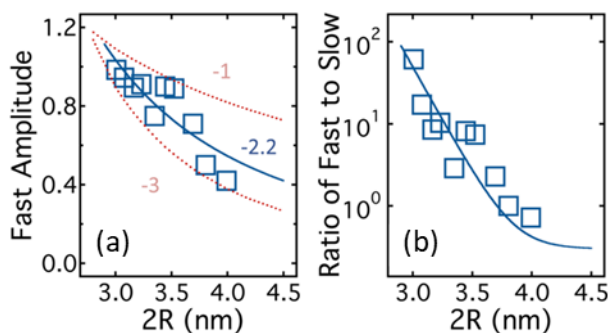


Figure 5.3. (a) The amplitude of the fast decay has a strong dependence on size with (b) the ratio of the fast to slow amplitude having an exponential relationship with size. Reprinted with permission from Ref. [186]. Copyright 2018 American Chemical Society.

By utilizing two different passivation methods, Yang *et al.* suggested that the fast decay was the purely the result of surface oxidation.¹⁸⁷ The first passivation technique, thermal hydrosilylation, is able to achieve higher surface coverage compared to the second technique, photoinitiated hydrosilylation. Passivating two identical samples by the two different methods allows for an indirect measure of the impact of surface oxidation. The authors observed only the slow microsecond decay for the thermally passivated sample while the photoinitiated sample exhibited both the slow and fast decay channel.¹⁸⁷ They concluded that the fast decay was purely the result of surface oxidation as a result. However, our data suggest a more complex picture, as A_1 shows strong nanocrystal size dependence, scaling as $R^{-2.2}$ (**Figure 5.3a**), while in **Figure 5.3b**, the ratio of the amplitudes A_2/A_1 is fit with an exponential. If the slow microsecond decay was solely the result of core electron-hole recombination and the fast decay was the result of surface oxidation, one would expect a relationship reflecting the surface to volume ratio, $A_2/A_1 = 1/R$. The trend in **Figure 5.3b**, however, is much stronger, indicating that the simple appearance of surface states is likely not a complete explanation

To further probe the two decay modes, temperature dependent emission spectra were taken on two distinct monodisperse samples at either end of the size window, denoted as “small” and “large”. **Figure 5.4a – b** shows the temperature dependent PL spectra of the small and large sample, respectively, starting at room temperature and cooling by consecutive 20 K increments down to liquid nitrogen temperatures (80 to 90 K). The small sample’s PL has a much greater coupling to the temperature when compared to the large sample, which will be discussed in greater detail in **Chapter 6**.¹⁰⁸ Furthermore, time dependent PL measurements as a function of temperature were taken for these two distinct samples (**Figure 5.4c – d**). As before, the decays were fit with a

double stretched exponential decay (Eq. 5.1) and Figure 5.5 shows the results. Parallel to what was seen in the size-resolved lifetime data, the slow lifetime shows strong temperature dependence while the fast decay has little coupling to temperature. Figure 5.5c shows the ratio of the slow to fast amplitude as a function of temperature for the small and large sample. This ratio increases exponentially upon cooling with $\frac{A_1}{A_2} \propto \exp\left[-\frac{T}{k_B T_0}\right]$, where $k_B T_0$ is approximately 4 meV and 6 meV for the small and large sample, respectively.

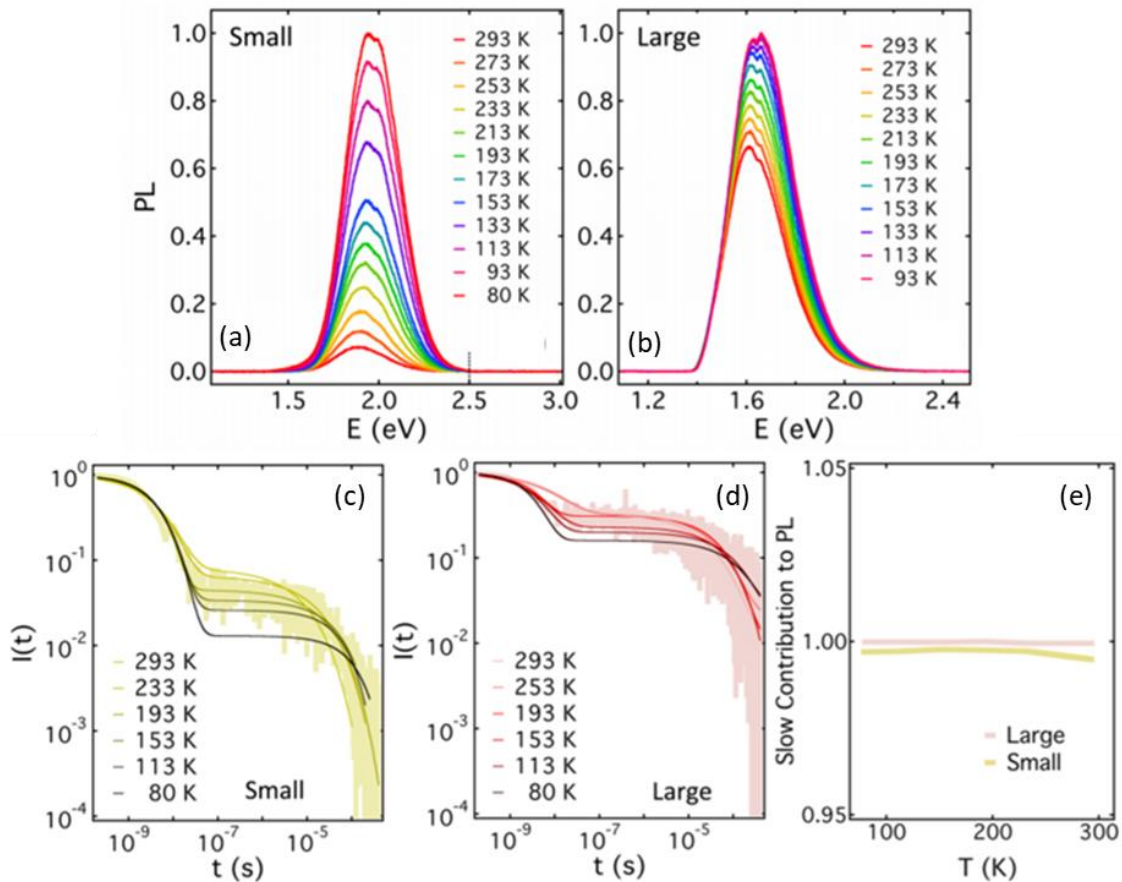


Figure 5.4. The temperature dependent photoluminescence spectra of (a) the small and (b) large silicon nanocrystals with the corresponding temperature dependent photoluminescence decay of (c) the small and (d) large samples. (e) The slow microsecond decay contributes most of the total emission regardless of size or temperature. Reprinted with permission from Ref. [186]. Copyright 2018 American Chemical Society.

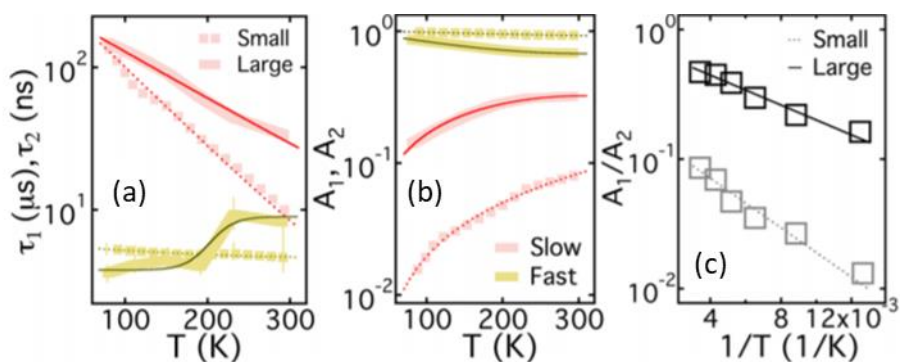


Figure 5.5. (a) Photoluminescence relaxation lifetimes of the small and large samples at $-80\text{ }^{\circ}\text{C}$, (b) the temperature dependent amplitudes of the slow and fast decay and (c) their corresponding ratio. Reprinted with permission from Ref. [186]. Copyright 2018 American Chemical Society.

To this point the data suggest that the relative strength of the fast decay increases exponentially as size and temperature decreases. When calculating the contribution of the fast decay to the overall PL, however, one finds that the fast mode has very little influence on the overall PL ($< 2\%$) even though $A_2 \gg A_1$ in the small sample. Physically, this means that the time scale of the fast decay is too short to make any significant contribution to the overall steady state PL.

To rationalize the data, there are essentially three models that can be used; (1) The fast decay is the result of direct or quasi-direct relaxation, (2) the fast relaxation is purely the result of surface chemistry, or (3) the fast decay is a higher-order result of quantum confinement. The first explanation does not seem plausible as the smallest nanocrystals that were used in this study have a diameter of 3 nm, which is above the expected crossover size for indirect to quasi-direct emission (1-2 nm). Even so, If the sample did crossover to direct-like emission, the expected emission wavelength would be below 400 nm, which would be filtered out of the experimental setup. The second explanation does not seem to capture the full picture either, because, as mentioned earlier, if the fast decay is purely due to surface effects, a $1/R$ trend would be expected for the ratio of the decay amplitudes, A_2/A_1 . **Figure 5.3** shows that this is not the case and that the actual trend is

much stronger. Furthermore, if oxygen related surface defects were the root cause, a strong temperature dependence would be expected for the small nanocrystals when compared to the large nanocrystals because of the thermal activation associated with surface defects. Yet, our results indicate that the relative amplitude of the fast to slow decay has a similar temperature dependence for both the large and the small samples (**Figure 5.5c**).

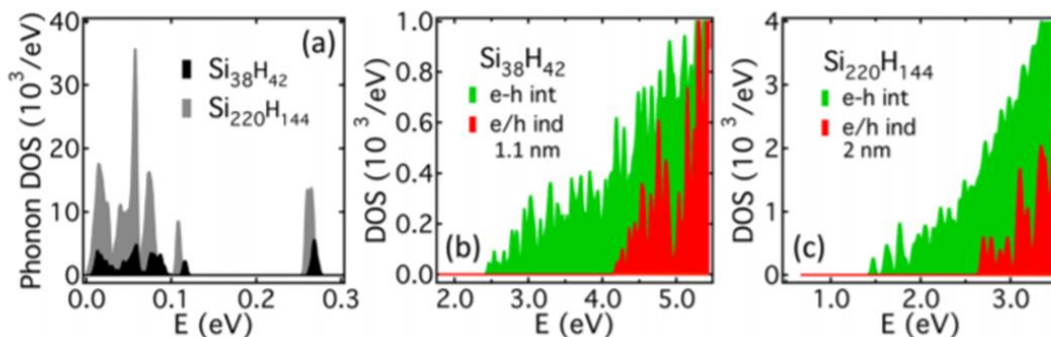


Figure 5.6. (a) DFT derived phonon density of states for two different sized silicon nanocrystals with the corresponding electronic density of states for the (b) small and (c) large silicon nanocrystal. Note: the green and red colored electronic density of states are calculated with and without electron hole interactions, respectively. Reprinted with permission from Ref. [186]. Copyright 2018 American Chemical Society.

The third picture offers one plausible explanation for the observed data. Recent DFT calculations by Hapala *et al.* suggest that minigaps appear within the conduction and valence band of small SiNCs.¹⁸⁷ These minigaps could have a significant impact on the dynamics of hot electrons. Similarly, when calculating the electronic density of states (DOS) of various sized SiNCs, it was observed that the mini gaps in the conduction band are present near the band edge (**Figure 5.6b-c**). The indirect nature of the SiNCs band gap also requires a phonon for recombination and the phonon DOS was determined to have energy comparable to the minigaps in the electronic DOS (**Figure 5.6a**). One can also see from **Figure 5.6a** that the phonon DOS is relatively independent of size. Yet, the size dependence in the electronic DOS could play a significant role in the electron-phonon coupling.

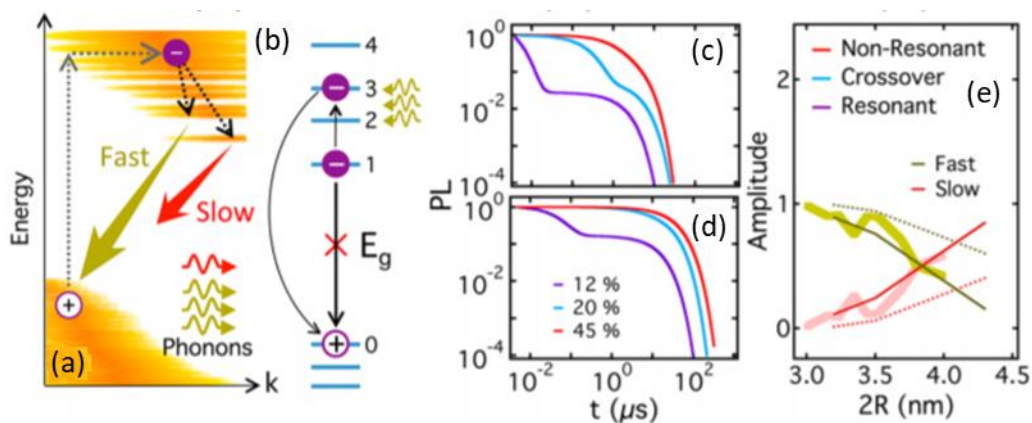


Figure 5.7. (a) Illustration of the proposed mechanism for exciton recombination with a resonant fast (yellow) and a non-resonant slow (red) decay. (b) An energy diagram of the proposed model where direct recombination via Kasha's rule is artificially blocked to mimic the long lifetime associated with the indirect band gap. Modeled photoluminescence relaxation curves at a temperature of (c) $T = 0.025$ eV and (d) $T = 0.010$ eV. Note the key in (d) corresponds to room temperature quantum yield. (e) Measured and calculated photoluminescence relaxation amplitudes of the fast and slow decay as a function of size. The calculated amplitudes are shown at two different temperatures (solid: $T = 0.025$ eV; dashed: $T = 0.010$ eV). Reprinted with permission from Ref. [186]. Copyright 2018 American Chemical Society.

Recent work by Sager *et al.* invoked minigaps in the quantum-confined band structure of SiNCs to explain the presence of a size dependent Fano resonance in micro-Raman spectra.¹¹⁹ Similarly, in this work we suggest that resonance could be the cause for the fast mode of exciton relaxation. Using perturbation theory based DFT, a model was developed to further explore this hypothesis.

In a physical sense, the DFT models attempts to capture the dynamics of hot electrons in SiNCs (**Figure 5.7a**). An electron is excited above the band edge where it quickly thermalizes to either the bottom of the band edge or the top of the minigap. When the electron thermalizes to the bottom of the band edge, the typical slow microsecond phonon assisted decay occurs, yet when the electron relaxes to the top of the minigap, the electron-phonon interaction is impacted by resonance such that the rate of recombination is enhanced.¹⁰⁹ Within this model one would expect to find the fast decay emission slightly blue shifted when compared to the slow microsecond decay

due to its recombination at a slightly higher energy excited states. The work by Klimov and coworkers, in fact, corroborated this idea when measuring spectrally resolved decays in SiNCs.¹²⁵ Furthermore, reasonable agreement is achieved between the DFT model and the experimental data (**Figure 5.7c-e**) giving further credence to this electron phonon coupling picture.

5.3. Conclusion

SiNCs offer a nontoxic alternative to the metal chalcogenide quantum dots. Yet due to the complex nature of electron-hole recombination at the hand of oxygen-sensitive surface states impacting an indirect band gap material, it has been challenging to achieve a detailed understanding of the radiative recombination process. In this work, plasma synthesized SiNCs were separated into monodisperse fractions and the size dependence of the PL kinetics was probed. The fast and slow decay amplitudes showed a strong size dependence, which was inferred to be the result of size dependent electron-phonon coupling. Although the computed phonon DOS was relatively independent of size, the computed electronic DOS showed a strong dependence on size, as would be expected for quantum confinement. Computationally, as the SiNCs size decreases, the DOS becomes more discretized, and ‘minigaps’ in the conduction band start to appear. These minigaps were proposed to have a strong impact on the electron-phonon coupling, which was qualitatively corroborated with perturbation based DFT calculations. These findings could help the design and synthesis of SiNCs to optimize their QY and PL decay dynamics, with the ultimate goal of achieving higher efficiency quantum dot LEDs made from abundant nontoxic materials.

5.4. Experimental Methods

Plasma synthesized SiNCs were hydrothermally passivated with 1-dodecene and then separated by DGU using m-xylene and chloroform to prepare the gradient. A five-step gradient was used with a 50 %, 60 %, 70 %, 80 %, and 90 % mixture of chloroform in xylene that was

progressively layered on top of each other. The centrifuge spin rate and time was 30K RPMs and 14.5 hours, respectively. Detailed instructions on how to separate the fractions are given in **Appendix B5**. The samples were drop cast on a fluorinated self-assembly monolayer (SAM) slide (**Appendix B4**) and then room temperature lifetime and PL measurements were taken using an inverted microscope with a 60X 1.2 NA water-immersion objective. Temperature dependent measurements were taken using an upright microscope in transmission mode using a 4X long-working-distance NA 0.13 objective. For modulated excitation, a fiber coupled UV laser was used (Advanced Laser Diode Systems, PiL037, 375 nm, 30 ps pulse width, 140 m W peak power, 1 kHz modulation) and for steady state excitation a fiber coupled a 365 nm LED was used.

CHAPTER 6. MICROSTRUCTURE AND TEMPERATURE

DEPENDENCE IN SILICON NANOCRYSTAL PHOTOLUMINESCENCE

6.1. Introduction

The microstructure and crystal packing of nanoparticles can affect their observed photophysics, giving scientists another degree of freedom in the tuning and development of nanoparticle devices. Methods to facilitate nanoparticle self-assembly and packing include DNA passivation,¹⁹⁷ slow evaporation,¹⁹⁸ electric field driven assembly¹⁹⁹ and superlattice growth at the air-liquid interface,^{200, 201} among others.¹⁴¹ In turn, due to the proximity of nanoparticles in nanocrystal solids, such super-assemblies can exhibit enhanced carrier mobilities,¹⁴⁰ altered band structure,⁴⁴⁻⁴⁶ and changed and enhanced photonic properties.^{106, 159, 202, 203} In this work, temperature and ligand concentration are used to externally modulate the microstructure and packing of size separated SiNC fractions. Specifically, a size dependent coupling between the PL of SiNCs and temperature is found, while the temperature dependent PL of the smallest fractions reveals an irregular jump discontinuity. The size-temperature coupling offers insight into recombination dynamics in SiNCs while the jump discontinuity, although rationalized with a simple physical explanation, gives insight into both a mechanism for PL enhancement and the dichotomy between surface vs. core emission in SiNCs.

6.2. Results

Non-thermal plasma synthesized SiNCs passivated with 1-dodecene were separated into size dependent fractions using DGU and then drop cast onto fluorinated glass slides to be analyzed (**Figure 6.1**). Temperature dependent PL was measured for several fractions and the corresponding PL intensity as a function of temperature is plotted in **Figure 6.2b**. Note that each fraction's PL is

normalized to its room temperature PL. Two representative samples at different ends of the size window, denoted “small” and “large”, were used to take temperature dependent dynamic PL measurements (**Figure 6.2a**). These time dependent PL decays were fit to a double stretched exponential decay (**Eq. 5.1**) and the corresponding microsecond lifetime is plotted in the inset of **Figure 6.2a** as a function of temperature. Parallel to the temperature dependent PL measurements, micrographs were taken for several fractions at sequentially decreasing 20 K increments. **Figure 6.2c** shows two micrographs of the small SiNC ensemble at 153 K (left) and 133 K (right) where changes to the microstructure are apparent. Crack formation in the SiNC ensembles, as seen in **Figure 6.2c**, would occur in all samples regardless of size at a temperature near 140 K, yet only in the smallest fractions was it reversible. In larger fractions the changed microstructure would persist when temperatures would return to room temperature. This allowed for room temperature atomic force microscopy (AFM) images to be taken on the cracked microstructure of larger samples (**Figure 6.2d**).

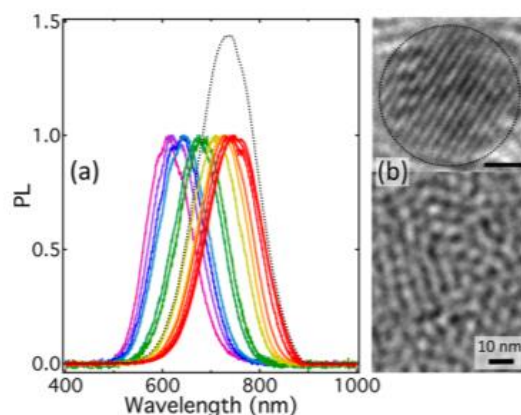


Figure 6.1. (a) The photoluminescence of size separated silicon nanocrystal fractions (solid) and the photoluminescence of the as-produced parent (dashed). (b) Transmission electron micrograph of a single nanocrystal (top; scale bar is 1 nm) and an ensemble of silicon nanocrystals (bottom). Reprinted with permission from Ref. [108] Copyright 2018 American Chemical Society.

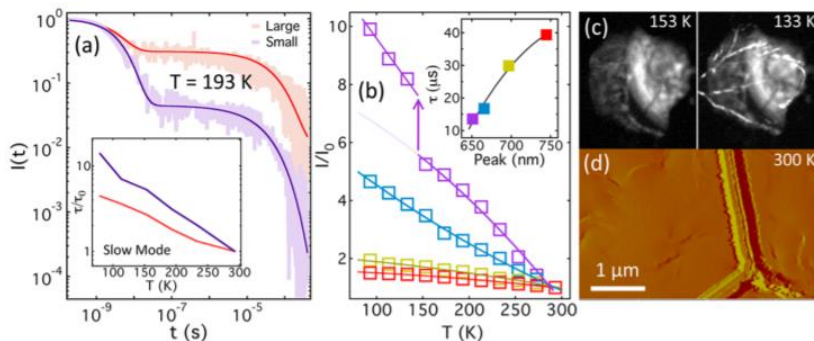


Figure 6.2. (a) The time dependent photoluminescence of a small and large diameter fraction measured at 193 K. The inset shows the photoluminescence lifetime of the “small” and “large” fraction as a function of temperature. (b) The maximum photoluminescence intensity as a function of temperature for several size-separated fractions with the inset showing the corresponding lifetime as a function of peak emission. (c) An optical micrograph showing a (left) drop cast silicon nanocrystal ensemble prior to (right) crack formation. Note the temperature in the top left corner of each micrograph. (d) The cracks that formed in the larger diameter nanocrystal ensembles would persist even when cycled back to room temperature allowing for atomic force microscopy images to be taken. Taken with permission from Ref. [108]. Copyright 2018 American Chemical Society.

6.3. Discussion

From these results, four main observations can be made.

- (1) The lifetime is largely unaffected by the PL jump (inset of **Figure 6.2a**).
- (2) The PL jump occurs only in the smallest fractions (**Figure 6.2b**).
- (3) Morphological cracks form in the SiNC ensembles corresponding to the PL jump (**Figure 6.2c**).
- (4) The SiNC size is indirectly related to its PL-Temperature coupling (**Figure 6.2b**).

To rationalize the first three observations, a simple physical model is proposed: the jump discontinuity in PL is the result of excess ligand in the SiNC ensemble. Although, it is tempting to propose a model invoking the recombination dynamics of SiNCs, the first observation (1) limits this as a plausible explanation. The lifetime of the microsecond decay in a SiNC ensemble can be directly related to its QY.¹²⁷ If a new radiative channel was opened due to either a morphological

feature or by a temperature dependence, one would expect to see a similar enhancement in the overall lifetime. But, as **Figure 6.2a** shows, this is not the case.

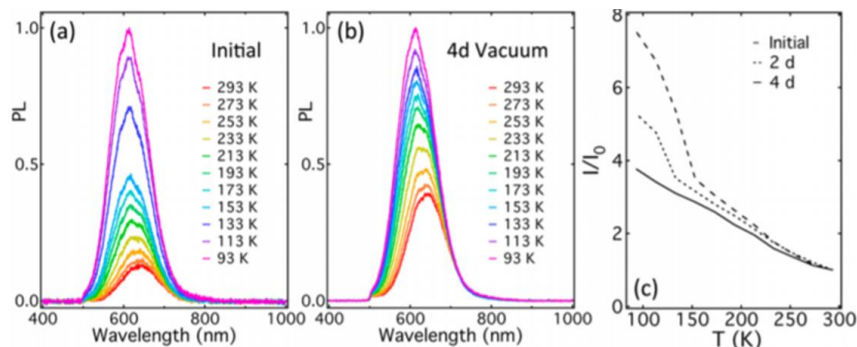


Figure 6.3. (a) The temperature dependent photoluminescence of the “small” sample showing the photoluminescence jump. (b) and (c) Successive sessions of vacuum annealing were able to effectively remove the photoluminescence jump. Reprinted with permission from Ref. [108]. Copyright 2018 American Chemical Society.

In observation (2) we see that the PL jump only occurs in the smallest SiNC ensembles. When SiNCs are separated through DGU, any excess ligand that was in the parent sample would remain near the top of the centrifuge tube due to its low molecular weight. This excess ligand would then be collected with the smallest SiNC fractions, increasing the relative concentration of free ligand in these fractions. This explains the different morphological features observed in the small and large SiNCs. The excess ligand in the smallest fractions acts as a plasticizer, allowing the ensemble structure to restore after deformation. This is not the case though in the larger fractions. The larger fraction ensembles, without the excess ligand, deform irreversibly.¹⁰⁸

Observation (3) states that cracks form in the SiNC ensembles at temperatures corresponding to the PL jump. Now if the proposed model is correct one would expect that these cracks are directly responsible for the increase the PL in the SiNC ensembles. To rationalize this observation with the proposed model we introduce three new experiments. In the first experiment a small SiNC fraction which exhibits the PL jump is exposed to various durations of reduced

pressure (**Figure 6.3a**). After each exposure, the PL jump and overall PL enhancement weakens (**Figure 6.3b-c**). In the second experiment we demonstrate that upon the addition of excess ligand to drop cast parent samples, the PL jump and overall enhancement to the PL returns with the PL jump corresponding to a phase change in the ligand (**Figure 6.4**). It is also observed that as the excess ligand freezes, the effective area of excitation increases (**Figure 6.4d**). Now the final test measures the extinction spectra of pure 1-dodecene and decane, where the extinction greatly increases when each respective ligand changes to the solid phase (**Figure 6.5a-c**).

From these three experiments we find that the PL jump can be added or subtracted with the addition or removal of excess ligand, respectively, and that a phase change increases the extinction of pure ligand. The smoking gun used to corroborate the proposed model is the fact that upon freezing, the area of PL extends past the original beam area (**Figure 6.4d**). The micrographs in **Figure 6.4d** show that once the SiNC/ligand matrix freezes nanocrystals outside of the original beam path become excited, due to the scattered light throughout the matrix. This is indicative of what happens in the small fractions. The cracks that form in the smaller SiNC ensembles scatter high energy blue light in accord with Rayleigh's ω^4 law, which effectively excites nanocrystals outside of the original beam path and effectively increase the excitation pathlength, thus enhancing PL. It is interesting to note that although emission in SiNCs can be highly dependent upon the surface states,^{30, 111, 114} here very little affect to the overall QY in the frozen and perturbed morphologies is observed. One would expect that the surface state would be affected by the changing morphologies induced upon freezing. This seems to indicate that the overall emission is predominantly core related as was discussed earlier.^{109, 110}

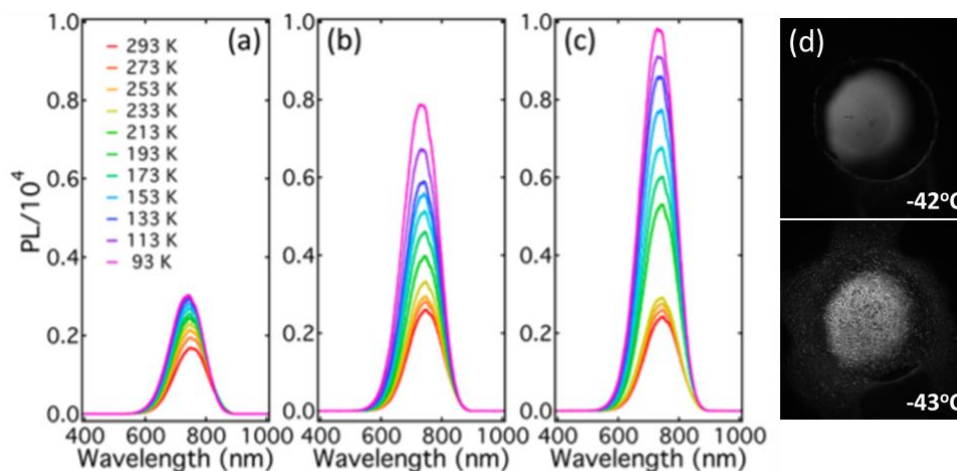


Figure 6.4. The temperature dependent photoluminescence of a (a) pure, as-produced sample and the sample in (b) excess 1-dodecane and in (c) excess decane. Note that the photoluminescence for (a), (b) and (c) are all normalized to the max photoluminescence in (c). (d) Optical micrographs of the photoluminescence in an as-produced silicon nanocrystal/decane matrix immediately before (top) and after (bottom) freezing. Reprinted with permission from Ref. [108]. Copyright 2018 American Chemical Society.

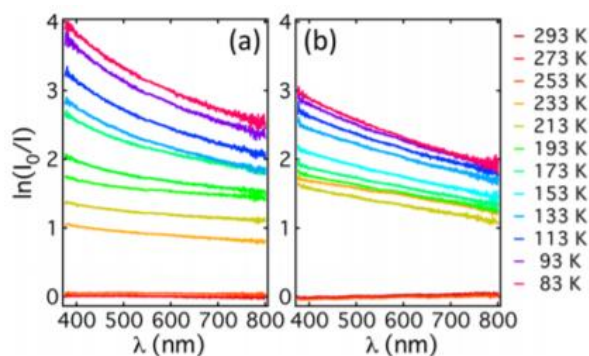


Figure 6.5. Temperature dependent extinction spectra of pure (a) 1-dodecene and (b) decane. Reprinted with permission from Ref. [108]. Copyright 2018 American Chemical Society.

To understand the final observation (4), a computational model is used to calculate the temperature dependent PL of three different sized (29, 66, and 220 atoms) SiNC models (**Figure 6.6**). More details on the computational model can be found in **Section 6.5** and in Ref. [108]. **Figure 6.6b** shows that the PL of each model exhibits the typical size dependent emission due to the quantum confinement effect, and at lower temperatures the modeled PL is enhanced and blue

shifted, matching experimental data.^{108, 127} In a fluorescent system, the most efficient radiative channel is through the highest occupied molecular orbital (HOMO) and lowest unoccupied molecular orbital (LUMO) in accordance with Kasha's rule.²⁰⁴ When looking at the electronic structure of the modeled SiNCs we see that the Kohn-Sham (KS) energy levels are relatively dense and as such any thermal fluctuations can cause for crossover in the energy levels.¹⁰⁸ Energy level crossover will effectively decrease the PL because recombination would then occur through orbitals other than the HOMO and LUMO, in violation of Kasha's rule. This explains the overall decrease in PL with increasing temperature, yet to understand why the smaller diameter SiNCs have a greater dependence on the temperature, the atomic fluctuations in each model is shown.

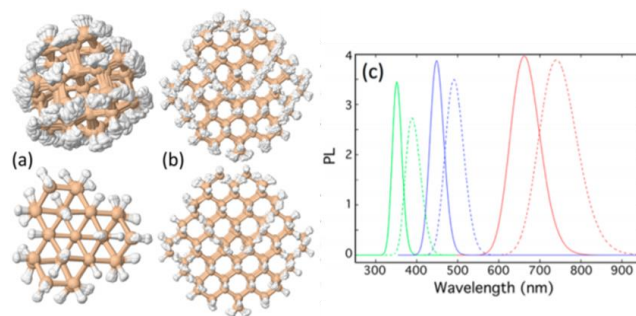


Figure 6.6. Thermal fluctuations in a “small” and (b) “large” SiNC modeled at 300 K (top) and 77 K (bottom), where the surface atoms experience a greater degree of fluctuations. Note that to view the thermal fluctuations, snapshots from a molecular dynamics simulation were superimposed. Here we only show two models for simplicity, yet three different sized models were used. (c) The photoluminescence of these three different sized silicon nanocrystals are determined using computational methods where the green, blue and red PL curves correspond to the small, medium, and large sized silicon nanocrystal models while the dashed and solid curves correspond to photoluminescence calculated at 300 K and 77 K, respectively. In accordance with experimental results, the photoluminescence red shifted with increasing size and the photoluminescence intensity decreases with increasing temperature. Note that the small, medium, and large silicon nanocrystal consisted of 29, 66, and 220 silicon atoms, respectively. Reprinted with permission from Ref. [108]. Copyright 2018 American Chemical Society.

When examining the thermal fluctuations in the models, one sees that the Si atoms with the lowest coordination (i.e. fewest bonds to other Si atoms) experience the greatest oscillations. In this case, the Si atoms at the surface and their corresponding hydrogen passivation will

experience the greatest fluctuations (**Figure 6.6a – b**). Now because smaller SiNCs have a greater surface area to volume ratio than their larger nanocrystal counterparts, temperature variations will have a stronger impact on their KS orbitals and thus the NC PL.

6.4. Conclusion

The challenges involved in SiNCs photophysics are complex and many, due in part to an intricate balance between exciton-phonon coupling in core recombination and the various emissive surface states.^{29, 30, 110, 111, 114, 115, 186} In this chapter, the PL of size separated SiNCs was examined as a function of the microstructure which was indirectly modulated with temperature and excess ligand. From this work four main observations are made; **(1)** the QY was unaffected by the PL jump, **(2)** a PL jump occurs at approximately 140 K only in the smallest fractions, **(3)** morphological cracks formed in the SiNC ensembles corresponding to the PL jump, and **(4)** the SiNC size is directly related to its QY and temperature coupling. The first three observations were explained with a simple physical model: free ligand in the SiNC ensembles would freeze and due to the turbidity of the nanocrystal/ligand matrix, enhance the extinction coefficient through scattering, effectively increasing the excitation pathlength. This was then confirmed by demonstrating an enhancement or detracting of low-temperature PL in SiNC ensembles by increasing or decreasing excess ligand, respectively. Using a computational model, the final observation was rationalized. This model indicated that thermal effects were greatest in smaller SiNCs due to a greater surface area to volume ratio. These thermal effects caused rearrangement in the KS orbitals limiting exciton recombination *via* Kasha's rule, thus lowering the overall QY. These results provide insight into SiNCs exciton recombination dynamics while gaining an understanding on the role that close packed behavior has on SiNC photophysics. These insights can be used to help tune and optimize the optical properties in SiNCs. In the chapter to follow, the

close pack nature of SiNCs will be considered with a greater emphasis on the size dependent packing structure.

6.5. Experimental Methods

SiNCs were synthesized through a non-thermal plasma synthesis and passivated with 1-dodecene according to established methods.^{103, 131} The nanoparticles were then separated into fractions *via* DGU using a two solvent mixture of m-xylene and chloroform also in accordance with established methods (**Appendix B5**).^{107, 127, 194} SAM slides were made by annealing glass cover slips in an atmosphere of perfluorodecyltriethoxysilane (**Appendix B4**). The lifetime and PL measurements were done according to **Appendix B2** and **Appendix B1**, respectively. Details for the computational model are explained elsewhere.¹⁰⁸ Briefly though, DFT within the Vienna ab initio Simulation Package (VASP) was used for geometry optimization, ground-state electronic structure, and adiabatic MD ab initio calculations. Perdew-Burke-Ernzerhof (PBE) functionals with a plane wave basis set and projector augmented wave (PAW) potentials with a periodic boundary condition were used for all electronic structure optimization. While emission spectra was calculated *via* first-principle MD sampling and time integration of the nanocrystal.²⁰⁵

CHAPTER 7. NANOPARTICLE SUPERLATTICE: PRELIMINARY

RESULTS

7.1. Introduction

Ordered nanoparticle arrays or superlattices have been an exciting topic of research both theoretically and experimentally since the early developments in nanoparticle synthesis. Fortunately, two years after the seminal paper on monodisperse nanoparticle synthesis,⁵ superlattice was achieved, proving it was not just possible experimentally but somewhat ubiquitous.²⁰⁶ The capabilities and methods of nanoparticle self-assembly have since developed with most methods using a variation on drop casting of sessile droplets,¹⁹⁸ slow evaporation procedures,²⁰⁷ or Langmuir-Blodgett (LB) techniques.^{201, 208} Yet, some more advanced methods have also been demonstrated such as the use of electric fields to drive nanoparticle self-assembly^{199, 209, 210} as well as using DNA-passivated nanoparticles to control specific nanoparticle-nanoparticle interactions and assembly.^{197, 211} Entropic effects play a key role in nanoparticle self-assembly but temperature has been shown to be a useful variable for varying the respective contribution of the internal energy and entropy to the total free energy.²⁰⁷

Many times, when nanoparticles are drop cast or formed within solution, especially in the presence of small amounts of anti-solvent, the resulting superlattices can be a 3D crystal.²¹² Yet, using an LB trough or evaporating over a polar droplet effectively eliminates this third degree of freedom, resulting in 2D superlattice films.^{201, 213} The use of diethylene glycol (DEG) instead of water as the liquid sub-phase has been shown to be particularly useful in the development of superlattice monolayers as most LB films cast on DEG exhibit less cracking.^{208, 214} The exact reasoning for this is unknown, yet the chemical inertness and low evaporation rate of DEG

have been offered as plausible explanations.²⁰¹ This methodology has recently been expanded on through the development of binary and tertiary monolayer nanocrystal films.^{201, 215} Furthermore, the Murray, Kagan, and Sargent groups, among others, have applied these monolayers films in devices such as LEDs, transistors, and photovoltaic cells.²¹⁶⁻²¹⁸

In ordered nanocrystal arrays, the optical properties of the QD solid can be greatly affected in a non-linear fashion. Plasmonic nanoparticles, such as silver and gold nanocrystals, have been shown to exhibit a strong coupling to the local order.^{159, 203, 219, 220} Furthermore, it has been shown that the band structure of quantum dot superlattices can form mini bands, which could be a particularly useful in boosting the efficiency of quantum dot solar cells.^{44, 221, 222} Nevertheless, the assembly of nanoparticles into ordered arrays gives researchers another tool to control and tune the photophysics of nanoparticles and nanoparticle devices.

Now, with the exception of a few reports, SiNC superlattices has not been demonstrated in the literature and the reasons for the limited availability of such observations is unknown.^{151, 223, 224} In this chapter we examine the ability of both SiNCs and AgNPs to form superlattices. In doing this we, get a direct comparison of the self-assembly of metallic nanoparticles compared to that of semiconducting nanoparticles, namely SiNCs. Here, this is done as a function of nanoparticle size and ligand length to gain insight into the mechanism of nanoparticle self-assembly. The preliminary results of this study show that although SiNC superlattices can form, the process appears to be highly size dependent and it is harder to coax SiNCs into ordered arrays in comparison to the plasmonic metal nanoparticle counterparts. Furthermore, we find indications that the initial concentration of nanoparticle sessile drops plays a key role in self-assembly, which could rationalize some of the challenges faced for SiNC in the past.

7.2. Materials and Methods

In this work, we use established methods for the synthesis of both SiNCs and AgNPs, using two different synthetic methods for the synthesis of AgNP. For the first AgNP synthesis method, **Method I**, oleylamine is used to dissolve silver acetate. This silver acetate and oleylamine solution is then injected into refluxing toluene where it is left to reflux for ~8 hours.²²⁵ This results in polydisperse samples that are later separated into distinct size fractions using DGU. In the second procedure, **Method II**, silver nitrate is dissolved in dichlorobenzene with the aid of oleylamine. This solution is then injected into a refluxing solution of dichlorobenzene and dodecanediol and allowed to react for three minutes before the solution is cooled to room temperature.¹⁵⁸ This procedure results in monodisperse samples of AgNPs. To synthesize the SiNCs, we use a top down approach. Briefly HSQ is annealed in a tube furnace at approximately 1200 °C resulting in SiNCs of approximately 5.5 nm in diameter encased in a silicon dioxide shell.¹³⁶ This SiNC/Silicon dioxide composite is then ball milled to reduce the composite granule sizes to approximately 200 nm and then the dioxide layer is removed by etching in equal parts concentrated hydrofluoric acid, water, and ethanol.¹⁰⁴ Note: this method effectively removes the silicon dioxide layer in approximately 1-2 hours, but in general the final product is polydisperse.¹⁰⁴ To obtain monodisperse fractions, etching procedures done in the dark can be employed to limit the etching rate of pure silicon and thus preserve the native size of the SiNCs after annealing.¹³⁶ After etching, the hydrogen passivated SiNCs are dispersed in a 5:1 ratio of mesitylene and the passivating ligand (i.e. 1-dodecene, 1-pentecene, 1-octadecene, or 1-eicosene). This is then refluxed at ~180 °C for ~8 hours. The resulting clear reaction mixture is then washed three times using toluene and ethanol as the solvent and anti-solvent, respectively.

To separate the nanoparticles into size-resolved fractions, DGU was employed using a five-layer step gradient with chloroform in m-xylene at concentrations of 50 %, 60 %, 70 %, 80 %, and 90 % at volumes of 1.5 mL each. The as-produced parent samples are then layered on top of the gradient at a volume of 300 μ L. The spin rates were held constant at 30,000 RPMs while the duration of each spin was varied. To separate the nanoparticles into distinct fractions, a micrometer is used to control the depth of a Teflon tube within the centrifuge tube. The Teflon tube is coupled to an empty vial which is coupled to a syringe. Using the syringe to build a vacuum inside the empty vial draws the topmost layer from the gradient into the vial. In this work, starting from the top of the test tube, each subsequent layer was progressively drawn off at an increment of 2 mm (e.g. fraction 5 corresponds to a depth of 8 – 10 mm in the centrifuge tube).

As was mentioned in the introduction of this chapter, there are several established methods to develop nanoparticle superlattices. Here we employ two methods, simple drop casting and drop casting on DEG liquid sub-phase. In the first method, a nanoparticle solution is simply drop cast onto a substrate. In a perfect system the solvent evaporation would be slow enough to limit any kinetic traps that could occur during self-assembly. Practically, this can be achieved in a crude manner by placing a vial cap on top of the drying sessile drop. As the solvent evaporates, it becomes trapped inside of the vial cap, saturating the local atmosphere with solvent vapor. Aside from the dispersity²²⁶ and strong dipole interactions,²²⁷⁻²³¹ the entropy of the systems plays a key role in the self-assembly of nanoparticles.^{141, 232-234} For purely hard sphere particle-particle interactions, temperature has a limited influence because entropic contributions dominate the free energy ($\Delta F = \Delta U - T\Delta S$), but when there are significant interparticle interactions beyond hard-sphere, temperature becomes a useful variable for controlling self assembly. Yet, unfortunately, the temperature is also coupled to the evaporation rate of the solvent, which can lead to kinetic

traps. In an attempt to decouple the dependence of the evaporation rate with temperature, a home-built chamber was designed (**Figure 7.1a**). This device consists of two separate chambers, a solvent chamber and a sample chamber, connected by a small hole. One chamber is for the nanoparticle sessile drops and the second is for pure solvent that serves as a vapor reservoir. The temperature of the solvent chamber can be controlled externally and is independent of the temperature of the first chamber. This allows for one to effectively control the rate of evaporation independent of the substrate temperature. It is important to note that in these systems, the substrate is also vital for nanoparticle assembly through sessile drop drying dynamics, as the smoothness and wettability of the solvent and substrate play a key role on the final drop cast film morphology.²³⁵

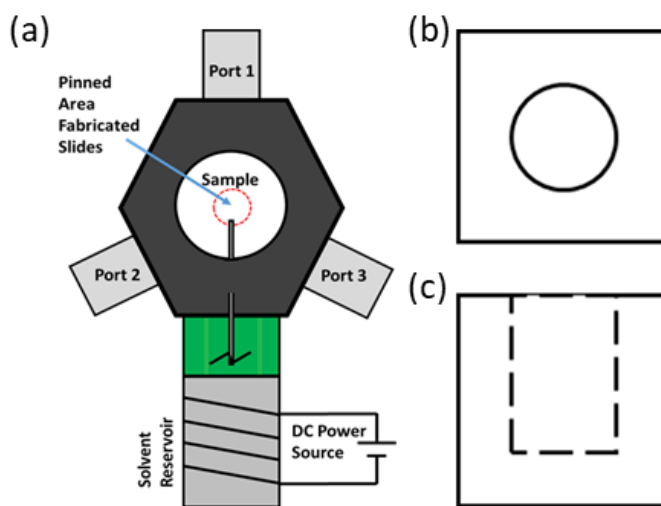


Figure 7.1. To develop nanocrystalline superlattice, two experimental setups were designed. (a) The first experimental setup is used to control the temperature and evaporation rate of sessile drops. Two chambers with independent heating sources are connected by a small hole. The first chamber holds solvent while the second chamber houses the sessile drop. Varied substrates can be used while the temperature of the substrate can be controlled to within a tenth of a degree. The temperature control on the second chamber or solvent reservoir can be used to push solvent vapor through the small hole connecting the two chambers, thereby controlling the evaporation rate of the sessile drop. The second experimental set up is a Langmuir Blodgett trough. (b) The diameter of the trough is 1/2" or 3/8" while (c) the trough depth is approximately 1/4"

The second method used to create nanoparticle superlattices is a Langmuir-Blodgett (LB) trough and here, we use a very simple LB design. A trough is drilled into pure Teflon with a diameter of 3/8" or 1/2" with a depth of approximately 1/4". Nanoparticles suspended in toluene are then drop cast onto a DEG liquid sub-phase and allowed to dry for at least fifteen minutes. The nanoparticle superlattice structure is then captured using the Langmuir-Schaefer technique, rinsing the substrate in deionized water, and then drying under reduced pressure.^{236, 237}

To characterize the drop cast films, optical micrographs were collected in transmission, reflection, and under cross polarizers, while in the case of the AgNPs, the plasmon absorption peak was also analyzed. Modulating the initial contact angle of the sessile drop was used as another variable during sessile drop drying. To achieve variation in the contact angle, two different substrates were used, a fluoropolymer coated glass slide and a pure glass slide. To prepare the fluoropolymer glass slides, a cleaned glass slide is annealed in an atmosphere of perfluorodecyltriethoxysilane for at least 8 hours. Further analyses for these larger scale structures are still under development and will be reported at a later time.

7.3. Preliminary Results: Silver Nanoparticles

AgNPs prepared by **Method I** were separated based on size using DGU, and as has been observed by other groups, the plasmon peak is inversely related to the diameter of the nanoparticle (**Figure 7.2**).^{158, 159, 238, 239} To test the propensity for self-assembly in these monodisperse samples, we simply drop cast them onto TEM grids, and as can be seen in **Figure 7.2c-d**, they readily form superlattice, albeit with limited range. Turning our attention to AgNPs made by **Method II**, we were able to produce monodisperse silver nanoparticles without the need for post processing which formed 3D superlattice crystals when simply drop cast onto a TEM grid (**Figure 7.2e-f**). Due to the higher concentration of monodisperse nanoparticles we could examine the effects that ligand

concentration, evaporation rate, sessile drop contact angle, and substrate temperature have on nanoparticle sessile drop drying. (Note: as with most nanoparticle syntheses based on the hot injection method, after the initial reaction, excess ligand is washed away using solvent, anti-solvent combinations. The number of washing cycles performed has been shown to directly control the concentration of excess free ligand and ligand surface coverage in each sample.^{240, 241} Here, we use this to control the amount excess free ligand in each sample). To control the temperature and evaporation rate, the device in **Figure 7.1a** was used, while the substrate was varied from a clean glass slide to a SAM-coated glass slide.

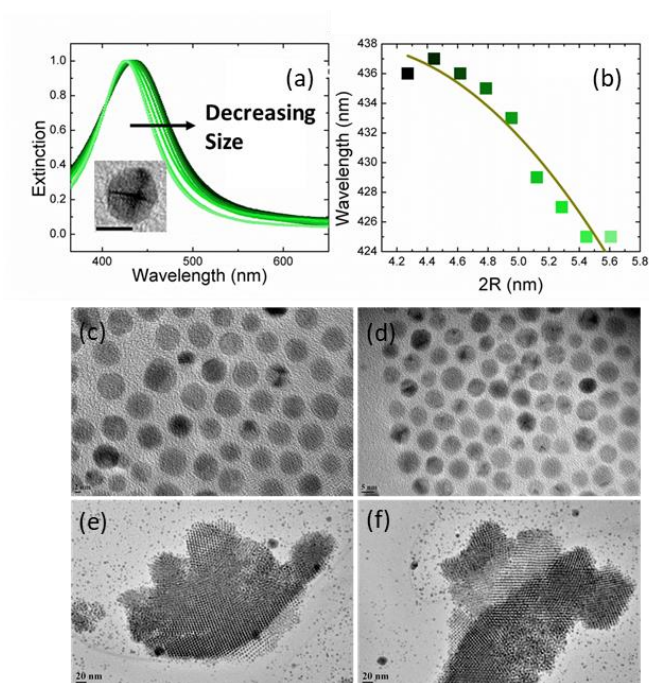


Figure 7.2. (a) The plasmon peak of nanocrystalline silver nanoparticles exhibits a size dependent red shift (b) such that the as the size of the nanoparticle decreases the plasmon peak wavelength increases. (c) - (f) By simply drop casting silver nanoparticle solution on a TEM grid, 3D superlattice structures can form. Note: (c) and (d) were prepared from samples synthesized via Method I, while (e) and (f) were prepared from nanocrystals synthesized via Method II.

Nanoparticle sessile drop drying is an active area of research.^{235, 242-246} In the most contemporary models, the pinning and depinning nature of the sessile drop can be derived from the Young-Dupree equation,²³⁵

$$0 = \gamma_{SL} - \gamma_{SG} + \gamma_{LG} \cos \theta_o. \quad (7.1.)$$

Here, γ_{SG} , γ_{LG} , and γ_{SL} are the surface tension between the solid-gas interface, liquid-gas interface, and solid-liquid interface, respectively, while θ_o is the initial contact angle of the droplet. As the sessile drop begins to evaporate, the contact angle will slightly decrease ($\theta_o - \delta\theta$). This will induce a slight horizontal force toward the center of the droplet as discussed by Orejon *et al.*²³⁵

$$\delta F = \gamma_{LG} \cos(\theta_o - \delta\theta) - \gamma_{LG} \cos \theta_o \approx \gamma_{LG} \sin \theta_o \delta\theta. \quad (7.2.)$$

Previous reports have indicated that depinning of the droplet can occur when an intrinsic energy barrier, U , is overcome, where this barrier is dependent upon substrate smoothness and chemical homogeneity.^{244, 247} Therefore, $\frac{\partial U}{\partial r}$ is a force opposing depinning while δF is a force trying to depin the droplet. As such, if δF is equal to $\frac{\partial U}{\partial r}$, then the droplet would remain static, but with any increase to δF , one would expect to see the contact line of the droplet depin;

$$\frac{\partial U}{\partial r} = \delta \vec{F} = \gamma_{LG} \sin \theta_o \delta\theta. \quad (7.3.)$$

In **Figure 7.3** we used the dual chamber set-up (**Figure 7.1a**) to vary only two parameters, the temperature of the substrate and the amount of solvent vapor, for the parent AgNP solution. The substrate (SAM or pure glass slide), solvent (toluene), solvent vapor (toluene), nanoparticle concentration (~ 3 mg), and sessile drop volume ($\sim 6 \mu\text{L}$) were held constant for each sample. As can be seen in **Figure 7.3**, at higher substrate temperatures and lower ambient solvent vapors, the nanofluid drops dry in constant contact area mode²⁴⁸ leaving a coffee ring of nanoparticles on the edges. However, at lower substrate temperatures and higher solvent vapor pressures, the AgNP

suspensions can depin and dry in constant contact angle mode. Now, this type of depinning only occurred with the fluorinated SAM (and “slippery PDMS”)²⁴⁶ coated substrates, as the initial contact angle is much greater in comparison to the contact angle of pure glass. Regardless of substrate temperature or ambient solvent vapor, nanoparticle suspensions were not observed to depin on pure glass substrates. (Note: In initial experimentation, when using a substrate coated with “slippery PDMS”,²⁴⁶ nanoparticles suspended in m-xylene would dry in constant contact angle mode regardless of substrate temperature and ambient solvent vapor. This could provide a perfect experimental set-up to examine the effect that temperature and evaporation rate have on superlattice formation while limiting the dependence on such factors as nanoparticle concentration and drop morphology.)

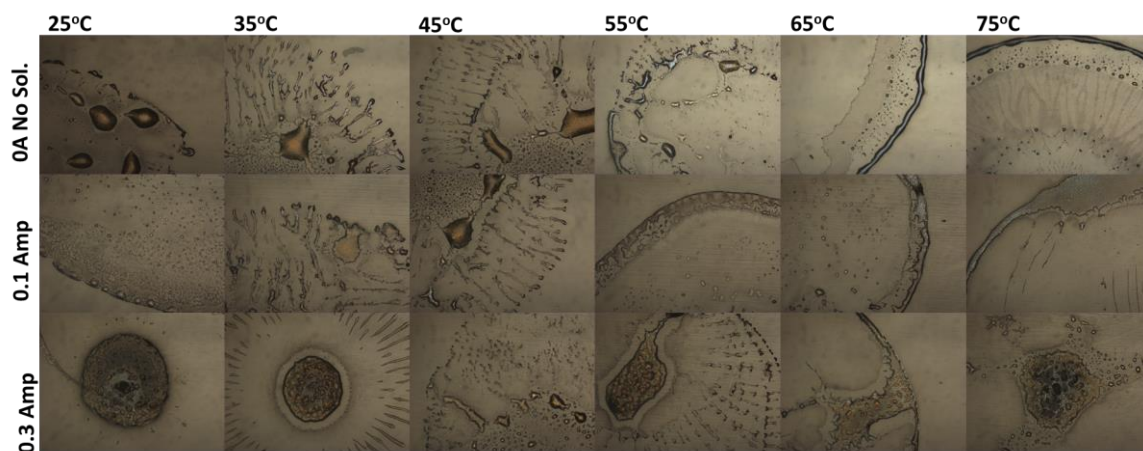


Figure 7.3. Simultaneous control of both substrate temperature and solvent vapor is an effective way to influence sessile drop drying. For low solvent vapor and high substrate temperature, the nanoparticle solutions dry in constant contact area mode, while at high solvent vapor and low temperature, the nanoparticle sessile drop can dry in constant contact angle mode. Note in these samples the substrate is a fluorinated SAM on a glass slide and the solvent and solvent vapor are toluene.

When drop casting AgNP suspension with excess ligand at room temperature, large superlattice crystals were observed (**Figure 7.4**). (Note that to create an environment of excess

ligand the nanocrystals were only washed once.²⁴⁰) What's interesting to see here is that it appears that excess ligand aides the nanoparticle superlattice formation. For instance, the droplet in **Figure 7.4** is only a small satellite droplet resulting from the sessile drop drying. Because this sample was dried on glass, it dried in constant contact area mode, leaving the edges pinned. Most of the material from this drop remained on the edge in a coffee ring pattern, but small droplets of excess ligand and AgNPs were dispersed throughout the inside of the drop. Now one possibility is that the excess ligand is acting as a depletant in this scenario.²⁴⁹⁻²⁵¹ Giving further credence to this possibility is the observation that when heating these samples, the crystalline shapes melt away, but as the sample returns to room temperature, the shapes do not reform. As toluene is no longer present in the sample, the system would only consist of two components (excess ligand and nanocrystals), and depletion interactions mediated by the common solvent would no longer be present.

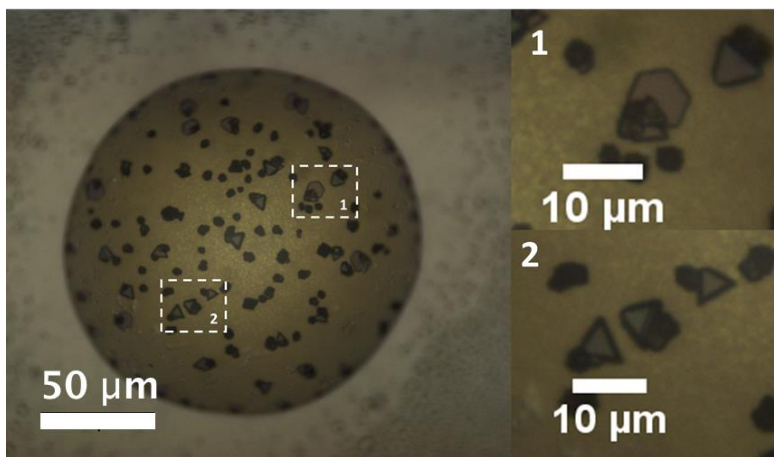


Figure 7.4. Drop casting silver nanoparticle suspensions in toluene on pure glass substrates at room temperature results in sessile drops drying in constant contact area mode. Within the coffee ring, droplets of excess ligand and silver nanoparticles can form. Inside of these droplets, silver nanocrystal superlattices can form.

In one last study, we drop cast monodisperse AgNP solutions synthesized by **Method II** with the following conditions held constant: substrate (fluoropolymer glass slide), solvent (m-

xylene), solvent vapor (m-xylene), nanoparticle concentration (~3 mg), sessile drop volume (~ 6 μL), and ambient solvent vapor (high), while only the substrate temperature was changed. At lower temperatures, the sessile drop dries in constant contact angle mode, depositing the material in the center. Now as the temperature of the substrate is increased the sessile droplet can no longer dry in a purely constant contact angle mode as some material is deposited in small fingers. Interestingly, when examining the plasmon peak of each drop cast film we find that a second peak begins to emerge that is directly coupled to the substrate temperature. This second peak is red shifted and considerably narrower than the original peak. Presumably this second peak is due to the intrinsic microstructural arrangement of the nanocrystals. In the report by Wei *et al.*, for example, nanocrystalline superlattices exhibited a red shift in the plasmon peak when compared to the plasmon peak of the solution state sample, similar to what is observed here.¹⁵⁹ Wei *et al.* did not observe the narrowing of the plasmonic peak, however, but the computational work by George Schatz entitled “Silver Nanoparticle Array Structures that Produce Remarkably Narrow Plasmon Lineshapes,” suggests that this narrowing could be due to microstructure changes of the nanocrystals or even superlattice formation.²⁵² It is also interesting to note the color change in the AgNP films. As the substrate temperature was increased for each sample, the color observed in reflection changes from a green to red (Note that the spectra and images were taken at room temperature and the increasing temperature refers to the substrate temperature at the time the sample was drop cast).

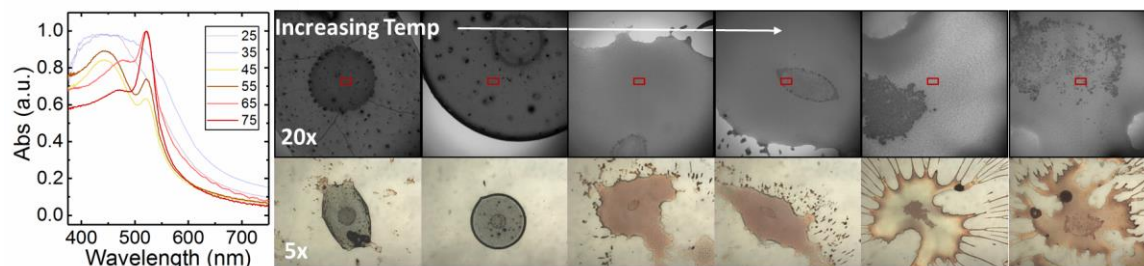


Figure 7.5. Drop casting the same parent silver nanoparticle solution from xylene onto substrates of progressively increasing temperatures (i.e. the initial temperature was 25 °C and each progressive sample was increased by 10 °C) in a high xylene vapor pressure atmosphere resulted in various morphologies and spectroscopic absorption peaks. As the temperature of the substrate was increased for each individual sample, the resulting sample’s plasmonic spectra would exhibit a second peak (Note that the plasmonic spectra was measured after the sample had returned to room temperature).

7.4. Preliminary Results: Silicon Nanocrystals

With the insight gained from considering the self-assembly of AgNPs, we now turn our attention to SiNCs. Only one group has reported on the experimental observations of SiNC superlattice.^{151, 223, 224} Yet, the ubiquity of reports on superlattice in metal and metal chalcogenide nanoparticles, as well as the complexity of these superlattice,¹⁴¹ hint that there is an intrinsic difference in the nanoparticle self-assembly of SiNCs compared to other metal chalcogenide quantum dots.

From previous experience with plasma synthesized SiNCs ($d \sim 3.5$ nm), little to no superlattice has been observed. This is in stark difference when compared to the previous case of AgNPs, where simply drop casting the nanoparticle solutions leads to quality superlattice. So, in this project, we use a larger size of SiNCs ($d \sim 5.5$ nm), which is more comparable in size to the AgNP suspensions, while also modulating the ligand length to determine its effect. Typically, SiNCs are synthesized with a ligand length of twelve carbon atoms where most metal and metal chalcogenide nanoparticles use a ligand with eighteen carbon atoms. We explore this parameter

space by passivating SiNCs with ligands of 12, 15, 18, and 20 carbon atoms. Furthermore, along with drop casting, we explore the previously described LB technique to develop nanoparticle superlattice.

Using a top down approach to synthesize SiNCs, we created as-produced samples that we passivated with ligands of varied length and that emit in the red to NIR region of the spectrum. These as-produced samples are then separated into distinct fractions based on size using DGU as described earlier. **Figure 7.7** shows the PL peak of each sample as a function of fraction number. (Note that C12, C15, C18, and C20 indicate the number of carbon atoms in the ligand while the letter afterward indicates the DGU spin, referring to **Table 7.1**.) Each sample was separated using a rotor speed of 30,000 RPMs, yet various spin durations were used to change the concentration and size resolution of each fraction.

Table 7.1. Duration and Rotor Speed for Each Nanoparticle Separation

Spin	Rotor Speed (RPMs)	Duration (hours)
A	30,000	2
B	30,000	2
C	30,000	5
D	30,000	5
E	30,000	5
F	30,000	1
G	30,000	5

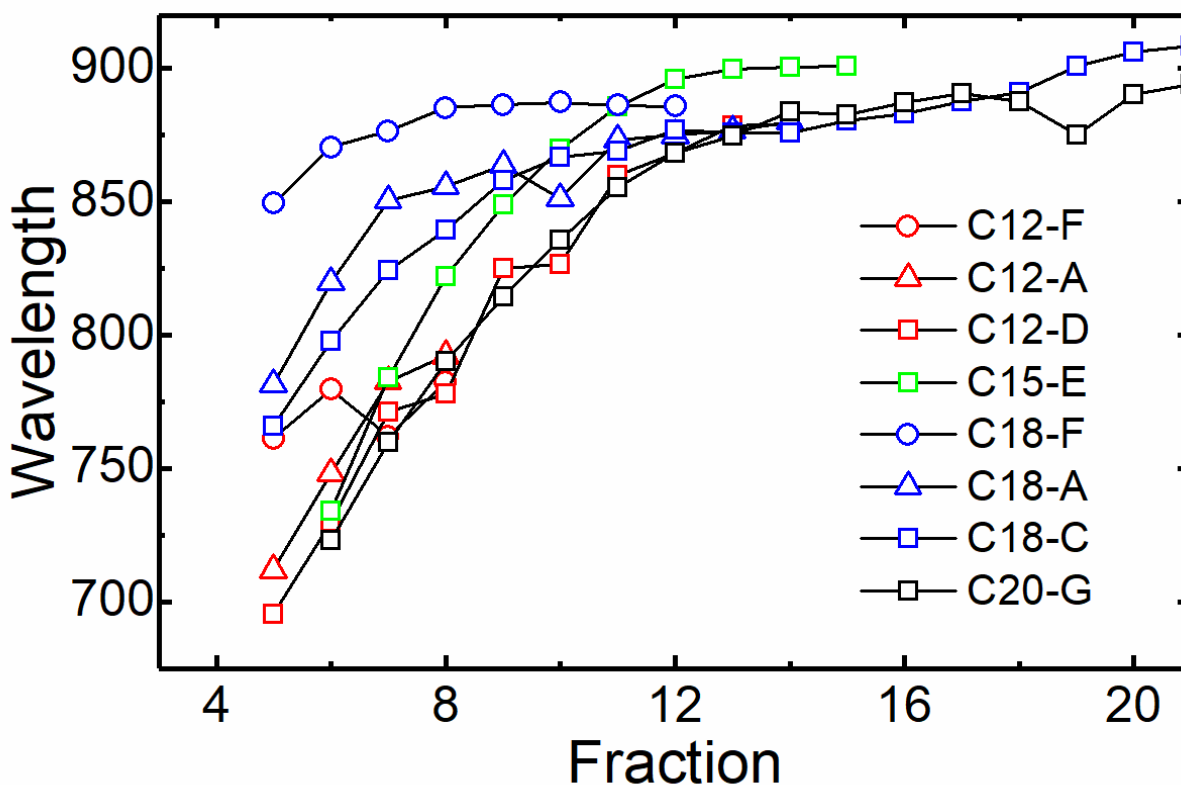


Figure 7.6. As-produced samples of silicon nanocrystals were passivated with different lengths of carbon chains ranging from 12 carbon atoms to 20 carbon atoms. These different samples were then separated into distinct fractions using density gradient ultracentrifugation. The peak of the resulting photoluminescence from these samples is then plotted here where one can see that the peak emission increases with increasing fraction number. The duration of these spins was varied from 1 to 2 to 5 hours and the final letter in the key corresponds to the spin in **Table 7.1**.

As can be seen in **Figure 7.6** the PL peak increases for progressively larger fraction numbers consistent with the anticipated effects of quantum confinement and previous reports.¹⁰⁶⁻

¹¹⁰ We use the Langmuir-Blodgett trough with a DEG liquid sub-phase as described in the previous section to develop nanocrystalline superlattice. This method exhibited remarkable success in creating two-dimensional SiNC superlattice as can be seen in **Figures 7.7-7.13**.

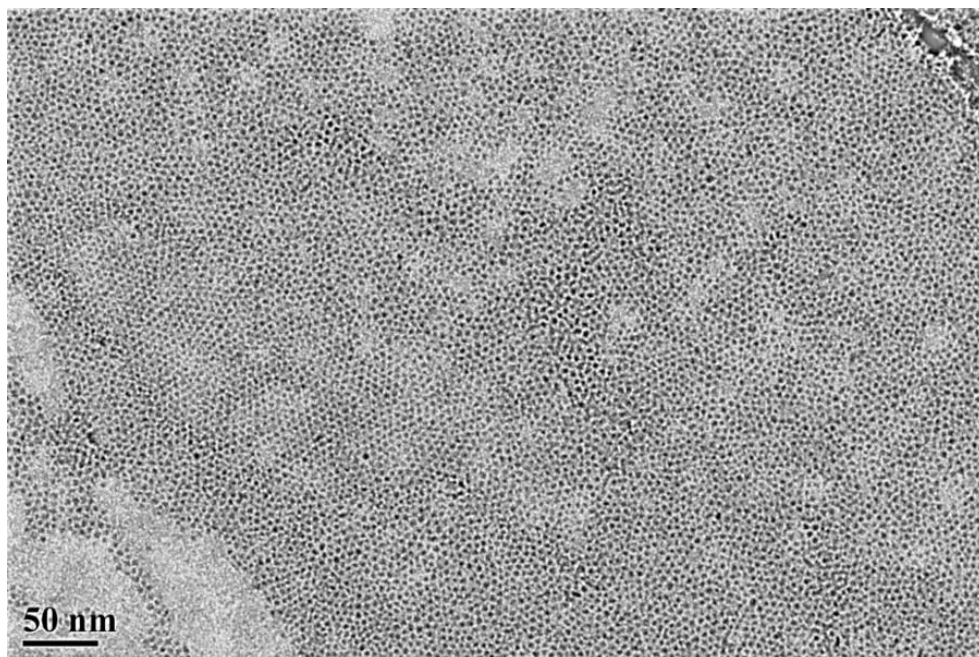


Figure 7.7. Silicon nanocrystals with a ligand length of twelve carbon atoms (Spin D from **Table 7.1** and Fraction 7).

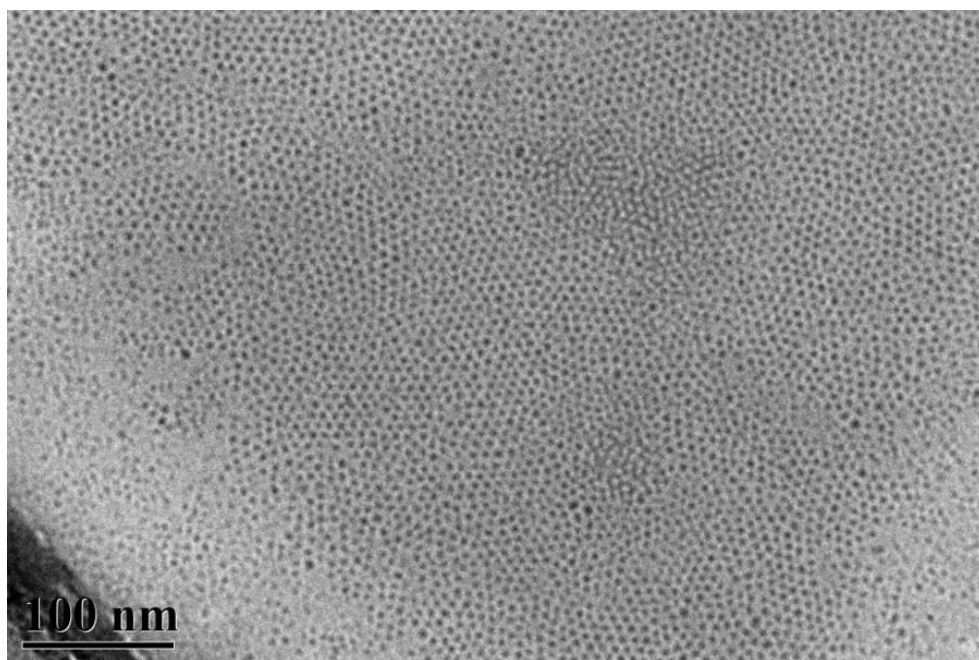


Figure 7.8. Silicon nanocrystals with a ligand length of fifteen carbon atoms (Spin B from **Table 7.1** Fraction 7 Image 1).

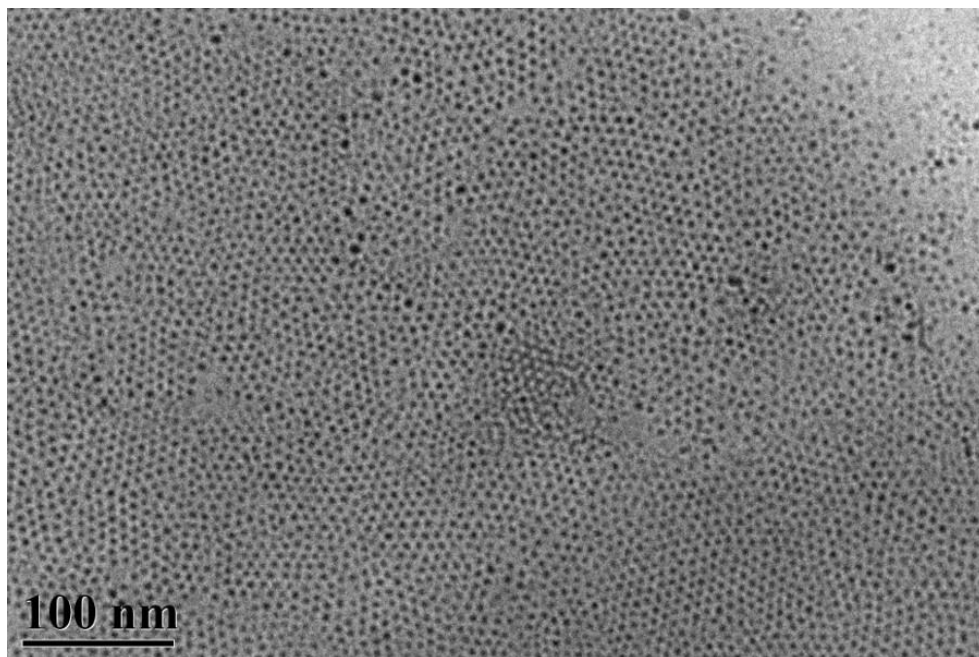


Figure 7.9. Silicon nanocrystals with a ligand length of fifteen carbon atoms (Spin B from **Table 7.1** Fraction 7 Image 2).

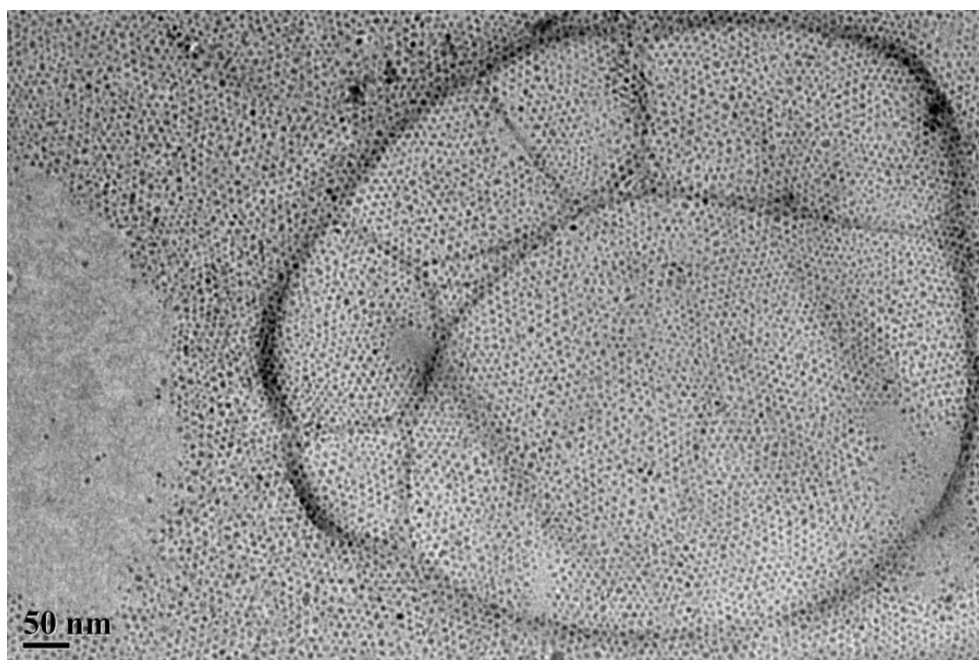


Figure 7.10. Silicon nanocrystals with a ligand length of eighteen carbon atoms (Spin F from **Table 7.1** Fraction 9 Image 1).

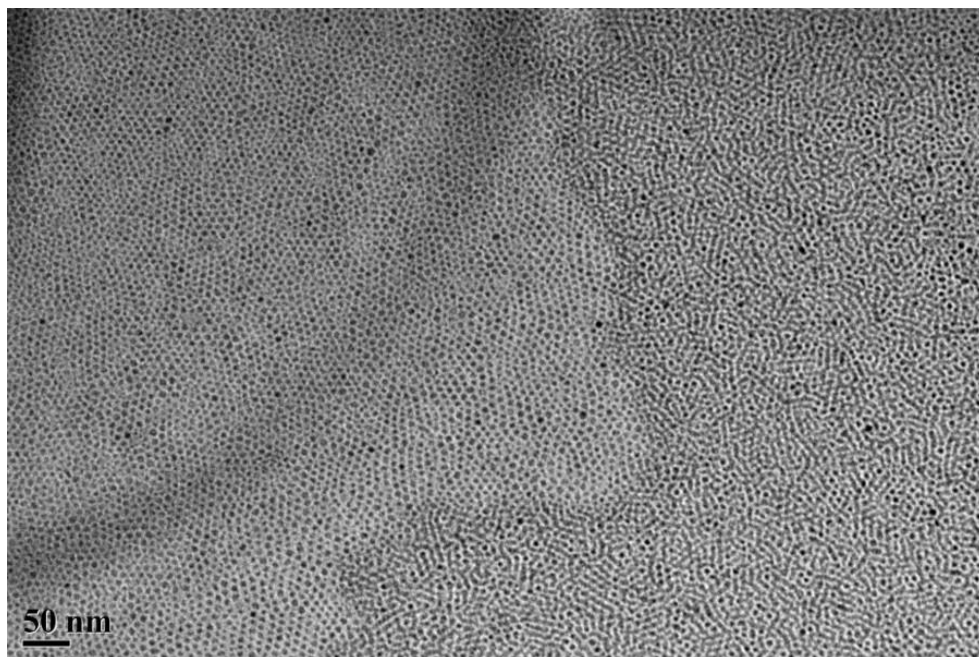


Figure 7.11. Silicon nanocrystals with a ligand length of eighteen carbon atoms (Spin F from **Table 7.1** Fraction 9 Image 2).

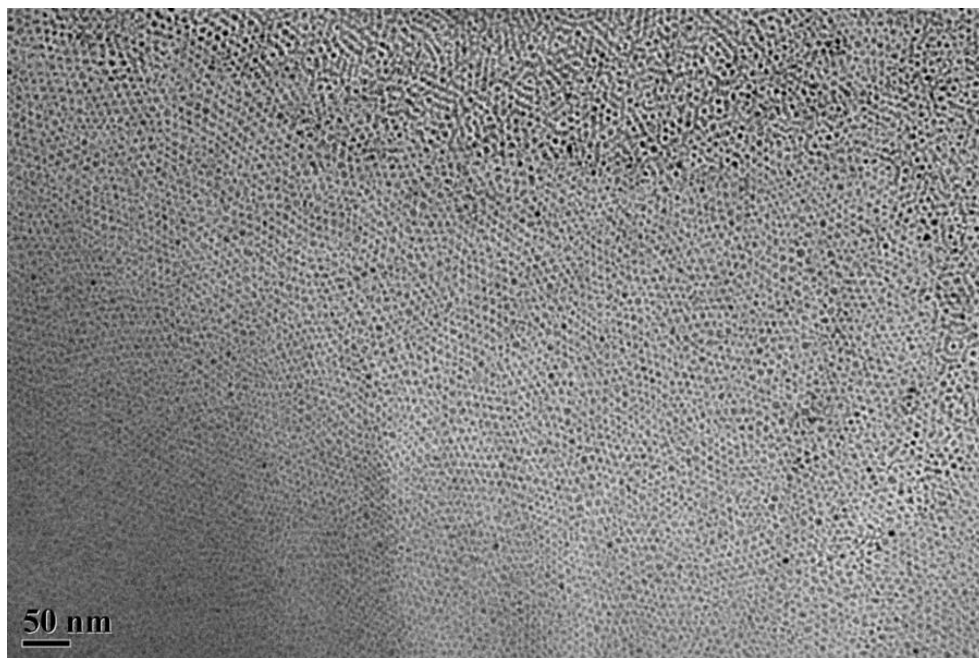


Figure 7.12. Silicon nanocrystals with a ligand length of eighteen carbon atoms (Spin F from **Table 7.1** Fraction 9 Image 3)

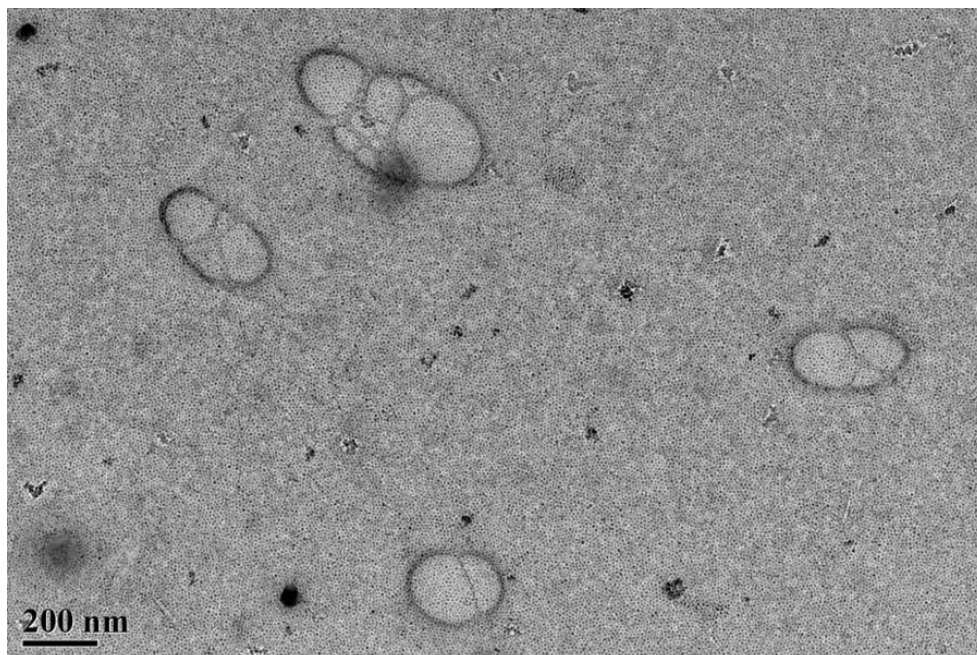


Figure 7.13. Silicon nanocrystals with a ligand length of eighteen carbon atoms (Spin F from **Table 7.1** Fraction 9 Image 4)

Ideally, for lower concentrated samples the smaller diameter LB trough ($d \sim 3/8''$) would be used to increase the coverage of nanoparticles, as the surface area of the smaller trough is roughly half of the larger. By using the same parent sample for each spin of similar ligand length, a convenient way to roughly vary the concentration is by the spin duration. In **Figure 7.14** we show representative TEM images from fractions of the same parent material originating from roughly the same depth of the centrifuge tube but with different spin durations. As can be seen, the fraction with the shortest spin duration has the greatest degree of coverage on the TEM grid. Though it should be noted that although this sample has a higher concentration the film was also prepared in the larger LB trough ($d = 1/2''$), while the fractions with lower concentrations were prepared in the smaller LB trough ($d = 3/8''$). A potential consequence of the size disparity between the two troughs is that the DEG in the smaller LB trough would have a more pronounced meniscus. As was shown by Guerra *et al.*, superlattice films that form on curved droplets will create a soccer

ball like pattern of nanoparticles and voids due to the strain induced by the curvature of the droplet surface.²⁵³ A similar phenomenon could be happening here, although the length scales might suggest otherwise. Another more practical explanation would be that the greater curvature in the smaller diameter trough could be causing the nanoparticles to flow to the edge of the trough, further decreasing the already low concentration of nanoparticles.

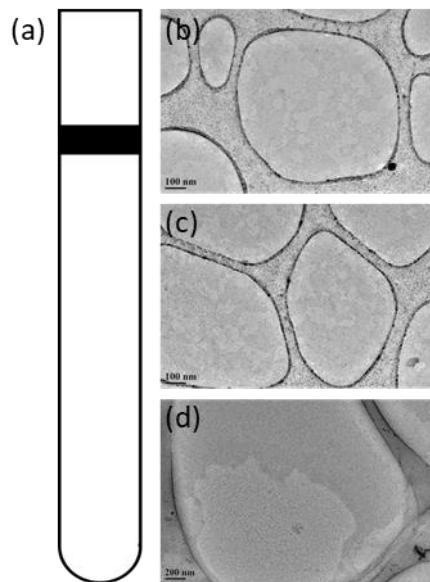


Figure 7.14. A representative image for fractions of the same parent taken at approximately the same centrifuge tube depth (a) but with a different spin duration of (b) 5 hours, (c) 2 hours, and (d) 1 hour.

To quantitatively understand the superlattice structure as a function of nanocrystal size, we analyze the TEM images of each fraction by first determining the particle centers using ImageJ. These particle centers can then be used to determine several characteristic features of the lattice such as the pair correlation function, structure factor, m_6 , n_6 , among others. This analysis is still running and there is not enough statistical data to report any conclusions at this time.

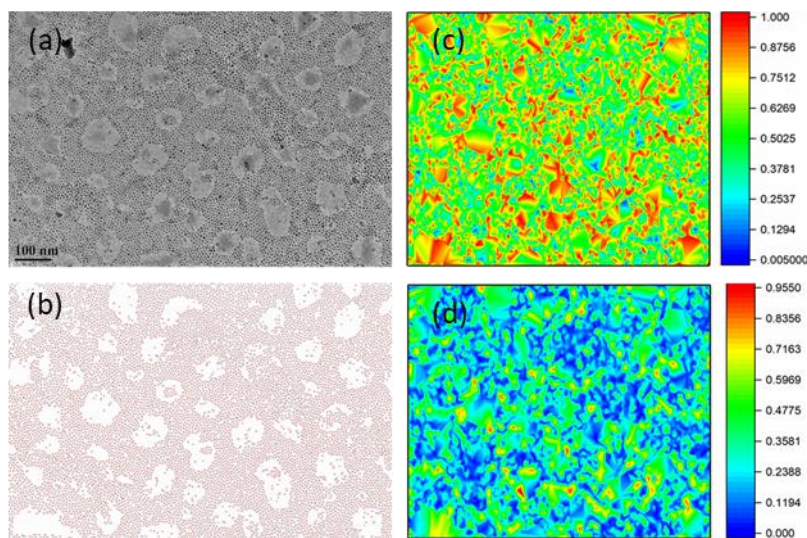


Figure 7.15. Once the particle centers are determined, various structural quantities can be computed. Here we show an example of a (a) TEM image with the (b) particle outlines selected using ImageJ. Various order parameters such as (c) m_6 and (d) n_6 can then be determined for each particle and mapped back onto the original image.

A promising approach to better understand how the diameter and ligand length might affect the propensity to form superlattice is *via* an optical signature, such as a shift in PL or domain birefringence. With the formation of minibands due to superlattice structure, one might also expect to see a corresponding change in the PL.^{44, 45} In addition, as is the case with polymers,^{254, 255} one might expect to see birefringence in the optical micrographs of SiNC superlattices. As can be seen in **Figure 7.17**, this is indeed the case. We see these birefringent structure form regardless of nanoparticle size, ligand length, and synthetic method. Yet, the concentration and degree of polydispersity appear to be important. At the time of this writing, fractions of low concentration do not form birefringent structures; only the monodisperse fractions of sufficiently high concentration will create the birefringent structures (i.e. the parent samples do not). Further evidence of microscale crystallinity, such as SEM or AFM images showing nanocrystalline terraces, will be important to further explain the self-assembly of SiNCs. But for now, we will rely

on the circumstantial evidence of birefringence and the requirement of high initial concentration as proof of packing and crystallinity.

If, indeed, the concentration and size resolution of SiNC samples plays a key role in self-assembly, it would help explain part of the disparity seen between SiNCs and other nanoparticles. In general, there is only one method that can be used to create monodisperse SiNCs without post processing.¹³⁶ Incidentally, this is the same method used by the only group that has produced SiNC superlattice. All other SiNC synthetic methods would either be A) to polydisperse to form superlattice outright or B) too dilute after size selective post processing methods. For metal and metal chalcogenide nanoparticles, there exist synthetic methods that are capable of achieving concentrated, high quantity, high size resolution samples outright,^{2, 256, 257} or one can use digestive ripening techniques to increase the size uniformity of the sample after synthesis.²⁵⁸⁻²⁶⁰

Nanoparticle concentration in the initial suspension is likely a key variable in the formation of superlattice. The fact that simply drop-casting AgNPs on a TEM grid leads to 3D superlattice crystals, however, indicates that there is still probably a significant intrinsic difference between the mechanism of SiNC superlattice formation and that for other metallic nanoparticles. Typically, at least based on our own experience, simply drop casting SiNC solutions leads to disordered or amorphous samples, and there are a number of possible reasons this could be the case. For instance, nanoparticle-ligand interactions are much different in SiNCs, where the ligand on SiNCs is irreversibly attached *via* a covalent bond. In contrast, the ligands on metallic nanoparticles experience a weaker covalent bond and undergo dynamic motion and exchange. Ligand-nanoparticle interactions could aid in self-assembly, for example, by giving the nanoparticle more freedom to pack. As the nanocrystal lattice is beginning to form, the ligands could conceivably move on the surface of the nanoparticle and even move between nanoparticles, helping the system

form more energetically favorable structures. Another possibility is that the directional nature of the diamond lattice in silicon, or possibly surface charges, could give the nanoparticle a dipole moment. One could imagine that such a hypothetical dipole moment could facilitate the formation of string-like structures during self-assembly and hence spherulitic domains, both of which we have observed for SiNCs.

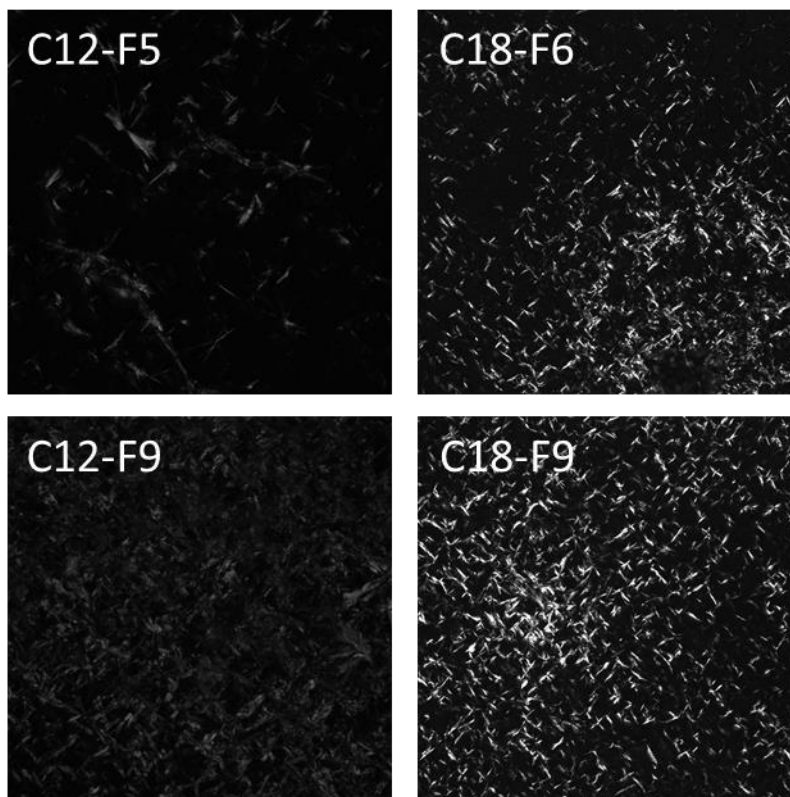


Figure 7.16. Drop cast films of silicon nanocrystals with a sufficiently high concentration of material exhibit birefringent domains.

7.5. Discussion and Future Outlook

Nanoparticle superlattice formation is a very active field of research that has many potential applications. In this work, we used both AgNPs and SiNCs as a case study for superlattice formation and found that both nanoparticles can indeed form superlattice. Simply by drop casting monodisperse fractions of AgNP on a TEM grid, we were able to demonstrate superlattice

formation (**Figure 7.2**). Furthermore, by drop casting a AgNP solution with excess free ligand on a glass slide, large faceted domains of AgNP superlattice would form (**Figure 7.4**). In the case of SiNCs, we were also able to make superlattices, but in doing so we used a more advanced LB technique. The superlattices can form regardless of nanocrystal size and ligand length. For both materials, TEM images showing superlattice can be useful for getting information on the packing structure. But for evaluating long-range order and the propensity to order in general, a better method for quantitatively screening and analyzing samples could lie in the ability to find a coarse optical signature of SiNC superlattice formation. Luckily in both cases – AgNPs and SiNCs – a spectroscopic signature appears to be present; the birefringence in SiNCs (a spectroscopic change may also be associated with this microstructure, but further analysis is needed to confirm this) and the narrowing and red-shifting of the plasmon peak in AgNPs.

There are three potential future directions that this research might take. First, we need to gain a more quantitative understanding of the formation of superlattice in SiNCs. A qualitative picture is beginning to emerge, but more statistics are necessary in order to say anything definitive. Secondly, a more quantitative approach is needed to model superlattice formation from SiNCs and AgNPs on the microscale. Expanding upon the current understanding of the microscopic signatures, as well as using the temperature dependent sample stage from **Figure 7.1a** to vary the temperature, should give greater insight into superlattice formation for SiNCs and AgNPs. Furthermore, using a carefully chosen substrate and solvent, such as a slippery PDMS slide and m-xylene, one might remove a degree of freedom the droplet drying scenario as this particular substrate and solvent combination appear to dry in constant contact angle mode, regardless of temperature. The third direction this project could go is returning to using the LB trough, but introducing temperature as a variable. Simply replacing the bottom of the Teflon trough with a

metal bolt and placing this set up on a hotplate would allow for efficient heat transfer from the hot plate to the DEG sub-phase and then consequently to the nanoparticles. This could potentially give additional insight into the temperature dependent superlattice formation dynamics.

Looking out longer term, assuming “superlattice on demand” can eventually be realized for SiNCs, the next logical step would be to design and develop quantum-dot devices built from SiNC superlattices, such as quantum dot solar cells.²⁶¹ Every hour the earth gets enough energy from the sun to power its daily applications for an entire year.³⁵ With such a large amount of energy, one just needs an efficient method to capture and collect this energy. Quantum dot solar cells not only have the ability to double the theoretical limit of traditional silicon based solar cells to efficiencies of 66 % due to MEG, but they can potentially also be manufactured with considerably lower costs due to their colloidal stability and fluid processibility.^{39, 40, 42, 43} The non-toxic nature and ubiquity of silicon leads to a perfect material to be used in these applications. We hope that the photophysical models and superlattices studies within this report can be used to advance the field of quantum dot solar cells.

CHAPTER 8. SUPPLEMENTAL PROJECT: A COMPUTATIONAL STUDY ON THE FLUORESCENCE OF SILVER NANOCCLUSERS

8.1. Introduction

Silver nanoclusters (AgNCs) are the ‘Goldilocks’ of fluorophores with just the right size, toxicity and photostability.⁷² Organic dyes or metal-chalcogenide quantum dots are typically used in biological applications requiring fluorophores. In these applications quantum dots offer superior photostability compared to organic dyes, yet consist primarily of toxic materials such as lead and cadmium.²⁶²⁻²⁶⁶ Aside from the toxicities, quantum dots are typically large and cumbersome for transport through biological membranes.^{57, 72, 185} However, AgNCs have a core diameter of 1 nm or less allowing them to be readily transported throughout the body, and the relatively benign nature of silver addresses potential concerns about nanotoxicity.^{86-88, 90, 92, 95, 267-269}

These highly efficient fluorophores (QY greater than 90 % in some cases) are typically synthesized using DNA to limit large nanoparticle growth and maintain stability.^{74, 75, 77, 82, 270, 271} Due to the biocompatibility of these particles, Yu *et al.* leveraged the fluorescence of AgNCs to take fluorescent *in vitro* cell images.²⁷² Alternatively, Yeh and coworkers created AgNC sensors, using the sensitivity of their optical properties.⁷⁹ The sensitivity of the AgNC’s optical properties to the surrounding environment has been well established.^{79, 270, 273, 274} For example, Diez *et al.* showed that systematic decreases in the solvating water to methanol ratio of polymer stabilized AgNCs results in a red shift to the PL peak.²⁷³ Additionally, combinatorial chemistry methods have demonstrated that changing the passivating DNA’s sequence can result in PL spanning the entire visible spectrum.²⁷⁰ The Gwinn group used random DNA oligomers to synthesize more than 600 different samples of AgNC.⁸² A corresponding histogram was then developed for peak

emission finding that most DNA AgNC complexes fluoresced with a peak emission at either 540 nm or 630 nm, which were deemed magic colors, corresponding to magic number structures.⁸²In mass spectroscopy studies, several groups found that fluorescent AgNC are highly charged (>4+).^{74, 76, 77, 81} The high charge has been hypothesized to be due to Ag⁺ atoms surrounding a neutral Ag⁽⁰⁾ core^{77, 81} much like that of superatom complexes.²⁷⁵

Here we attempt to glean further insight into the nature of the high charged AgNC and how this charge affects the overall PL *via* computational methods. This chapter outlines the methodology development needed to determine spin resolved PL as a result of the open shell nature of the valent d- and s- orbitals in silver atoms. In more practical terms, we analyze the electronic structure of a AgNC with different charges and ground state (GS) spin configurations. Our goal is to identify promising models with a high potential for fluorescence as a function of charge. The singlet 5+ model is identified as a promising candidate and the spin resolved PL is calculated for mechanistic insight.

8.2. Methods

All electronic structure calculations were performed in a self-consistent manner using DFT²⁷⁶ with spin resolved components and constraints²⁷⁷ as

$$\left(-\frac{\hbar^2}{2m}\nabla^2 + v_\sigma[\vec{r}, \rho_\alpha(\vec{r}), \rho_\beta(\vec{r})]\right)\varphi_{i,\sigma}^{KS}(\vec{r}) = \varepsilon_{i,\sigma}\varphi_{i,\sigma}^{KS}(\vec{r}), \sigma = \alpha, \beta \quad (8.1.)$$

where \hbar is Planck's constant, m is the mass of the electron, $\varphi_{i,\sigma}^{KS}(\vec{r})$ is the i -th Kohn-Sham (KS) orbital, $\varepsilon_{i,\sigma}$ is the energy of the i -th KS orbital and $\sigma = \alpha$ or β electrons. Note: spin resolved calculations are important in this application of DFT due to the open shell nature of the d- and s-valent orbitals in silver atoms forming a nanocluster. Included in the total energy, E^{tot} , is the exchange correlation-functional of electron density. $v_\sigma = \frac{\delta}{\delta\rho_\sigma}(E^{tot} - T^{kin})$ is the potential as a

functional of the spin resolved electron densities, $\rho_\alpha(\vec{r}) = \sum_{i=1}^{N_\alpha} |\varphi_{i,\alpha}^{KS}|^2$ and $\rho_\beta(\vec{r}) = \sum_{i=1}^{N_\beta} |\varphi_{i,\beta}^{KS}|^2$, where N_α and N_β are the number of alpha and beta electrons, respectively. The DFT calculated electronic structure is parameterized by the total charge

$$N = N_\alpha + N_\beta \quad (8.2.)$$

and spin polarization^{278,279}

$$\Delta N_{\uparrow\downarrow} = N_\alpha - N_\beta \quad (8.3.)$$

The value of the spin polarization parameter can be used to identify spin multiplicity as follows: $2S + 1$, where $S = \Delta N_{\uparrow\downarrow}/2$. Thus, a progression of $\Delta N_{\uparrow\downarrow} = 0, 1, 2, 3, \dots$ corresponds to singlet, doublet, triplet, quartet, ... multiplicities, respectively. The spin resolved band gap for each pair of parameters, N and $\Delta N_{\uparrow\downarrow}$, is analyzed as follows

$$\Delta \varepsilon_\sigma^{gap}(N, \Delta N_{\uparrow\downarrow}) = \varepsilon_\sigma^{LU}(N, \Delta N_{\uparrow\downarrow}) - \varepsilon_\sigma^{HO}(N, \Delta N_{\uparrow\downarrow}) \quad (8.4.)$$

as well as the change in total energy

$$\Delta N_{\uparrow\downarrow} = N_\alpha - N_\beta \quad (8.5.)$$

where in all calculations, the passivating ligands' electrons are included in the total number of electrons, N .

A Slater determinant is constructed from the KS orbitals and used to find the transition dipole expectation values, $\langle \vec{D}_{ij,\sigma} \rangle = e \int \varphi_{i\sigma}^* \vec{r} \varphi_{j\sigma} d\vec{r}$, in the independent orbitals approximation (IOA);²⁸⁰ where e is the charge of an electron and \vec{r} is the position operator. Note that the singly-excited state formation is often described as a superposition of the occupied and unoccupied molecular orbital pairs. For example, in solutions of the Bethe-Salpeter equation, $\sum_{i'j'} H_{ij i'j'} A_{i'j'}^\alpha = E^\alpha A_{ij}$, with the many-electron Hamiltonian $H_{ij i'j'} = (\varepsilon_i - \varepsilon_j) \delta_{ii'} \delta_{jj'} + W_{ii'jj'}$ in basis of single electron orbitals $|i\rangle$ and $|j\rangle$ including coulombic interactions, $W_{ii'jj'}$.

The eigenstate solutions read $|\alpha\rangle = \sum_{ij} A_{ij}^\alpha |i\rangle|j\rangle$, and obey normalization $\sum_{ij} |A_{ij}^\alpha|^2 = 1$. The description of dynamics requires a recalculation of such excited states at each time along trajectory $|\alpha(t)\rangle$, $A_{ij}^\alpha(t)$. As an approximation, the superposition of states is represented by one leading term only as $A_{ij}^\alpha(t) \approx \delta_{i,i'(\alpha)} \cdot \delta_{j,j(\alpha)'} + o$, where the excited state, α , is approximated as a pair of orbitals, occupied $i'(\alpha)$ to unoccupied $j'(\alpha)$, with both depending on α , which is referred to as the IOA.²⁸⁰

The transition dipole expectation values can then be used to find the oscillator strength of an electronic transition from KS orbital i to KS orbital j , with given spin σ , such that

$$f_{ij,\sigma} = |\vec{D}_{ij,\sigma}|^2 \frac{4\pi m_e v_{ij,\sigma}}{3\hbar e^2} \quad (8.6.)$$

where m_e is the mass of an electron. Using the oscillator strengths and assuming a lack of spin-orbit coupling, the absorption spectra can then be determined from **Eqs. 8.7-8.8**.

$$\alpha_\sigma(\omega) = \sum_{ij} f_{ij,\sigma} \delta(\varepsilon - \Delta\varepsilon_{ij,\sigma}) \quad (8.7.)$$

$$a(\omega) = a_\alpha(\omega) + a_\beta(\omega) \quad (8.8.)$$

To calculate time-dependent spin-resolved PL, we build upon a previously reported method for the determination of time-dependent spin-unresolved PL.²⁰⁵ This method rests on the time propagation of the excited states, facilitated by energy dissipation into phonons. In this method there are five stages of computation: thermostat modeling, molecular dynamics (MD), non-adiabatic couplings (NAC), Redfield dissipative dynamics, and computation of photoemission. Briefly, a room temperature adiabatic MD simulation on the model in question is ran with $\sum_{I=1}^{N^{ion}} \frac{M_I}{2} \left(\frac{d\vec{R}_I}{dt}\right)_{t=0}^2 = \frac{3}{2} N^{ion} k_B T$ used as thermostat, where M_I and \vec{R}_I are the mass and position of ion I , respectively and N^{ion} is the total number of ions. Ion position changes as a function of time by Newton's equation of motion

$$\frac{d^2}{dt^2} \vec{R}_I = \vec{F}_I / M_I \quad (8.9.)$$

which consequently alter the KS orbitals, giving $\varepsilon_{i,\sigma}(t) = \varepsilon_{i,\sigma}(\vec{R}_I(t))$. NACs determined “on-the-fly”,²⁸¹ are then used to calculate the components of the Redfield Tensor, R_{ijml} . The Redfield Tensor and Fock Matrix, $H_{ij,\sigma} = \delta_{ij}\varepsilon_{i\sigma}(t)$, are then used in the Redfield Master Equation²⁸² (**Eq. 8.10**) to calculate time dependent orbital occupation;

$$\dot{\rho}_{ij,\sigma} = \frac{i}{\hbar} \sum_k (H_{ik,\sigma} \rho_{kj,\sigma} - \rho_{jk,\sigma} H_{ki,\sigma}) + \sum_{lm} R_{ijml,\sigma} \rho_{lm,\sigma} \quad (8.10.)$$

With knowledge of the spin resolved orbital occupation, $\rho_{ii,\sigma}(t)$ as a function of time the time dependent and steady state PL can be calculated using **Eq. 8.11** and **Eq. 8.13**, respectively;

$$E_\sigma(\omega, t) = \sum_{ij} f_{ij\sigma} \delta(\varepsilon - \Delta\varepsilon_{ij\sigma}) (\rho_{jj\sigma}(t) - \rho_{ii\sigma}(t)), \quad (8.11.)$$

$$E_\sigma(\omega) = \int_0^\infty dt E_\sigma(\omega, t). \quad (8.12.)$$

Summing over both the PL for both alpha and beta spins result in the total PL,

$$E(\omega) = E_\alpha(\omega) + E_\beta(\omega). \quad (8.13.)$$

The AgNC modeled in this study is shown in the inset of **Figure 8.1a**. Small metal clusters like this exhibit a broad variety of isomers with multiple geometries yielding similar energies. Iterative scanning of the size and shape of the cluster is beyond the scope of this paper; instead we focus primarily on optimizing the electronic configuration in a selected high-symmetry cluster, Ag₁₃, a typical geometry for transition metal clusters.^{283,284,285,286} This model consists of thirteen silver atoms in the icosahedral geometry with one central Ag atom and twelve surface shell silver atoms. The surface of the AgNC is passivated by a cytosine base, representative of DNA, constituting the simplest spherical cluster model.

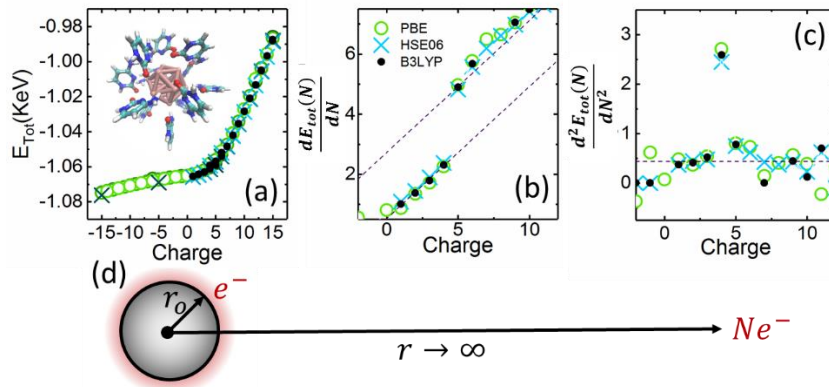


Figure 8.1. The (a) total energy as a function of charge for the modeled nanocluster (inset) with the corresponding (b) first (c) and second derivative. The purple dashed lines in (b) are linear fits of the form $\frac{dE}{dN} = A_1 + BN$ and $\frac{dE}{dN} = A_2 + BN$ such that $A_1 < A_2$. The jump discontinuity here represents a deviation from classic electrostatics as quantum mechanical effects become important. (d) Charge constrained DFT was used for each calculation where an electron is removed from the silver nanocluster. Green circle, blue cross, and black dot stand for PBE, HSE06, and B3LYP data, respectively. Reprinted with permission from Ref. [80]. Copyright 2017 American Chemical Society.

The VASP suite was used for all electronic structure simulations with PAW potentials.²⁸⁷⁻

²⁹⁰ The ground state (GS) geometry of the modeled AgNC was optimized using DFT with the PBE functional.²⁸⁹ Electronic wave functions were expanded in a plane wave basis set with a kinetic energy cutoff of 500 eV. The atoms in the unit cell are fully relaxed until the force on each atom is less than 0.01 eV/Å. Spin resolved DFT calculations were performed with one Generalized Gradient Approximation (GGA) functional PBE, and two hybrid models, namely Heyd-Scuseria-Ernzerhof (HSE06),²⁹¹ and Becke, 3-parameter, Lee-Yang-Parr (B3LYP)^{292,293} exchange-correlation kernels. In an attempt to avoid spurious interactions, periodic boundary conditions (PBC) are implemented with 8 Å of vacuum added in each direction.

8.3. Results

To begin our analysis, we examine the energy-charge space of the modeled AgNC. **Figure 8.1a** plots the total energy as a function of charge, $E_{tot}(N)$, which takes the general form of a

quadratic function. This is consistent with the findings of Meng *et al.* for platinum nanoclusters.²⁹⁴ In general a system with higher energy will be less stable. Here we see minor differences between the total energies of different multiplicities, yet a strong coupling to the charge of the nanocluster and, although, it is possible that the sextet multiplicity would lead to a more stable complex due to the 5 nearly degenerate singly occupied d- orbitals we did not examine this specific multiplicity.

Figures 8.1b and **c** show the first derivative, $\left(\frac{dE_{tot}(N)}{dN}\right)$, and second derivative, $\left(\frac{d^2E_{tot}(N)}{dN^2}\right)$, of $E_{tot}(N)$ with respect to charge, which are expected to show linear and constant dependence on N . Here we only use the singlet and doublet GS configurations to determine $\frac{dE_{tot}(N)}{dN}$ and $\frac{d^2E_{tot}(N)}{dN^2}$, although we calculate the total energy for the singlet, doublet, triplet and quartet GS configuration. The first derivative $\frac{dE_{tot}(N)}{dN}$ exhibits a linear trend with a jump discontinuity present at a charge of 5+. These trends are fit with two lines per **Eq. 8.14** below as illustrated in **Figure 8.1b**

$$\frac{dE(N)}{dN} - BN = \begin{cases} A_1, N < 5 \\ A_2, N > 5 \end{cases} \quad (8.14.)$$

where B is the slope of the line and $A_{1,2}$ is a constant. Interestingly, on either side of the jump discontinuity we see that the slope of the line does not change ($B \approx 0.439$) and the only difference is found between the two values of the constant ($\Delta A = A_2 - A_1 \approx 2.2eV$). The derivative of **Eq. 8.14**, $\frac{d^2E(N)}{dN^2}$, is dependent only on the slope, B , which is applicable to the entire range excluding $N = 4$.

$$\frac{d^2E(N)}{dN^2} = B, N \neq 4 \quad (8.15.)$$

Eq. 8.15 is illustrated in **Figure 8.1c** with a purple dashed line, where a nice fit of the data is observed aside from the deviation at a charge of 4+. The discrepancy at 4+ is indicative of the jump discontinuity in **Figure 8.1b**.

Turning our attention to the nature of the electronic structure of the AgNC, we show the spin resolved band gap of the AgNC modeled as a function of the total number of electrons (**Figure 8.2a-c**). Because of the spin resolved nature of these calculations, a band gap for both alpha, $\Delta\varepsilon_{\alpha}^{gap}(N, \Delta N_{\uparrow\downarrow})$, and beta, $\Delta\varepsilon_{\beta}^{gap}(N, \Delta N_{\uparrow\downarrow})$, electrons is calculated, where in order to visually display both, the band gap of the beta electrons is multiplied by -1 (**Figures 8.2a-d**). As we examine the band structure of these models, we keep a keen eye open for structures having a semiconducting band gap (~ 1 to 3 eV), as this has the greatest potential for fluorescence. **Figure 8.2a-d** shows that that the band gap is semiconducting (~ 2 eV) in nature at a charge of 5+ or greater regardless of GS configuration and once opened, the gap value is only slightly coupled to the charge and exchange correlation functional. We take a quick aside to mention that several experimental reports have indicated the influence charge has on the overall PL. Interestingly, our calculations indicate that although a high charge is necessary for PL, it has a negligible impact on the HOMO-LUMO gap once it is opened, indicating that factors such as morphology and passivation play a key role in the PL.

Redolent of the discontinuity in **Figure 8.1b**, we see that the band gap for both alpha and beta electrons is open only when the charge is 5+ or greater, regardless of GS configuration. To further demonstrate the similarity between the discontinuity in $\frac{dE_{tot}(N)}{dN}$ and the calculated band gap, in **Figure 8.2e** we replot $\frac{dE_{tot}(N)}{dN}$ with a subtracted background of $BN + A_1$, resulting in two lines with no slope per **Eq. 8.16**.

$$\frac{dE(N)}{dN} = \begin{cases} 0, N < 5 \\ \Delta A, N > 5 \end{cases} \quad (8.16.)$$

With the slope of the line removed one can see that not only does the discontinuity occur at the same charge, but also has a comparable amplitude to the DFT calculated band gap.

Figure 8.3c-d shows the DOS for the charged and uncharged AgNC, respectively. The overall structure of the DOS for both models is very similar, yet the extra electrons in the neutrally charged clusters are located in what would be the valence band of the charged model, creating a “pseudogap” and limiting any potential for optical emission. Here a pseudogap refers to a gap of 0.5 eV or greater in the valence band of the DOS.

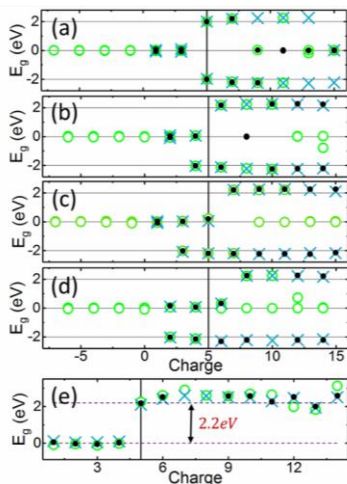


Figure 8.2. The spin resolved band gap as a function of charge for the (a) singlet (b) doublet (c) triplet and (d) quartet ground state configuration. Note that the band gap for beta electrons is multiplied by -1 for clarity. (e) To compare classical results with first principle calculations we replot **Figure 8.1a** with a linear background removed ($\frac{dE}{dN} = A_1 + BN$). The jump discontinuity here is very similar in magnitude to the first principles calculation of the band gap. Note that for each first principle calculation, PBE, HSE06, and B3LYP functionals were used where the same key used to differentiate functional from **Figure 8.1**. applies here: circle, cross, and dot stand for PBE, HSE06, and B3LYP data, respectively. Reprinted with permission from Ref. [80]. Copyright 2017 American Chemical Society.

The neutral cluster has a zero HOMO-LUMO gap, as can be seen in **Figure 8.3d**. However, there’s two noticeable pseudogaps, one between $HOMO_\alpha - 3$ and $HOMO_\alpha - 2$ and the other between $HOMO_\beta - 2$ and $HOMO_\beta - 1$. The DOS of the neutral model looks like a DOS of an n-doped semiconductor, however the model with a +5 charge exhibits an open gap, as shown in **Figure 8.3c**. The electronic structures response to the change in charge is schematically summarized in **Figure 8.3a**. We show the spin resolved band gap for alpha and beta electrons with

N equal to 5+, 7+, 9+ and 11+ with open gaps in the singlet GS configuration, $\Delta N_{\uparrow\downarrow} = 0$. As just mentioned, the magnitude of these gaps appears to be independent of the total charge, yet as electrons are removed, and the charge increases the Fermi energy drops.

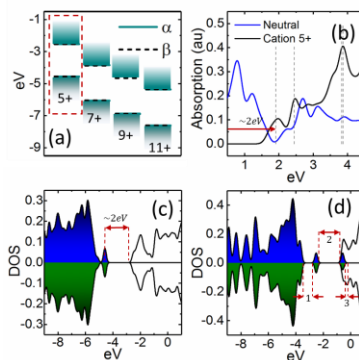


Figure 8.3. (a) Spin resolved band gaps for the singlet ground state configuration for charges of 5+, 7+, 9+ and 11+. (b) The absorption spectra for a silver nanocluster in the 5+ charge state and neutral state are compared to the spin resolved density of states for the (c) charged and (d) neutral state, for reference. Note that in (c) and (d) the beta electronic states are multiplied by -1 and the shaded and unshaded regions represent occupied and unoccupied KS-orbitals, respectively. The vertical dashed lines in (b) are the four most probable optical transitions. In (d) labels 1 and 2 represent the pseudogaps while label 3 represents the formal gap (which is nearly zero in this case). Reprinted with permission from Ref.[80]. Copyright 2017 American Chemical Society.

In **Figure 8.3b**, we calculate the absorption spectra according to **Eq. 8.8** for the AgNC in the singlet 5+ and doublet neutral configuration. Due to the open gap nature of the charged AgNC though, it does not exhibit transitions in the IR range. We also show the four most probable transition in the absorption spectra of the charged AgNC, denoted by vertical dashed lines and building upon this, **Table 8.1** includes the ten most probable elementary excitations across the band gap. The elementary excitations are labeled by the pair of orbitals, $HOMO - i, LUMO + j$ involved in the transition and their corresponding oscillator strength, $f_{HOMO-i, LUMO+j}$, and thermalization rates which will be introduced later. Interestingly, most of the bright transitions occur from the top of the valence band to a relatively large number of orbitals away from the bottom of the conduction band. Typical orbitals involved in absorption and emission reside in the

core prior to excitation and then are promoted to orbitals primarily located on the ligand. Recombination according to Kasha's rule would then occur in the AgNC with both the HOMO and LUMO reside in the nanocluster core.

Table 8.1. Representative inter-band excitations under independent orbital approximation represented by pairs of occupied (hole) and unoccupied (electron) orbitals.

Initial Orbital, i	Final Orbital, j	Oscillator Strength, f_{ij}	Energy of Transition (eV)	Thermalization Lifetimes (τ_e/τ_h) (ps)	Thermalizations Rates (k_e/k_h) (ps^{-1})
HO-2 (319)	LU+5 (327)	3.593789	2.4744	0.3111/3.3146	3.2138/0.3017
HO-1 (320)	LU+25 (347)	3.125815	3.8477	0.9161/5.3967	1.0915/0.1853
HO-1 (320)	LU+23 (345)	1.634268	3.7894	0.9916/5.3967	1.0084/0.1853
HO (321)	LU+26 (348)	1.550391	2.6759	0.9091/--	1.1000/--
HO-2 (319)	LU+10 (332)	1.55031017	2.6759	0.4639/3.3146	2.1558/0.3017
HO (321)	LU+2 (324)	1.38873756	2.22	0.1841/--	5.4315/--
HO-2 (319)	LU+8 (330)	1.28777306	2.6204	0.3463/3.3146	2.8875/0.3017
HO-1 (320)	LU+35 (357)	1.27029564	4.3379	0.9322/5.3967	1.0727/0.1853
HO-2 (319)	LU (322)	1.2570283	2.0617	--/3.3146	--/0.3017
HO (321)	LU (322)	0.260736	2.0137	--/--	--/--

Note: Excitations are chosen out of about 18000 elementary excitations based on larger values of oscillator strength and transition energies vicinity to the bandgap. Note that oscillator strength values computed by **Eq. (3a)** are not normalized here. Last two columns represent thermalization rates and lifetimes for electrons and holes for each given excitation. Interestingly, most of the bright transitions occur from the top of the valence band to relatively large number of orbitals away from the bottom of the conduction band. Note this was all calculated at the PBE level of theory. Reprinted with permission from Ref. [80]. Copyright 2017 American Chemical Society.

Switching gears to electron dynamics and photoemission computations, we focus our attention on one representative configuration, the 5+ singlet state. As a prerequisite to PL calculations an MD simulation was conducted on the AgNC in the 5+ singlet GS configuration, where the total energy of the system was found to randomly fluctuate near approximately

$E_{tot}(t) = -1052 \pm 0.5$ eV, as shown in **Figure 8.4a**. Measuring the distance between the center silver atom (Ag_c) and the other 12 surface silver atoms of our model, we find that the Ag_c -Ag distance harmonically oscillates by ~ 0.1 Å with a mean distance of 2.8 Å. The distance of the three nitrogen atoms in cytosine from the core silver atom (Ag_c -N) fluctuate near 5, 6, and 7 Å means. One could imagine that the jittery oscillations of nitrogen atoms to be expected due to its relatively low molecular weight when compared to silver and the restricted degrees of freedom due to the cyclic ring structure of cytosine. Furthermore, the greatest oscillations are found for primary nitrogen atoms, whereas the amplitude of oscillation in the secondary nitrogen atoms are damped, again likely due to the reduced degrees of freedom.

Figure 8.4d-e shows the fluctuations of the energy of the KS orbitals along the MD trajectory, $\varepsilon_\sigma^i(t)$. The time dependent KS orbitals with the NAC in conjunction with the Redfield master equation can be used to find the orbital occupation as a function of time for any initial excitation specified by the active pairs of orbitals, $HOMO - i$ and $LUMO + j$.²⁹⁵ Most excitations follow two typical trends: (i) the relaxation of one carrier, electron or hole, is independent of where the second carrier is excited to and (ii) the relaxation occurs in a cascade fashion,

$$LUMO + j \rightarrow LUMO + (j - 1) \rightarrow \dots \rightarrow LUMO + 2 \rightarrow LUMO + 1 \rightarrow LUMO,$$

$$HOMO - i \rightarrow HOMO - (i - 1) \rightarrow \dots \rightarrow HOMO - 2 \rightarrow HOMO - 1 \rightarrow HOMO.$$

Based on these trends we deduce that the final stages of the cascade, which are the most important for photoemission, occur through the same sequence of orbitals with the same rates, for a broad range of excitations. A representative example of this thermalization process for an initial excitation of $LUMO + 25$ and $HOMO - 25$ is illustrated in **Figure 8.5a** and **Figure 8.5b**, respectively. As can be seen, the electron relaxes to the LUMO within 300 fs and hole thermalizes

to HOMO-2 in ~ 250 fs and then to the HOMO in ~ 500 fs. The resulting HOMO-LUMO excitation then waits to radiatively recombine via Kasha's rule.²⁰⁵

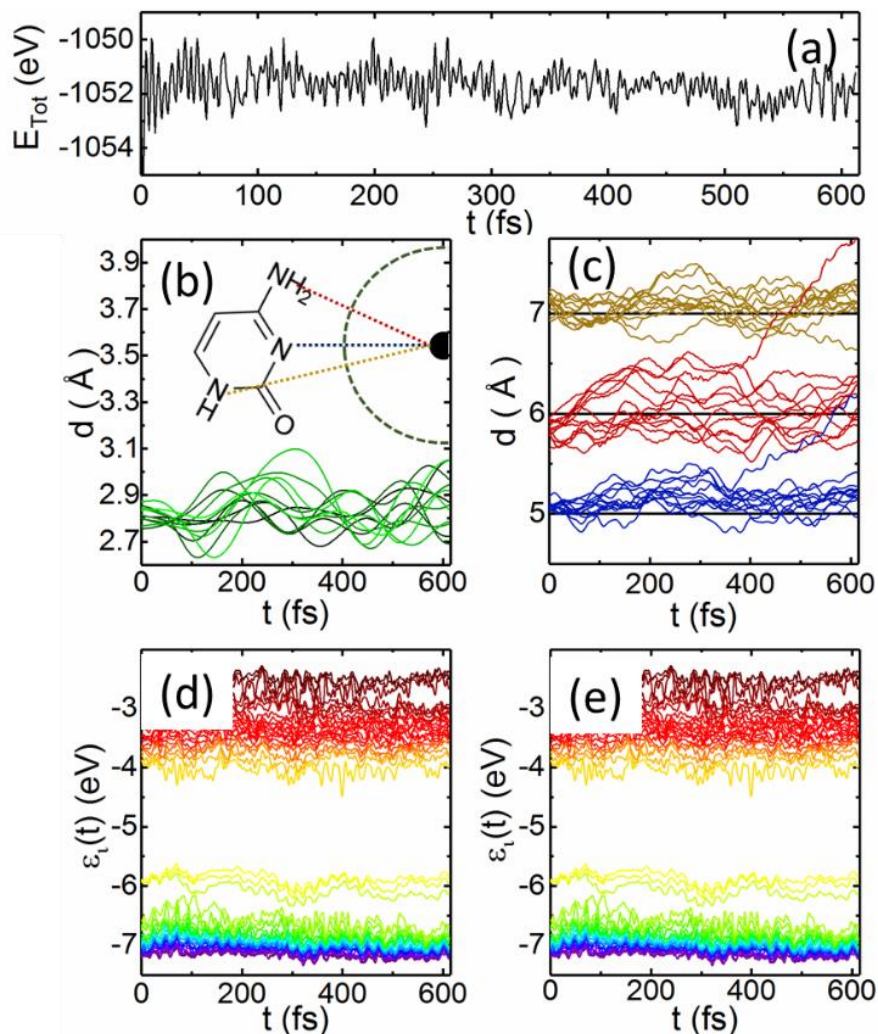


Figure 8.4. Room temperature molecular dynamics simulations were conducted for the 5+ singlet ground state configuration silver nanocluster. The (a) total energy as well as the distance from the center silver atom (b) to outer silver atoms and (c) to nitrogen atoms in cytosine were determined. The colors in (b) and (c) are coded to match the inset of (b). From the molecular simulations, spin resolved time dependent Kohn-Sham orbitals were determined for (d) alpha and (e) beta electrons under PBE functionals. Reprinted with permission from Ref. [80] Copyright 2017 American Chemical Society.

Next, we explore the response of excited state dynamics to the change in the initial excitation. The initial excitation of a charge carrier can be labeled in two fashions: first, by orbital index and second by an offset of orbital energy from the band edge, $|\varepsilon_i - \varepsilon_{LU}|$ for electrons and

$|\varepsilon_{HO} - \varepsilon_i|$ for holes. Here, the dependence on initial excitation is best visualized as a relaxation time, $\tau = k^{-1}$, versus initial excitation energy. The relaxation time of both alpha and beta electrons, $\tau_e = (k_e)^{-1}$ in **Table 8.1** and **Figure 8.5c** are in accordance with the band gap law such that the lifetime increases with increasing excitation energy.²⁹⁶ Contrary to this, however, the hole relaxation times, $\tau_h = (k_h)^{-1}$, exhibit the opposite trend, possibly due to the dense spacing of the KS orbital energy in the valence band.

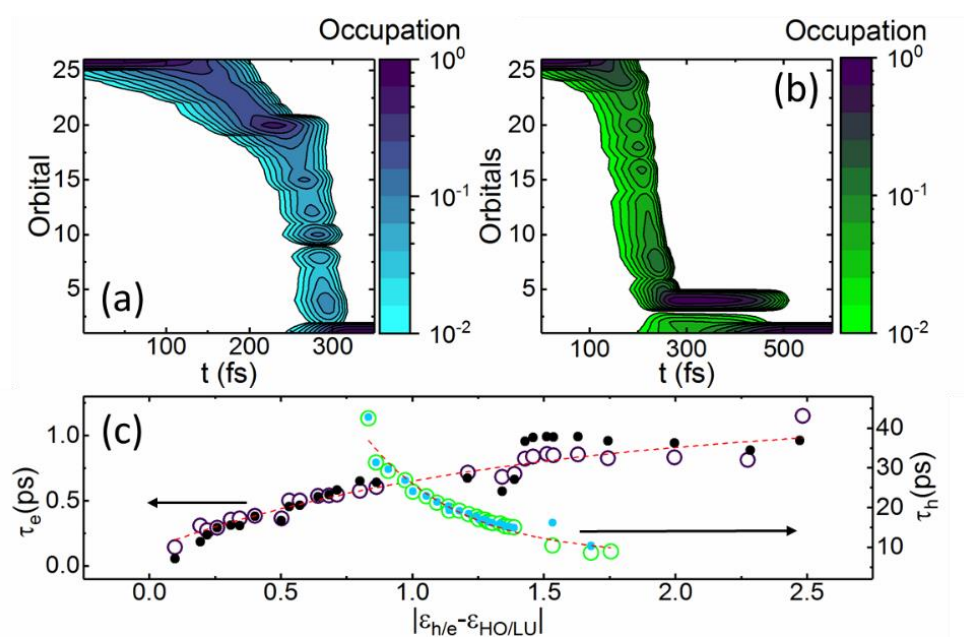


Figure 8.5. The orbital occupation for alpha (a) electrons and (b) holes as a function of time calculated for the silver nanocluster in the 5+ singlet ground state configuration, thermalizing from LUMO+25 to the LUMO and HOMO + 25 to the HOMO, respectively. (c) Calculated electron and hole thermalization lifetimes as a function of the energy difference between the corresponding band edge and the initial excitation level. The solid and open circles represent alpha and beta electrons, respectively, while the black and purple symbols are electron lifetimes and the green and blue symbols represent hole lifetimes. The alpha and beta electrons of both the hole and electron lifetimes are fit with an exponential function (red dashed line). Reprinted with permission from Ref. [80] Copyright 2017 American Chemical Society.

The summation of spin resolved PL by **Eq. 8.13** was used to create the overall PL spectrum in **Figure 8.6** where the peak is centered at approximately 610 nm. Also, in **Figure 8.6** we plot the

absorption spectra according to **Eq. 8.8** and the experimentally observed PL and absorption data from Ref. [75] for oligonucleotide capped AgNC with a 540 nm excitation.

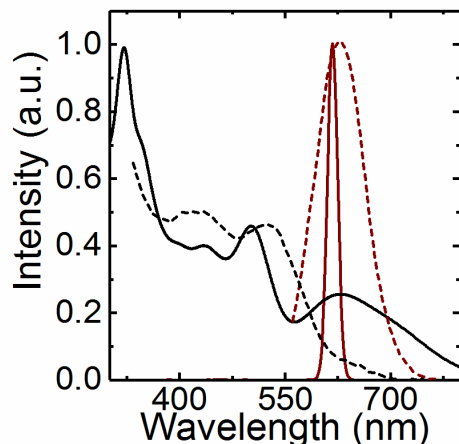


Figure 8.6. Normalized calculated PL (solid red line) and absorption (solid black line) spectra for the 5+ singlet model with experimental PL (dashed red line) and absorption spectra (dashed black line) from Petty (Ref. [75]). Reprinted with permission from Ref. [80]. Copyright 2017 American Chemical Society.

8.4. Discussion

To rationalize the presence of the discontinuity in $\frac{dE_{tot}}{dN}$ we use an electrostatic approach for a metal sphere. First the energy required to remove an electron from a metal sphere (E_{ion}) can be modeled according to Coulomb's Law as given by **Eq. 8.17**,

$$E_{ion} = \Delta E_{tot} = E_{tot}(N) - E_{tot}(N - 1) = -\frac{1}{\epsilon_R} \frac{(Ne)(-Ne)}{|R_0|} \quad (8.17.)$$

where, R_0 is the radius of the conducting metal sphere and ϵ_R is the dielectric constant of the surrounding material in atomic units. The energy dependence scales as a second power in terms of the number of electrons, N , and the first derivative of this ionization term leads to $\frac{dE_{ion}}{dN} = \frac{2e^2}{\epsilon|R_0|} N$.

Fitting the DFT derived data in **Figure 8.1b**, we find a very similar trend, $\frac{dE_{ion}}{dN} = A_{1,2} + BN$, where $A_{1,2}$ is a constant for the data on either side of the jump discontinuity at 5+. We expect this

constant to be directly related to the quantum mechanical nature in the DOS which is neglected in the classical methods used here. Gaps in the DOS will increase the energy required to remove the electron. It is possible that this is the root cause for both deviations seen in **Eq. 8.17** and the actual fit of the data in **Eq. 8.14**. The most prominent difference between **Eq. 8.14** and **Eq. 8.17** lies in the presence of the constant $A_{1,2}$. With the sudden jump at a charge of 5+, we assume that this must have a strong correlation to the presence of the bandgap, due in part to the semblance of ΔA to the DFT calculated band gap. We further assume that the band gap can be approximated from the energy of ionization, E_{ion} , using **Eq. 8.18** below;

$$dE_{ion} \sim E^{gap}(N, R_0, \epsilon) = -\frac{2(Ne)(-e)}{\epsilon |R_0|} = BN \quad (8.18.)$$

From this we see that the band gap of the nanocluster is dependent on the charge and size of the nanocluster as well as the dielectric constant of the surrounding medium.

However, from the DFT generated results we see that the band gap is only weakly coupled to the charge aside from the clear dependence at a charge of 5+ (**Figure 8.2a-d**). Now, we did not explicitly study the effect different surrounding mediums would have on the PL, but a quick literature review reveals that several groups have shown the effect stabilizing ligand and the dispersing solvent play in the observed PL.^{79, 270, 273, 274} For instance, Richards *et al.* and Copp *et al.* were able to tune the AgNC's PL by changing the DNA sequences passivating the AgNC^{82, 270} surface, while Diez *et al.* demonstrated the strong coupling between the solvent and the AgNC PL.²⁷³

Both systems can be explained using the simple model presented here (**Eq. 8.18**). The calculated data from **Figure 8.1b** has a slope of $B \approx 0.439$. Substituting this into **Eq. 8.18** we find that $E^{gap}(+5, 2.756 \text{ \AA}, \epsilon) = 0.439 * 5 = 2.195$, which leads to a dielectric constant of 12.1. To check the validity of this approximation we try to determine the dielectric constant in the near

vicinity of the nanocluster. To the knowledge of the authors, the dielectric constant of cytosine is not given explicitly, but with the volume and polarizability one can use the Clausius-Mossotti relation²⁹⁷ to determine a dielectric constant, which ends up being approximately 3.83 in this case.⁸⁰

Because these nanoparticles are dispersed in water, which has a substantially larger dielectric constant at 80.1, we would suspect it to play a role in the overall dielectric constant of the medium directly surrounding the nanocluster. Here we employ a simple rule of mixtures, $\epsilon_{mix} = \phi_{cyt}\epsilon_{cyt} + \phi_{water}\epsilon_{water}$, where ϕ is the volume fraction and solving for ϕ_{cyt} and ϕ_{water} knowing that $1 = \phi_{cyt} + \phi_{water}$, leads to $\phi_{cyt} = 0.89$ and $\phi_{water} = 0.11$. We find this solution to be reasonable due to the fact that cytosine is in direct contact with the silver sphere and as a result its dielectric constant would have the largest impact on the total dielectric constant while very few water molecules can approach the nanocluster and affect it.

Another approach to examine the jump discontinuity at 5+ is through the lens of superatom physics. Small clusters of metallic atoms or superatoms can take on significantly different properties than that of the bulk. The early work by Walter Knight showed that a cool gas of sodium atoms would condense into clusters containing a specific number of atoms, 8, 20, 40, etc.^{298, 299} The specific number of atoms in a cluster was due to electronic shell closures.

Similar to the noble gases with their filled shells, superatoms can also have exceptional stability with a valence electron count at $n^* = 2, 8, 18, 34, 58, 92, 138, \dots$ due to shell closures.²⁷⁵ Directly relevant to the work here, the group of Häkkinen gave a simple arithmetic expression to predict whether a superatom with organic ligands has a shell closer, $n^* = Nv_A - M - z$, where n^* is the valence electron count corresponding to the list above, N is the number metallic atoms,

ν_A is the number of valence electrons in the metallic atom, M is the number electron withdrawing ligands assuming each ligand withdraws one electron, and z is the overall charge.

In the AgNC studied here a shell closure would correspond to a charge, z , of 5- and 5+ with a shell closure, n^* , of 18 and 8, respectively, due to the 13 metal atoms and the $5S^1$ valence electron in each atom (e.g. $8 = (13)(1) - 0 - 5$ and $18 = (13)(1) - 0 + 5$). Alternatively, if one explicitly counts the 10 electrons in the d- orbitals of silver based on the Aufbau principle, $Ag^{(0)} = [Kr]4d^{10}5S^1$, a shell closure is still observed at a charge of 5+ with a magic shell closure of 138 electrons (e.g. $138 = (13)(11) - 0 - 5$). This indicates that the ligand is not withdraw electrons from the AgNC core ($M = 0$) and perhaps a more intricate ligand structure is adopted.

Ligand stabilization in gold nanoclusters was found to occur through a metal ligand adduct, $M^{(+)}\text{-Ligand}$ with a pure neutral gold core.²⁷⁵ This type of complex could be occurring in DNA complexed AgNC where there is an inner neutral core of silver atoms surrounded by positively charged $Ag^+\text{-DNA}$ adducts. This type of complex has been hypothesized by Petty *et al.*⁸¹ and by Copp *et al.*⁸² with their work on DNA – AgNC complexes.

8.5. Conclusions

AgNCs are ideal fluorophores for biological systems with their high photostability, relatively non-toxic nature, and small footprint.⁷² Yet, despite several inspiring proof-of-concept sensors^{76, 79, 81} and biolabels,²⁷² a compelling model of the PL has been lacking. Herein the results of spin-resolved, constrained DFT calculations of an icosahedron shaped AgNC passivated with cytosine. The electronic structure of AgNC was calculated for various charges. Due to the sensitivity of the optical properties and their surrounding environment, it was found that a relatively high charge of 5+ or greater is necessary for the nanocluster to become optically active for electrons of either spins. However, the charge played a small role on the overall PL.

We report a new method to estimate the band gap of semiconducting nanoparticles through careful examination of the total energy as a function of charge using a classical electron dynamics method. The first derivative with respect to charge of the total energy was found to be linear in nature, yet a discontinuity was present at a charge of $5+$, where the amplitude of the jump coincided with the calculated band gap of approximately 2 eV. Using a classic coulombic model, we rationalized the observed behavior proposing that the band gap is inversely dependent to the dielectric constant of the surrounding material. This intuitively speaks to the nature of the sensitivity of photoemission to the surface passivation.

Methodologies presented for the calculation of spin resolved PL are general and can be applied to a broad variety of other nanoscale systems. This application is exemplified on a silver nanocluster model as a proof of concept, thus overcoming lack of atomistic simulations of PL properties in such systems. The calculated PL and absorption spectra show similarities to experimental data, giving credibility to the validity of the methodologies described here.

REFERENCES

1. Feynman, R. P., There's Plenty of Room at the Bottom. *Engineering and Science*: **1960**, 23, 22-36.
2. Sun, S. H.; Murray, C. B.; Weller, D.; Folks, L.; Moser, A., Monodisperse FePt Nanoparticles and Ferromagnetic FePt Nanocrystal Superlattices. *Science* **2000**, 287 (5460), 1989-1992.
3. Eigler, D. M.; Schweizer, E. K., Positioning Single Atoms with a Scanning Tunneling Microscope. *Nature* **1990**, 344 (6266), 524-526.
4. Schrodinger, E., Quantisation as an Eigen Value Problem. *Annalen Der Physik* **1926**, 79 (4), 361-U8.
5. Murray, C. B.; Norris, D. J.; Bawendi, M. G., Synthesis and Characterization of Nearly Monodisperse CdE (E = S, Se, Te) Semiconductor Nanocrystallites. *Journal of the American Chemical Society* **1993**, 115 (19), 8706-8715.
6. Ekimov, A. I.; Onushchenko, A. A., Quantum Size Effect in 3-Dimensional Microscopic Semiconductor Crystals. *JETP Letters* **1981**, 34 (6), 345-349.
7. Rossetti, R.; Nakahara, S.; Brus, L. E., Quantum Size Effects in the Redox Potentials, Resonance Raman-Spectra, and Electronic-Spectra of CdS Crystallites in Aqueous-Solution. *Journal of Chemical Physics* **1983**, 79 (2), 1086-1088.
8. Novoselov, K. S.; Geim, A. K.; Morozov, S. V.; Jiang, D.; Zhang, Y.; Dubonos, S. V.; Grigorieva, I. V.; Firsov, A. A., Electric Field Effect in Atomically Thin Carbon Films. *Science* **2004**, 306 (5696), 666-669.
9. Srinivasan, C., Do Damascus Swords Reveal India's Mastery of Nanotechnology? *Current Science* **2007**, 92 (3), 279-280.
10. Reibold, M.; Paufler, P.; Levin, A. A.; Kochmann, W.; Patzke, N.; Meyer, D. C., Materials - Carbon Nanotubes in an Ancient Damascus Sabre. *Nature* **2006**, 444 (7117), 286-286.
11. Freestone, I.; Meeks, N.; Sax, M.; Higgitt, C., The Lycurgus Cup - A Roman Nanotechnology. *Gold Bulletin* **2007**, 40 (4), 270-277.
12. Zsigmondy, R.; Heyer, R., The Purification of Colloids by Means of Dialysis. *Zeitschrift Fur Anorganische Chemie* **1910**, 68 (3), 169-187.
13. Zsigmondy, R., Coagulation and Particle Attraction. *Zeitschrift Fur Physikalische Chemie-Stoichiometrie Und Verwandtschaftslehre* **1918**, 92 (5), 600-639.
14. Zsigmondy, R.; Joel, E., Gold Protection and Precipitation by Protein. *Zeitschrift Fur Physikalische Chemie-Stoichiometrie Und Verwandtschaftslehre* **1924**, 113 (3/4), 299-312.

15. Langmuir, I., The Adsorption of Gases on Plane Surfaces of Glass, Mica and Platinum. *Journal of the American Chemical Society* **1918**, *40*, 1361-1403.
16. Blodgett, K. B., Films Built by Depositing Successive Monomolecular Layers on a Solid Surface. *Journal of the American Chemical Society* **1935**, *57* (1), 1007-1022.
17. Blodgett, K. B.; Langmuir, I., Built-up Films of Barium Stearate and their Optical Properties. *Physical Review* **1937**, *51* (11), 0964-0982.
18. Taniguchi, N. In *On the Basic Concept of Nanotechnology*, Proceedings of the International Conference on Production Engineering, Tokyo, 1974.
19. Kroto, H. W.; Heath, J. R.; O'Brien, S. C.; Curl, R. F.; Smalley, R. E., C-60 - Buckminsterfullerene. *Nature* **1985**, *318* (6042), 162-163.
20. Brus, L., Electronic Wave-Functions in Semiconductor Clusters - Experiment and Theory. *Journal of Physical Chemistry* **1986**, *90* (12), 2555-2560.
21. Canham, L. T., Silicon Quantum Wire Array Fabrication by Electrochemical and Chemical Dissolution of Wafers. *Applied Physics Letters* **1990**, *57* (10), 1046-1048.
22. Iijima, S., Helical Microtubules of Graphitic Carbon. *Nature* **1991**, *354* (6348), 56-58.
23. Zhou, H. S.; Honma, I.; Komiyama, H.; Haus, J. W., Controlled Synthesis and Quantum-Size Effect in Gold-Coated Nanoparticles. *Physical Review B* **1994**, *50* (16), 12052-12056.
24. Barbosa, S.; Agrawal, A.; Rodriguez-Lorenzo, L.; Pastoriza-Santos, I.; Alvarez-Puebla, R. A.; Kornowski, A.; Weller, H.; Liz-Marzan, L. M., Tuning Size and Sensing Properties in Colloidal Gold Nanostars. *Langmuir* **2010**, *26* (18), 14943-14950.
25. Sau, T. K.; Murphy, C. J., Room temperature, high-yield synthesis of multiple shapes of gold nanoparticles in aqueous solution. *Journal of the American Chemical Society* **2004**, *126* (28), 8648-8649.
26. Jurbergs, D.; Rogojina, E.; Mangolini, L.; Kortshagen, U., Silicon Nanocrystals with Ensemble Quantum Yields Exceeding 60%. *Applied Physics Letters* **2006**, *88* (23).
27. Boles, M. A.; Ling, D.; Hyeon, T.; Talapin, D. V., The Surface Science of Nanocrystals. *Nature Materials* **2016**, *15* (2), 141-153.
28. Panthani, M. G.; Hessel, C. M.; Reid, D.; Casillas, G.; Jose-Yacaman, M.; Korgel, B. A., Graphene-Supported High-Resolution TEM and STEM Imaging of Silicon Nanocrystals and their Capping Ligands. *Journal of Physical Chemistry C* **2012**, *116* (42), 22463-22468.
29. Li, Q.; Luo, T. Y.; Zhou, M.; Abroshan, H.; Huang, J. C.; Kim, H. J.; Rosi, N. L.; Shao, Z. Z.; Jin, R. C., Silicon Nanoparticles with Surface Nitrogen: 90% Quantum Yield with Narrow Luminescence Bandwidth and the Ligand Structure Based Energy Law. *ACS Nano* **2016**, *10* (9), 8385-8393.

30. Dasog, M.; De los Reyes, G. B.; Titova, L. V.; Hegmann, F. A.; Veinot, J. G. C., Size vs Surface: Tuning the Photoluminescence of Freestanding Silicon Nanocrystals Across the Visible Spectrum via Surface Groups. *ACS Nano* **2014**, *8* (9), 9636-9648.
31. Kovalenko, M. V.; Scheele, M.; Talapin, D. V., Colloidal Nanocrystals with Molecular Metal Chalcogenide Surface Ligands. *Science* **2009**, *324* (5933), 1417-1420.
32. Dabbousi, B. O.; RodriguezViejo, J.; Mikulec, F. V.; Heine, J. R.; Mattoussi, H.; Ober, R.; Jensen, K. F.; Bawendi, M. G., (CdSe)/ZnS Core-Shell Quantum Dots: Synthesis and Characterization of a Size Series of Highly Luminescent Nanocrystallites. *Journal of Physical Chemistry B* **1997**, *101* (46), 9463-9475.
33. Reiss, P.; Protiere, M.; Li, L., Core/Shell Semiconductor Nanocrystals. *Small* **2009**, *5* (2), 154-168.
34. Yong, K. T.; Law, W. C.; Hu, R.; Ye, L.; Liu, L. W.; Swihart, M. T.; Prasad, P. N., Nanotoxicity Assessment of Quantum Dots: From Cellular to Primate Studies. *Chemical Society Reviews* **2013**, *42* (3), 1236-1250.
35. Smalley, R. E., Future Global Energy Prosperity: The Terawatt Challenge. *MRS Bulletin* **2005**, *30* (6), 412-417.
36. BP Statistical Review of World Energy June 2017. (accessed 12-22-17).
37. Shockley, W.; Queisser, H. J., Detailed Balance Limit of Efficiency of P-N Junction Solar Cells. *Journal of Applied Physics* **1961**, *32* (3), 510-&.
38. Semonin, O. E.; Luther, J. M.; Choi, S.; Chen, H. Y.; Gao, J. B.; Nozik, A. J.; Beard, M. C., Peak External Photocurrent Quantum Efficiency Exceeding 100% via MEG in a Quantum Dot Solar Cell. *Science* **2011**, *334* (6062), 1530-1533.
39. Beard, M. C.; Knutsen, K. P.; Yu, P. R.; Luther, J. M.; Song, Q.; Metzger, W. K.; Ellingson, R. J.; Nozik, A. J., Multiple Exciton Generation in Colloidal Silicon Nanocrystals. *Nano Letters* **2007**, *7* (8), 2506-2512.
40. Beard, M. C., Multiple Exciton Generation in Semiconductor Quantum Dots. *Journal of Physical Chemistry Letters* **2011**, *2* (11), 1282-1288.
41. Kryjevski, A.; Kilin, D., Multiple Exciton Generation in Silicon Quantum Dot Arrays: Density Functional Perturbation Theory Computation. *Molecular Physics* **2014**, *112* (3-4), 430-440.
42. Nelson, C. A.; Monahan, N. R.; Zhu, X. Y., Exceeding the Shockley-Queisser limit in Solar Energy Conversion. *Energy & Environmental Science* **2013**, *6* (12), 3508-3519.

43. Nozik, A. J.; Beard, M. C.; Luther, J. M.; Law, M.; Ellingson, R. J.; Johnson, J. C., Semiconductor Quantum Dots and Quantum Dot Arrays and Applications of Multiple Exciton Generation to Third-Generation Photovoltaic Solar Cells. *Chemical Reviews* **2010**, *110* (11), 6873-6890.
44. Yi, J. C., Miniband Properties of Superlattice Quantum Dot Arrays Fabricated by the Edge-Defined Nanowires. *Microelectronics Journal* **2008**, *39* (3-4), 369-374.
45. Jiang, C. W.; Green, M. A., Silicon Quantum Dot Superlattices: Modeling of Energy Bands, Densities of States, and Mobilities for Silicon Tandem Solar Cell Applications. *Journal of Applied Physics* **2006**, *99* (11).
46. Voros, M.; Galli, G.; Zimanyi, G. T., Colloidal Nanoparticles for Intermediate Band Solar Cells. *ACS Nano* **2015**, *9* (7), 6882-6890.
47. Mendes, M. J.; Hernandez, E.; Lopez, E.; Garcia-Linares, P.; Ramiro, I.; Artacho, I.; Antolin, E.; Tobias, I.; Marti, A.; Luque, A., Self-Organized Colloidal Quantum Dots and Metal Nanoparticles for Plasmon-Enhanced Intermediate-Band Solar Cells. *Nanotechnology* **2013**, *24* (34), 12.
48. Sergio Brovelli Meinardi, F. C., Annalisa Velizhanin, Kirill A. Simonutti, Roberto Lorenzon, Monica Beverina, Luca Viswanatha, Ranjani Klimov, Victor I. Brovelli, Sergio., Large-Area Luminescent Solar Concentrators Based on 'Stokes-Shift-Engineered' Nanocrystals in a Mass-Polymerized PMMA Matrix. *Nature Photonics* **2014**, *8*, 392-399.
49. Meinardi, F.; Ehrenberg, S.; Dharmo, L.; Carulli, F.; Mauri, M.; Bruni, F.; Simonutti, R.; Kortshagen, U.; Brovelli, S., Highly Efficient Luminescent Solar Concentrators Based on Earth-Abundant Indirect-Bandgap Silicon Quantum Dots. *Nature Photonics* **2017**, *11* (3), 177-+.
50. Bronstein, N. D.; Yao, Y.; Xu, L.; O'Brien, E.; Powers, A. S.; Ferry, V. E.; Alivisatos, A. P.; Nuzzo, R. G., Quantum Dot Luminescent Concentrator Cavity Exhibiting 30-fold Concentration. *Acs Photonics* **2015**, *2* (11), 1576-1583.
51. Mulligan, C. J.; Wilson, M.; Bryant, G.; Vaughan, B.; Zhou, X.; Belcher, W. J.; Dastoor, P. C., A Projection of Commercial-Scale Organic Photovoltaic Module Costs. *Solar Energy Materials and Solar Cells* **2014**, *120*, 9-17.
52. Mulligan, C. J.; Bilen, C.; Zhou, X. J.; Belcher, W. J.; Dastoor, P. C., Levelised Cost of Electricity for Organic Photovoltaics. *Solar Energy Materials and Solar Cells* **2015**, *133*, 26-31.
53. Stratakis, E.; Kymakis, E., Nanoparticle-Based Plasmonic Organic Photovoltaic Devices. *Materials Today* **2013**, *16* (4), 133-146.
54. 8 Advantages of LED Lighting.

55. Shirasaki, Y.; Supran, G. J.; Bawendi, M. G.; Bulovic, V., Emergence of Colloidal Quantum-Dot Light-Emitting Technologies. *Nature Photonics* **2013**, *7* (1), 13-23.
56. Maier-Flaig, F.; Rinck, J.; Stephan, M.; Bocksrocker, T.; Bruns, M.; Kubel, C.; Powell, A. K.; Ozin, G. A.; Lemmer, U., Multicolor Silicon Light-Emitting Diodes (SiLEDs). *Nano Letters* **2013**, *13* (2), 475-480.
57. Delehanty, J. B.; Mattoussi, H.; Medintz, I. L., Delivering Quantum Dots into Cells: Strategies, Progress and Remaining Issues. *Analytical and Bioanalytical Chemistry* **2009**, *393* (4), 1091-1105.
58. Farokhzad, O. C.; Cheng, J. J.; Teply, B. A.; Sherifi, I.; Jon, S.; Kantoff, P. W.; Richie, J. P.; Langer, R., Targeted Nanoparticle-aptamer Bioconjugates for Cancer Chemotherapy in vivo. *Proceedings of the National Academy of Sciences of the United States of America* **2006**, *103* (16), 6315-6320.
59. Wang, S. P.; Mamedova, N.; Kotov, N. A.; Chen, W.; Studer, J., Antigen/Antibody Immunocomplex from CdTe Nanoparticle Bioconjugates. *Nano Letters* **2002**, *2* (8), 817-822.
60. O'Neal, D. P.; Hirsch, L. R.; Halas, N. J.; Payne, J. D.; West, J. L., Photo-Thermal Tumor Ablation in Mice Using Near Infrared-Absorbing Nanoparticles. *Cancer Letters* **2004**, *209* (2), 171-176.
61. Maeda, H.; Fang, J.; Inutsuka, T.; Kitamoto, Y., Vascular Permeability Enhancement in Solid Tumor: Various Factors, Mechanisms Involved and Its Implications. *International Immunopharmacology* **2003**, *3* (3), 319-328.
62. Maeda, H., The Enhanced Permeability And Retention (EPR) Effect In Tumor Vasculature: The Key Role Of Tumor-Selective Macromolecular Drug Targeting. *Advances in Enzyme Regulation, Vol 41* **2001**, *41*, 189-207.
63. Chen, W. R.; Adams, R. L.; Carubelli, R.; Nordquist, R. E., Laser-photosensitizer assisted immunotherapy: A Novel Modality for Cancer Treatment. *Cancer Letters* **1997**, *115* (1), 25-30.
64. Jolesz, F. A.; Hynynen, K., Magnetic Resonance Image-Guided Focused Ultrasound Surgery. *Cancer Journal* **2002**, *8*, S100-S112.
65. Gazelle, G. S.; Goldberg, S. N.; Solbiati, L.; Livraghi, T., Tumor Ablation with Radio-Frequency Energy. *Radiology* **2000**, *217* (3), 633-646.
66. Forster, T., *Zwischenmolekulare Energiewanderung und Fluoreszenz. *Annalen Der Physik* **1948**, *2* (1-2), 55-75.
67. Medintz, I. L.; Clapp, A. R.; Mattoussi, H.; Goldman, E. R.; Fisher, B.; Mauro, J. M., Self-Assembled Nanoscale Biosensors Based on Quantum Dot FRET Donors. *Nature Materials* **2003**, *2* (9), 630-638.

68. Chou, K. F.; Dennis, A. M., Forster Resonance Energy Transfer between Quantum Dot Donors and Quantum Dot Acceptors. *Sensors* **2015**, *15* (6), 13288-13325.
69. Shamirian, A.; Ghai, A.; Snee, P. T., QD-Based FRET Probes at a Glance. *Sensors* **2015**, *15* (6), 13028-13051.
70. Hildebrandt, N.; Spillmann, C. M.; Algar, W. R.; Pons, T.; Stewart, M. H.; Oh, E.; Susumu, K.; Diaz, S. A.; Delehanty, J. B.; Medintz, I. L., Energy Transfer with Semiconductor Quantum Dot Bioconjugates: A Versatile Platform for Biosensing, Energy Harvesting, and Other Developing Applications. *Chemical Reviews* **2017**, *117* (2), 536-711.
71. Algar, W. R.; Tavares, A. J.; Krull, U. J., Beyond labels: A Review of the Application of Quantum Dots as Integrated Components of Assays, Bioprobes, and Biosensors Utilizing Optical Transduction. *Analytica Chimica Acta* **2010**, *673* (1), 1-25.
72. Diez, I.; Ras, R. H. A., Fluorescent Silver Nanoclusters. *Nanoscale* **2011**, *3* (5), 1963-1970.
73. Le Guevel, X.; Spies, C.; Daum, N.; Jung, G.; Schneider, M., Highly Fluorescent silver nanoclusters stabilized by glutathione: a promising fluorescent label for bioimaging. *Nano Research* **2012**, *5* (6), 379-387.
74. Koszinowski, K.; Ballweg, K., A Highly Charged Ag-6(4+) Core in a DNA-Encapsulated Silver Nanocluster. *Chemistry-a European Journal* **2010**, *16* (11), 3285-3290.
75. Petty, J. T.; Zheng, J.; Hud, N. V.; Dickson, R. M., DNA-templated Ag nanocluster formation. *Journal of the American Chemical Society* **2004**, *126* (16), 5207-5212.
76. Petty, J. T.; Sergev, O. O.; Kantor, A. G.; Rankine, I. J.; Ganguly, M.; David, F. D.; Wheeler, S. K.; Wheeler, J. F., Ten-Atom Silver Cluster Signaling and Tempering DNA Hybridization. *Analytical Chemistry* **2015**, *87* (10), 5302-5309.
77. Schultz, D.; Gardner, K.; Oemrawsingh, S. S. R.; Markesevic, N.; Olsson, K.; Debord, M.; Bouwmeester, D.; Gwinn, E., Evidence for Rod-Shaped DNA-Stabilized Silver Nanocluster Emitters. *Advanced Materials* **2013**, *25* (20), 2797-2803.
78. Sharma, J.; Yeh, H. C.; Yoo, H.; Werner, J. H.; Martinez, J. S., A Complementary Palette of Fluorescent Silver Nanoclusters. *Chemical Communications* **2010**, *46* (19), 3280-3282.
79. Yeh, H. C.; Sharma, J.; Han, J. J.; Martinez, J. S.; Werner, J. H., A DNA-Silver Nanocluster Probe That Fluoresces upon Hybridization. *Nano Letters* **2010**, *10* (8), 3106-3110.
80. Brown, S. L.; Hobbie, E. K.; Tretiak, S.; Kilin, D. S., First-Principles Study of Fluorescence in Silver Nanoclusters. *Journal of Physical Chemistry C* **2017**, *121* (43), 23875-23885.
81. Petty, J. T.; Sergev, O. O.; Ganguly, M.; Rankine, I. J.; Chevrier, D. M.; Zhang, P., A Segregated, Partially Oxidized, and Compact Ag-10 Cluster within an Encapsulating DNA Host. *Journal of the American Chemical Society* **2016**, *138* (10), 3469-3477.

82. Copp, S. M.; Schultz, D.; Swasey, S.; Pavlovich, J.; Debord, M.; Chiu, A.; Olsson, K.; Gwinn, E., Magic Numbers in DNA-Stabilized Fluorescent Silver Clusters Lead to Magic Colors. *Journal of Physical Chemistry Letters* **2014**, *5* (6), 959-963.
83. Poland, C. A.; Duffin, R.; Kinloch, I.; Maynard, A.; Wallace, W. A. H.; Seaton, A.; Stone, V.; Brown, S.; MacNee, W.; Donaldson, K., Carbon Nanotubes Introduced into the Abdominal Cavity of Mice Show Asbestos-like Pathogenicity in a Pilot Study. *Nature Nanotechnology* **2008**, *3* (7), 423-428.
84. Sharifi, S.; Behzadi, S.; Laurent, S.; Forrest, M. L.; Stroeve, P.; Mahmoudi, M., Toxicity of Nanomaterials. *Chemical Society Reviews* **2012**, *41* (6), 2323-2343.
85. Toyokuni, S., Genotoxicity and Carcinogenicity Risk of Carbon Nanotubes. *Advanced Drug Delivery Reviews* **2013**, *65* (15), 2098-2110.
86. Buzea, C.; Pacheco, II; Robbie, K., Nanomaterials and Nanoparticles: Sources and Toxicity. *Biointerphases* **2007**, *2* (4), MR17-MR71.
87. Wang, X. Z.; Yang, Y.; Li, R. F.; McGuinness, C.; Adamson, J.; Megson, I. L.; Donaldson, K., Principal Component and Causal Analysis of Structural and Acute in Vitro Toxicity Data for Nanoparticles. *Nanotoxicology* **2014**, *8* (5), 465-476.
88. Braydich-Stolle, L.; Hussain, S.; Schlager, J. J.; Hofmann, M. C., In vitro Cytotoxicity of Nanoparticles in Mammalian Germline Stem Cells. *Toxicological Sciences* **2005**, *88* (2), 412-419.
89. Hardman, R., A toxicologic review of quantum dots: Toxicity Depends on Physicochemical and Environmental Factors. *Environmental Health Perspectives* **2006**, *114* (2), 165-172.
90. King-Heiden, T. C.; Wiecinski, P. N.; Mangham, A. N.; Metz, K. M.; Nesbit, D.; Pedersen, J. A.; Hamers, R. J.; Heideman, W.; Peterson, R. E., Quantum Dot Nanotoxicity Assessment Using the Zebrafish Embryo. *Environmental Science & Technology* **2009**, *43* (5), 1605-1611.
91. Mahendra, S.; Zhu, H. G.; Colvin, V. L.; Alvarez, P. J., Quantum Dot Weathering Results in Microbial Toxicity. *Environmental Science & Technology* **2008**, *42* (24), 9424-9430.
92. Meng, H.; Chen, Z.; Xing, G.; Yuan, H.; Chen, C.; Zhao, F.; Zhang, C.; Zhao, Y., Ultrahigh Reactivity Provokes Nanotoxicity: Explanation of Oral Toxicity of Nano-Copper Particles. *Toxicology Letters* **2007**, *175* (1-3), 102-110.
93. Sun, H. Z.; Zhang, F.; Wei, H. T.; Yang, B., The Effects of composition and Surface Chemistry on the Toxicity of Quantum Dots. *Journal of Materials Chemistry B* **2013**, *1* (47), 6485-6494.

94. Truong, L.; Moody, I. S.; Stankus, D. P.; Nason, J. A.; Lonergan, M. C.; Tanguay, R. L., Differential Stability of Lead Sulfide Nanoparticles Influences Biological Responses in Embryonic Zebrafish. *Archives of Toxicology* **2011**, *85* (7), 787-798.
95. Wiecinski, P. N.; Metz, K. M.; Heiden, T. C. K.; Louis, K. M.; Mangham, A. N.; Hamers, R. J.; Heideman, W.; Peterson, R. E.; Pedersen, J. A., Toxicity of Oxidatively Degraded Quantum Dots to Developing Zebrafish (*Danio rerio*). *Environmental Science & Technology* **2013**, *47* (16), 9132-9139.
96. Chen, N.; He, Y.; Su, Y. Y.; Li, X. M.; Huang, Q.; Wang, H. F.; Zhang, X. Z.; Tai, R. Z.; Fan, C. H., The Cytotoxicity of Cadmium-based Quantum Dots. *Biomaterials* **2012**, *33* (5), 1238-1244.
97. Liu, J. W.; Erogbogbo, F.; Yong, K. T.; Ye, L.; Liu, J.; Hu, R.; Chen, H. Y.; Hu, Y. Z.; Yang, Y.; Yang, J. H.; Roy, I.; Karker, N. A.; Swihart, M. T.; Prasad, P. N., Assessing Clinical Prospects of Silicon Quantum Dots: Studies in Mice and Monkeys. *ACS Nano* **2013**, *7* (8), 7303-7310.
98. Dutta, M.; Thirugnanam, L.; Van Trinh, P.; Fukata, N., High Efficiency Hybrid Solar Cells Using Nanocrystalline Si Quantum Dots and Si Nanowires. *ACS Nano* **2015**, *9* (7), 6891-6899.
99. Kim, S.; Jeon, K.; Lee, J. C.; Swihart, M. T.; Yang, M., Enhanced Performance of a Polymer Solar Cell upon Addition of Free-Standing, Freshly Etched, Photoluminescent Silicon Nanocrystals. *Applied Physics Express* **2012**, *5* (2).
100. Liu, C. Y.; Holman, Z. C.; Kortshagen, U. R., Hybrid Solar Cells from P3HT and Silicon Nanocrystals. *Nano Letters* **2009**, *9* (1), 449-452.
101. Liu, C. Y.; Kortshagen, U. R., Hybrid solar cells from MDMO-PPV and silicon nanocrystals. *Nanoscale* **2012**, *4* (13), 3963-3968.
102. Erogbogbo, F.; Yong, K. T.; Roy, I.; Xu, G. X.; Prasad, P. N.; Swihart, M. T., Biocompatible luminescent silicon quantum dots for imaging of cancer cells. *ACS Nano* **2008**, *2* (5), 873-878.
103. Mangolini, L.; David, J.; Rogojina, E.; Kortshagen, U. In Plasma Synthesis and Surface Passivation of Silicon Quantum Dots with Photoluminescence Quantum Yields higher than 60%, *MRS Spring Meeting*, 2006.
104. Clark, R. J.; Aghajamali, M.; Gonzalez, C. M.; Hadidi, L.; Islam, M. A.; Javadi, M.; Mobarok, M. H.; Purkait, T. K.; Robidillo, C. J. T.; Sinelnikov, R.; Thiessen, A. N.; Washington, J.; Yu, H. Y.; Veinot, J. G. C., From Hydrogen Silsesquioxane to Functionalized Silicon Nanocrystals. *Chemistry of Materials* **2017**, *29* (1), 80-89.
105. Mastronardi, M. L.; Maier-Flaig, F.; Faulkner, D.; Henderson, E. J.; Kubel, C.; Lemmer, U.; Ozin, G. A., Size-Dependent Absolute Quantum Yields for Size-Separated Colloidally-Stable Silicon Nanocrystals. *Nano Letters* **2012**, *12* (1), 337-342.

106. Miller, J. B.; Van Sickle, A. R.; Anthony, R. J.; Kroll, D. M.; Kortshagen, U. R.; Hobbie, E. K., Ensemble Brightening and Enhanced Quantum Yield in Size-Purified Silicon Nanocrystals. *ACS Nano* **2012**, *6* (8), 7389-7396.
107. Miller, J. B.; Harris, J. M.; Hobbie, E. K., Purifying Colloidal Nanoparticles through Ultracentrifugation with Implications for Interfaces and Materials. *Langmuir* **2014**, *30* (27), 7936-7946.
108. Brown, S. L.; Vogel, D. J.; Miller, J. B.; Inerbaev, T. M.; Anthony, R. J.; Kortshagen, U. R.; Kilin, D. S.; Hobbie, E. K., Enhancing Silicon Nanocrystal Photoluminescence through Temperature and Microstructure. *Journal of Physical Chemistry C* **2016**, *120* (33), 18909-18916.
109. Brown, S. L.; Miller, J. B.; Anthony, R. J.; Kortshagen, U. R.; Kryjevski, A.; Hobbie, E. K., Abrupt Size Partitioning of Multimodal Photoluminescence Relaxation in Monodisperse Silicon Nanocrystals. *ACS Nano* **2017**, *11* (2), 1597-1603.
110. Brown, S. L.; Krishnan, R.; Elbaradei, A.; Sivaguru, J.; Sibi, M. P.; Hobbie, E. K., Origin of Stretched-Exponential Photoluminescence Relaxation in Size-Separated Silicon Nanocrystals. *AIP Advances* **2017**, *7* (5), 11.
111. Dasog, M.; Yang, Z.; Regli, S.; Atkins, T. M.; Faramus, A.; Singh, M. P.; Muthuswamy, E.; Kauzlarich, S. M.; Tilley, R. D.; Veinot, J. G. C., Chemical Insight into the Origin of Red and Blue Photoluminescence Arising from Freestanding Silicon Nanocrystals. *ACS Nano* **2013**, *7* (3), 2676-2685.
112. de Boer, W.; Timmerman, D.; Dohnalova, K.; Yassievich, I. N.; Zhang, H.; Buma, W. J.; Gregorkiewicz, T., Red Spectral Shift and Enhanced Quantum Efficiency in Phonon-Free Photoluminescence from Silicon Nanocrystals. *Nature Nanotechnology* **2010**, *5* (12), 878-884.
113. Dohnalova, K.; Poddubny, A. N.; Prokofiev, A. A.; de Boer, W.; Umesh, C. P.; Paulusse, J. M. J.; Zuilhof, H.; Gregorkiewicz, T., Surface Brightens Up Si Quantum Dots: Direct Bandgap-like Size-Tunable Emission. *Light-Science & Applications* **2013**, *2*, 6.
114. Dohnalova, K.; Gregorkiewicz, T.; Kusova, K., Silicon Quantum Dots: Surface Matters. *Journal of Physics-Condensed Matter* **2014**, *26* (17), 28.
115. Gupta, A.; Wiggers, H., Freestanding Silicon Quantum Dots: Origin of Red and Blue Luminescence. *Nanotechnology* **2011**, *22* (5).
116. Hannah, D. C.; Yang, J. H.; Podsiadlo, P.; Chan, M. K. Y.; Demortiere, A.; Gosztola, D. J.; Prakapenka, V. B.; Schatz, G. C.; Kortshagen, U.; Schaller, R. D., On the Origin of Photoluminescence in Silicon Nanocrystals: Pressure-Dependent Structural and Optical Studies. *Nano Letters* **2012**, *12* (8), 4200-4205.

117. Kislitsyn, D. A.; Kocevski, V.; Mills, J. M.; Chiu, S. K.; Gervasi, C. F.; Taber, B. N.; Rosenfield, A. E.; Eriksson, O.; Rusz, J.; Goforth, A. M.; Nazin, G. V., Mapping of Defects in Individual Silicon Nanocrystals Using Real-Space Spectroscopy. *Journal of Physical Chemistry Letters* **2016**, 7 (6), 1047-1054.
118. Pavesi, L.; Rasit, T., *Silicon Nanocrystals: Fundamentals, Synthesis and Applications* Wiley-VCH: 2010; p 2.
119. Sagar, D. M.; Atkin, J. M.; Palomaki, P. K. B.; Neale, N. R.; Blackburn, J. L.; Johnson, J. C.; Nozik, A. J.; Raschke, M. B.; Beard, M. C., Quantum Confined-Electron Phonon Interaction in Silicon Nanocrystals. *Nano Letters* **2015**, 15 (3), 1511-1516.
120. Sangghaleh, F.; Bruhn, B.; Schmidt, T.; Linnros, J., Exciton Lifetime Measurements on Single Silicon Quantum Dots. *Nanotechnology* **2013**, 24 (22), 5.
121. Sangghaleh, F.; Sychugov, I.; Yang, Z.; Veinot, J. G. C.; Linnros, J., Near-Unity Internal Quantum Efficiency of Luminescent Silicon Nanocrystals with Ligand Passivation. *ACS Nano* **2015**, 9 (7), 7097-7104.
122. Shu, Y. N.; Fales, B. S.; Levine, B. G., Defect-Induced Conical Intersections Promote Nonradiative Recombination. *Nano Letters* **2015**, 15 (9), 6247-6253.
123. Shu, Y. N.; Kortshagen, U. R.; Levine, B. G.; Anthony, R. J., Surface Structure and Silicon Nanocrystal Photoluminescence: The Role of Hypervalent Silyl Groups. *Journal of Physical Chemistry C* **2015**, 119 (47), 26683-26691.
124. Shu, Y. N.; Levine, B. G., First-Principles Study of Nonradiative Recombination in Silicon Nanocrystals: The Role of Surface Silanol. *Journal of Physical Chemistry C* **2016**, 120 (40), 23246-23253.
125. Sykora, M.; Mangolini, L.; Schaller, R. D.; Kortshagen, U.; Jurbergs, D.; Klimov, V. I., Size-Dependent Intrinsic Radiative Decay Rates of Silicon Nanocrystals at Large Confinement Energies. *Physical Review Letters* **2008**, 100 (6), 4.
126. Valenta, J.; Fucikova, A.; Pelant, I.; Kusova, K.; Dohnalova, K.; Aleknavicius, A.; Cibulka, O.; Fojtik, A.; Kada, G., On the Origin of the Fast Photoluminescence Band in Small Silicon Nanoparticles. *New Journal of Physics* **2008**, 10.
127. Van Sickle, A. R.; Miller, J. B.; Moore, C.; Anthony, R. J.; Kortshagen, U. R.; Hobbie, E. K., Temperature Dependent Photoluminescence of Size-Purified Silicon Nanocrystals. *ACS Applied Materials & Interfaces* **2013**, 5 (10), 4233-4238.
128. Zatoryb, G.; Podhorodecki, A.; Misiewicz, J.; Cardin, J.; Gourbilleau, F., On the Nature of the Stretched Exponential Photoluminescence Decay for Silicon Nanocrystals. *Nanoscale Research Letters* **2011**, 6.

129. Murray, C. B.; Kagan, C. R.; Bawendi, M. G., Synthesis and Characterization of Monodisperse Nanocrystals and Close-packed Nanocrystal Assemblies. *Annual Review of Materials Science* **2000**, *30*, 545-610.
130. Jariwala, B. N.; Dewey, O. S.; Stradins, P.; Ciobanu, C. V.; Agarwal, S., In Situ Gas-Phase Hydrosilylation of Plasma-Synthesized Silicon Nanocrystals. *ACS Applied Materials & Interfaces* **2011**, *3* (8), 3033-3041.
131. Mangolini, L.; Thimsen, E.; Kortshagen, U., High-yield Plasma Synthesis of Luminescent Silicon Nanocrystals. *Nano Letters* **2005**, *5* (4), 655-659.
132. Abderrafi, K.; Calzada, R. G.; Gongalsky, M. B.; Suarez, I.; Abarques, R.; Chirvony, V. S.; Timoshenko, V. Y.; Ibanez, R.; Martinez-Pastor, J. P., Silicon Nanocrystals Produced by Nanosecond Laser Ablation in an Organic Liquid. *Journal of Physical Chemistry C* **2011**, *115* (12), 5147-5151.
133. Chewchinda, P.; Hayashi, K.; Ichida, D.; Seo, H.; Uchida, G.; Shiratani, M.; Odawara, O.; Wada, H. In Preparation of Si nanoparticles by laser ablation in liquid and their application as photovoltaic material in quantum dot sensitized solar cell, *26th Symposium on Plasma Sciences for Materials (SPSM)*, Fukuoka, JAPAN, Sep 23-24; 2013.
134. Li, X. G.; He, Y. Q.; Swihart, M. T., Surface Functionalization of Silicon Nanoparticles Produced by Laser-Driven Pyrolysis of Silane Followed by HF-HNO₃ Etching. *Langmuir* **2004**, *20* (11), 4720-4727.
135. Hessel, C. M.; Henderson, E. J.; Veinot, J. G. C., Hydrogen Silsesquioxane: A Molecular Precursor for Nanocrystalline Si-SiO₂ Composites and Freestanding Hydride-Surface-Terminated Silicon Nanoparticles. *Chemistry of Materials* **2006**, *18* (26), 6139-6146.
136. Hessel, C. M.; Reid, D.; Panthani, M. G.; Rasch, M. R.; Goodfellow, B. W.; Wei, J. W.; Fujii, H.; Akhavan, V.; Korgel, B. A., Synthesis of Ligand-Stabilized Silicon Nanocrystals with Size-Dependent Photoluminescence Spanning Visible to Near-Infrared Wavelengths. *Chemistry of Materials* **2012**, *24* (2), 393-401.
137. Wang, J.; Sun, S. Q.; Peng, F.; Cao, L. X.; Sun, L. F., Efficient One-pot Synthesis of Highly Photoluminescent Alkyl-Functionalised Silicon Nanocrystals. *Chemical Communications* **2011**, *47* (17), 4941-4943.
138. Shiohara, A.; Prabakar, S.; Faramus, A.; Hsu, C. Y.; Lai, P. S.; Northcote, P. T.; Tilley, R. D., Sized Controlled Synthesis, Purification, and Cell Studies with Silicon Quantum Dots. *Nanoscale* **2011**, *3* (8), 3364-3370.
139. He, Y.; Zhong, Y. L.; Peng, F.; Wei, X. P.; Su, Y. Y.; Lu, Y. M.; Su, S.; Gu, W.; Liao, L. S.; Lee, S. T., One-Pot Microwave Synthesis of Water-Dispersible, Ultraphoto- and pH-Stable, and Highly Fluorescent Silicon Quantum Dots. *Journal of the American Chemical Society* **2011**, *133* (36), 14192-14195.

140. Liu, Y.; Gibbs, M.; Puthussery, J.; Gaik, S.; Ihly, R.; Hillhouse, H. W.; Law, M., Dependence of Carrier Mobility on Nanocrystal Size and Ligand Length in PbSe Nanocrystal Solids. *Nano Letters* **2010**, *10* (5), 1960-1969.
141. Boles, M. A.; Engel, M.; Talapin, D. V., Self-Assembly of Colloidal Nanocrystals: From Intricate Structures to Functional Materials. *Chemical Reviews* **2016**, *116* (18), 11220-11289.
142. Amin, V. A.; Aruda, K. O.; Lau, B.; Rasmussen, A. M.; Edme, K.; Weiss, E. A., Dependence of the Band Gap of CdSe Quantum Dots on the Surface Coverage and Binding Mode of an Exciton-Delocalizing Ligand, Methylthiophenolate. *Journal of Physical Chemistry C* **2015**, *119* (33), 19423-19429.
143. Fischer, S. A.; Crotty, A. M.; Kilina, S. V.; Ivanov, S. A.; Tretiak, S., Passivating Ligand and Solvent Contributions to the Electronic Properties of Semiconductor Nanocrystals. *Nanoscale* **2012**, *4* (3), 904-914.
144. Mastronardi, M. L.; Hennrich, F.; Henderson, E. J.; Maier-Flaig, F.; Blum, C.; Reichenbach, J.; Lemmer, U.; Kuebel, C.; Wang, D.; Kappes, M. M.; Ozin, G. A., Preparation of Monodisperse Silicon Nanocrystals Using Density Gradient Ultracentrifugation. *Journal of the American Chemical Society* **2011**, *133* (31), 11928-11931.
145. Fagan, J. A.; Becker, M. L.; Chun, J.; Nie, P.; Bauer, B. J.; Simpson, J. R.; Walker, A. R. H.; Hobbie, E. K., Centrifugal Length Separation of Carbon Nanotubes. *Langmuir* **2008**, *24* (24), 13880-13889.
146. Fagan, J. A.; Becker, M. L.; Chun, J.; Hobbie, E. K., Length fractionation of carbon nanotubes using centrifugation. *Advanced Materials* **2008**, *20* (9), 1609.
147. Bai, L.; Ma, X. J.; Liu, J. F.; Sun, X. M.; Zhao, D. Y.; Evans, D. G., Rapid Separation and Purification of Nanoparticles in Organic Density Gradients. *Journal of the American Chemical Society* **2010**, *132* (7), 2333-2337.
148. Tilley, R. D.; Warner, J. H.; Yamamoto, K.; Matsui, I.; Fujimori, H., Micro-Emulsion Synthesis of Monodisperse Surface Stabilized Silicon Nanocrystals. *Chemical Communications* **2005**, (14), 1833-1835.
149. Cheng, X.; Gondosiswanto, R.; Ciampi, S.; Reece, P. J.; Gooding, J. J., One-Pot Synthesis of Colloidal Silicon Quantum Dots and Surface Functionalization via Thiol-ene Click Chemistry. *Chemical Communications* **2012**, *48* (97), 11874-11876.
150. Yasar-Inceoglu, O.; Lopez, T.; Farshihagro, E.; Mangolini, L., Silicon Nanocrystal Production Through Non-Thermal Plasma Synthesis: A Comparative Study between Silicon Tetrachloride and Silane Precursors. *Nanotechnology* **2012**, *23* (25).

151. Yu, Y. X.; Lu, X. T.; Guillaussier, A.; Voggu, V. R.; Pineros, W.; de la Mata, M.; Arbiol, J.; Smilgies, D. M.; Truskett, T. M.; Korgel, B. A., Orientationally Ordered Silicon Nanocrystal Cuboctahedra in Superlattices. *Nano Letters* **2016**, *16* (12), 7814-7821.
152. Warner, J. H.; Hoshino, A.; Yamamoto, K.; Tilley, R. D., Water-Soluble Photoluminescent Silicon Quantum Dots. *Angewandte Chemie-International Edition* **2005**, *44* (29), 4550-4554.
153. Wilcoxon, J. P.; Samara, G. A.; Provencio, P. N., Optical and Electronic Properties of Si Nanoclusters Synthesized in Inverse Micelles. *Physical Review B* **1999**, *60* (4), 2704-2714.
154. Rosso-Vasic, M.; Spruijt, E.; van Lagen, B.; De Cola, L.; Zuilhof, H., Alkyl-Functionalized Oxide-Free Silicon Nanoparticles: Synthesis and Optical Properties. *Small* **2008**, *4* (10), 1835-1841.
155. Anderson, N. C.; Hendricks, M. P.; Choi, J. J.; Owen, J. S., Ligand Exchange and the Stoichiometry of Metal Chalcogenide Nanocrystals: Spectroscopic Observation of Facile Metal-Carboxylate Displacement and Binding. *Journal of the American Chemical Society* **2013**, *135* (49), 18536-18548.
156. Green, M. L. H., A New Approach to the Formal Classification of Covalent Compounds of the Elements. *Journal of Organometallic Chemistry* **1995**, *500* (1-2), 127-148.
157. Dong, A. G.; Ye, X. C.; Chen, J.; Kang, Y. J.; Gordon, T.; Kikkawa, J. M.; Murray, C. B., A Generalized Ligand-Exchange Strategy Enabling Sequential Surface Functionalization of Colloidal Nanocrystals. *Journal of the American Chemical Society* **2011**, *133* (4), 998-1006.
158. Wei, J. J.; Schaeffer, N.; Pileni, M. P., Ag Nanocrystals: 1. Effect of Ligands on Plasmonic Properties. *Journal of Physical Chemistry B* **2014**, *118* (49), 14070-14075.
159. Wei, J. J.; Schaeffer, N.; Albouy, P. A.; Pileni, M. P., Surface Plasmon Resonance Properties of Silver Nanocrystals Differing in Size and Coating Agent Ordered in 3D Supracrystals. *Chemistry of Materials* **2015**, *27* (16), 5614-5621.
160. Luther, J. M.; Law, M.; Song, Q.; Perkins, C. L.; Beard, M. C.; Nozik, A. J., Structural, Optical and Electrical Properties of Self-Assembled Films of PbSe Nanocrystals Treated with 1,2-Ethanedithiol. *ACS Nano* **2008**, *2* (2), 271-280.
161. Law, M.; Luther, J. M.; Song, O.; Hughes, B. K.; Perkins, C. L.; Nozik, A. J., Structural, Optical, and Electrical Properties of PbSe Nanocrystal Solids Treated Thermally or with Simple Amines. *Journal of the American Chemical Society* **2008**, *130* (18), 5974-5985.
162. Koleilat, G. I.; Levina, L.; Shukla, H.; Myrskog, S. H.; Hinds, S.; Pattantyus-Abraham, A. G.; Sargent, E. H., Efficient, Stable Infrared Photovoltaics Based on Solution-Cast Colloidal Quantum Dots. *ACS Nano* **2008**, *2* (5), 833-840.

163. Beard, M. C.; Midgett, A. G.; Law, M.; Semonin, O. E.; Ellingson, R. J.; Nozik, A. J., Variations in the Quantum Efficiency of Multiple Exciton Generation for a Series of Chemically Treated PbSe Nanocrystal Films. *Nano Letters* **2009**, *9* (2), 836-845.
164. Tang, J.; Kemp, K. W.; Hoogland, S.; Jeong, K. S.; Liu, H.; Levina, L.; Furukawa, M.; Wang, X. H.; Debnath, R.; Cha, D. K.; Chou, K. W.; Fischer, A.; Amassian, A.; Asbury, J. B.; Sargent, E. H., Colloidal-Quantum-Dot Photovoltaics using Atomic-Ligand Passivation. *Nature Materials* **2011**, *10* (10), 765-771.
165. Wheeler, L. M.; Neale, N. R.; Chen, T.; Kortshagen, U. R., Hypervalent Surface Interactions for Colloidal Stability and Doping of Silicon Nanocrystals. *Nature Communications* **2013**, *4*.
166. Sun, W.; Qian, C. X.; Mastronardi, M. L.; Wei, M.; Ozin, G. A., Hydrosilylation Kinetics of Silicon Nanocrystals. *Chemical Communications* **2013**, *49* (97), 11361-11363.
167. Hua, F. J.; Swihart, M. T.; Ruckenstein, E., Efficient Surface Grafting of Luminescent Silicon Quantum Dots by Photoinitiated Hydrosilylation. *Langmuir* **2005**, *21* (13), 6054-6062.
168. Miyano, M.; Endo, S.; Takenouchi, H.; Nakamura, S.; Iwabuti, Y.; Shiino, O.; Nakanishi, T.; Hasegawa, Y., Novel Synthesis and Effective Surface Protection of Air-Stable Luminescent Silicon Nanoparticles. *Journal of Physical Chemistry C* **2014**, *118* (34), 19778-19784.
169. Islam, M. A.; Mobarok, M. H.; Sinelnikov, R.; Purkait, T. K.; Veinot, J. G. C., Phosphorus Pentachloride Initiated Functionalization of Silicon Nanocrystals. *Langmuir* **2017**, *33* (35), 8766-8773.
170. Fagan, J.; Becker, M. L.; Chun, J.; Bauer, B. J.; Hobbie, E. K., Length Fractionation of Carbon Nanotubes Using Centrifugation. *Advanced Materials* **2008**, *20*, 1609 - 1613.
171. Jones, R. A. L., *Soft Condensed Matter*. Oxford University Press: Oxford New York, 2003.
172. Frei, M. BioFiles Volume 6, Nubmer 5 - Centrifugation. <http://www.sigmaaldrich.com/technical-documents/articles/biofiles/centrifugation-separations.html#differential>.
173. Hummel, R. E., *Electronic Properties of Materials*. 4th ed.; Springer: New York, 2012.
174. Dirac, P. A. M., Quantum Mechanics of Many-Electron Systems. *Proceedings of the Royal Society of London Series a-Containing Papers of a Mathematical and Physical Character* **1929**, *123* (792), 714-733.
175. Silbey, R. J.; Alberty, R. A.; Bawendi, M. G., *Physical Chemistry*. John Wiley & Sons, Inc.: 2005.

176. Hartree, D. R., The Wave Mechanics of an Atom with a non-Coulomb Central Field Part I Theory and Methods. *Proceedings of the Cambridge Philosophical Society* **1928**, *24*, 89-110.
177. Hartree, D. R., The Wave Mechanics of an Atom with a non-Coulomb Central Field Part II Some Results and Discussion. *Proceedings of the Cambridge Philosophical Society* **1928**, *24*, 111-132.
178. Hartree, D. R., The Wave Mechanics of an Atom with a non-Coulomb central field Part III Term values and Intensities in Series an Optical Spectra. *Proceedings of the Cambridge Philosophical Society* **1928**, *24*, 426-437.
179. Jones, R. O., Density functional theory: Its Origins, Rise to Prominence, and Future. *Reviews of Modern Physics* **2015**, *87* (3), 897-923.
180. Becke, A. D., Perspective: Fifty Years of Density-Functional Theory in Chemical Physics. *Journal of Chemical Physics* **2014**, *140* (18).
181. Burke, K., Perspective on Density Functional Theory. *Journal of Chemical Physics* **2012**, *136* (15), 9.
182. Anikeeva, P. O.; Halpert, J. E.; Bawendi, M. G.; Bulovic, V., Quantum Dot Light-Emitting Devices with Electroluminescence Tunable over the Entire Visible Spectrum. *Nano Letters* **2009**, *9* (7), 2532-2536.
183. Shields, A. J., Semiconductor Quantum Light Sources. *Nature Photonics* **2007**, *1* (4), 215-223.
184. Alivisatos, P., The Use of Nanocrystals in Biological Detection. *Nature Biotechnology* **2004**, *22* (1), 47-52.
185. Elbaradei, A.; Brown, S. L.; Miller, J. B.; May, S.; Hobbie, E. K., Interaction of Polymer-Coated Silicon Nanocrystals with Lipid Bilayers and Surfactant Interfaces. *Physical Review E* **2016**, *94* (4), 9.
186. Brown, S. L.; Miller, J. B.; Anthony, R. J.; Kortshagen, U. R.; Kryjevski, A.; Hobbie, E. K., Abrupt Size Partitioning of Multimodal Photoluminescence Relaxation in Monodisperse Silicon Nanocrystals. *ACS Nano* **2017**.
187. Yang, Z.; De los Reyes, G. B.; Titova, L. V.; Sychugov, I.; Dasog, M.; Linnros, J.; Hegmann, F. A.; Veinot, J. G. C., Evolution of the Ultrafast Photoluminescence of Colloidal Silicon Nanocrystals with Changing Surface Chemistry. *ACS Photonics* **2015**, *2* (5), 595-605.
188. Johnston, D. C., Stretched Exponential Relaxation Arising from a Continuous Sum of Exponential Decays. *Physical Review B* **2006**, *74* (18), 7.

189. Delerue, C.; Allan, G.; Reynaud, C.; Guillois, O.; Ledoux, G.; Huisken, F., Multiexponential Photoluminescence Decay in Indirect-Gap Semiconductor Nanocrystals. *Physical Review B* **2006**, *73* (23).
190. Hapala, P.; Kusova, K.; Pelant, I.; Jelinek, P., Theoretical Analysis of Electronic Band Structure of 2- to 3-nm Si Nanocrystals. *Physical Review B* **2013**, *87* (19).
191. Wen, X. M.; Zhang, P. F.; Smith, T. A.; Anthony, R. J.; Kortshagen, U. R.; Yu, P.; Feng, Y.; Shrestha, S.; Coniber, G.; Huang, S. J., Tunability Limit of Photoluminescence in Colloidal Silicon Nanocrystals. *Scientific Reports* **2015**, *5*, 10.
192. Phillips, J. C., Stretched Exponential Relaxation in Molecular and Electronic Glasses. *Reports on Progress in Physics* **1996**, *59* (9), 1133-1207.
193. Miller, J. B.; Hobbie, E. K., Nanoparticles as Macromolecules. *Journal of Polymer Science Part B-Polymer Physics* **2013**, *51* (16), 1195-1208.
194. Miller, J. B.; Dandu, N.; Velizhanin, K. A.; Anthony, R. J.; Kortshagen, U. R.; Kroll, D. M.; Kilina, S.; Hobbie, E. K., Enhanced Luminescent Stability through Particle Interactions in Silicon Nanocrystal Aggregates. *ACS Nano* **2015**, *9* (10), 9772-9782.
195. Hannah, D. C.; Yang, J. H.; Kramer, N. J.; Schatz, G. C.; Kortshagen, U. R.; Schaller, R. D., Ultrafast Photoluminescence in Quantum-Confined Silicon Nanocrystals Arises from an Amorphous Surface Layer. *ACS Photonics* **2014**, *1* (10), 960-967.
196. Ondic, L.; Kusova, K.; Ziegler, M.; Fekete, L.; Gartnerova, V.; Chab, V.; Holy, V.; Cibulka, O.; Herynkova, K.; Gallart, M.; Gilliot, P.; Honerlage, B.; Pelant, I., A Complex Study of the Fast Blue Luminescence of Oxidized Silicon Nanocrystals: The Role of the Core. *Nanoscale* **2014**, *6* (7), 3837-3845.
197. Macfarlane, R. J.; Lee, B.; Jones, M. R.; Harris, N.; Schatz, G. C.; Mirkin, C. A., Nanoparticle Superlattice Engineering with DNA. *Science* **2011**, *334* (6053), 204-208.
198. Josten, E.; Wetterskog, E.; Glavic, A.; Boesecke, P.; Feoktystov, A.; Brauweiler-Reuters, E.; Rucker, U.; Salazar-Alvarez, G.; Bruckel, T.; Bergstrom, L., Superlattice Growth and Rearrangement during Evaporation-Induced Nanoparticle Self-Assembly. *Scientific Reports* **2017**, *7*.
199. Yadavali, S.; Sachan, R.; Dyck, O.; Kalyanaraman, R., DC Electric Field Induced Phase Array Self-Assembly of Au Nanoparticles. *Nanotechnology* **2014**, *25* (46), 9.
200. Elbert, K. C.; Jishkariani, D.; Wu, Y. T.; Lee, J. D.; Donnio, B.; Murray, C. B., Design, Self-Assembly, and Switchable Wettability in Hydrophobic, Hydrophilic, and Janus Dendritic Ligand-Gold Nanoparticle Hybrid Materials. *Chemistry of Materials* **2017**, *29* (20), 8737-8746.

201. Dong, A. G.; Chen, J.; Vora, P. M.; Kikkawa, J. M.; Murray, C. B., Binary Nanocrystal Superlattice Membranes Self-Assembled at the Liquid-Air Interface. *Nature* **2010**, *466* (7305), 474-477.
202. Kim, S. H.; Lee, S. Y.; Yang, S. M.; Yi, G. R., Self-Assembled Colloidal Structures for Photonics. *NPG Asia Materials* **2011**, *3* (1), 25-33.
203. Greybush, N. J.; Liberal, I.; Malassis, L.; Kikkawa, J. M.; Engheta, N.; Murray, C. B.; Kagan, C. R., Plasmon Resonances in Self-Assembled Two-Dimensional Au Nanocrystal Metamolecules. *ACS Nano* **2017**, *11* (3), 2917-2927.
204. Kasha, M., Characterization of Electronic Transitions in Complex Molecules. *Discussions of the Faraday Society* **1950**, (9), 14-19.
205. Vogel, D. J.; Kilin, D. S., First-Principles Treatment of Photoluminescence in Semiconductors. *Journal of Physical Chemistry C* **2015**, *119* (50), 27954-27964.
206. Murray, C. B.; Kagan, C. R.; Bawendi, M. G., Self-Organization of CdSe Nanocrystallites into 3-Dimensional Quantum Dot Superlattices. *Science* **1995**, *270* (5240), 1335-1338.
207. Bodnarchuk, M. I.; Kovalenko, M. V.; Heiss, W.; Talapin, D. V., Energetic and Entropic Contributions to Self-Assembly of Binary Nanocrystal Superlattices: Temperature as the Structure-Directing Factor. *Journal of the American Chemical Society* **2010**, *132* (34), 11967-11977.
208. Aleksandrovic, V.; Greshnykh, D.; Randjelovic, I.; Fromsdorf, A.; Kornowski, A.; Roth, S. V.; Klinke, C.; Weller, H., Preparation and Electrical Properties of Cobalt-Platinum Nanoparticle Monolayers Deposited by the Langmuir-Blodgett technique. *ACS Nano* **2008**, *2* (6), 1123-1130.
209. Kleinert, J.; Kim, S.; Velev, O. D., Electric-Field-Assisted Convective Assembly of Colloidal Crystal Coatings. *Langmuir* **2010**, *26* (12), 10380-10385.
210. Sapoletova, N. A.; Martynova, N. A.; Napolskii, K. S.; Eliseev, A. A.; Lukashin, A. V.; Kolesnik, I. V.; Petukhov, D. I.; Kushnir, S. E.; Vassilieva, A. V.; Grigoriev, S. V.; Grigoryeva, N. A.; Mistonov, A. A.; Byelov, D. V.; Tret'yakov, Y. D., Electric-Field-Assisted Self-Assembly of Colloidal Particles. *Physics of the Solid State* **2011**, *53* (6), 1126-1130.
211. Radha, B.; Senesi, A. J.; O'Brien, M. N.; Wang, M. X.; Auyeung, E.; Lee, B.; Mirkin, C. A., Reconstitutable Nanoparticle Superlattices. *Nano Letters* **2014**, *14* (4), 2162-2167.
212. Talapin, D. V.; Shevchenko, E. V.; Kornowski, A.; Gaponik, N.; Haase, M.; Rogach, A. L.; Weller, H., A New Approach to Crystallization of CdSe Nanoparticles into Ordered Three-Dimensional Superlattices. *Advanced Materials* **2001**, *13* (24), 1868.

213. Alzaid, M.; Roth, J.; Wang, Y. Z.; Almutairi, E.; Brown, S. L.; Dumitrica, T.; Hobbie, E. K., Enhancing the Elasticity of Ultrathin Single-Wall Carbon Nanotube Films with Colloidal Nanocrystals. *Langmuir* **2017**, *33* (32), 7889-7895.
214. Sachan, M.; Walrath, N. D.; Majetich, S. A.; Krycka, K.; Kao, C. C., Interaction Effects within Langmuir Layers and Three-Dimensional Arrays of Epsilon-Co Nanoparticles. *Journal of Applied Physics* **2006**, *99* (8), 3.
215. Paik, T.; Diroll, B. T.; Kagan, C. R.; Murray, C. B., Binary and Ternary Superlattices Self-Assembled from Colloidal Nanodisks and Nanorods. *Journal of the American Chemical Society* **2015**, *137* (20), 6662-6669.
216. Kagan, C. R.; Lifshitz, E.; Sargent, E. H.; Talapin, D. V., Building Devices From Colloidal Quantum Dots. *Science* **2016**, *353* (6302).
217. Choi, J. H.; Wang, H.; Oh, S. J.; Paik, T.; Jo, P. S.; Sung, J.; Ye, X. C.; Zhao, T. S.; Diroll, B. T.; Murray, C. B.; Kagan, C. R., Exploiting the Colloidal Nanocrystal Library to Construct Electronic Devices. *Science* **2016**, *352* (6282), 205-208.
218. Ip, A. H.; Thon, S. M.; Hoogland, S.; Voznyy, O.; Zhitomirsky, D.; Debnath, R.; Levina, L.; Rollny, L. R.; Carey, G. H.; Fischer, A.; Kemp, K. W.; Kramer, I. J.; Ning, Z. J.; Labelle, A. J.; Chou, K. W.; Amassian, A.; Sargent, E. H., Hybrid Passivated Colloidal Quantum Dot Solids. *Nature Nanotechnology* **2012**, *7* (9), 577-582.
219. Scheeler, S. P.; Muhlig, S.; Rockstuhl, C.; Bin Hasan, S.; Ullrich, S.; Neubrech, F.; Kudera, S.; Pacholski, C., Plasmon Coupling in Self-Assembled Gold Nanoparticle-Based Honeycomb Islands. *Journal of Physical Chemistry C* **2013**, *117* (36), 18634-18641.
220. Barrow, S. J.; Wei, X. Z.; Baldauf, J. S.; Funston, A. M.; Mulvaney, P., The Surface Plasmon Modes of Self-Assembled Gold Nanocrystals. *Nature Communications* **2012**, *3*.
221. Sugaya, T.; Amano, T.; Mori, M.; Niki, S., Miniband Formation in InGaAs Quantum Dot Superlattice. *Applied Physics Letters* **2010**, *97* (4).
222. Kada, T.; Asahi, S.; Kaizu, T.; Harada, Y.; Tamaki, R.; Okada, Y.; Kita, T., Efficient Two-Step Photocarrier Generation in Bias-Controlled InAs/GaAs Quantum Dot Superlattice Intermediate-Band Solar Cells. *Scientific Reports* **2017**, *7*.
223. Yu, Y. X.; Bosoy, C. A.; Smilgies, D. M.; Korgel, B. A., Self-Assembly and Thermal Stability of Binary Superlattices of Gold and Silicon Nanocrystals. *Journal of Physical Chemistry Letters* **2013**, *4* (21), 3677-3682.
224. Yu, Y. X.; Bosoy, C. A.; Hessel, C. M.; Smilgies, D. M.; Korgel, B. A., Silicon Nanocrystal Superlattices. *ChemPhysChem* **2013**, *14* (1), 84-87.
225. Hiramatsu, H.; Osterloh, F. E., A Simple Large-Scale Synthesis of Nearly Monodisperse Gold and Silver Nanoparticles with Adjustable Sizes and with Exchangeable Surfactants. *Chemistry of Materials* **2004**, *16* (13), 2509-2511.

226. Auer, S.; Frenkel, D., Suppression of Crystal Nucleation in Polydisperse Colloids Due to Increase of the Surface Free Energy. *Nature* **2001**, *413* (6857), 711-713.
227. Leunissen, M. E.; Christova, C. G.; Hynninen, A. P.; Royall, C. P.; Campbell, A. I.; Imhof, A.; Dijkstra, M.; van Roij, R.; van Blaaderen, A., Ionic Colloidal Crystals of Oppositely Charged Particles. *Nature* **2005**, *437* (7056), 235-240.
228. Bishop, K. J. M.; Wilmer, C. E.; Soh, S.; Grzybowski, B. A., Nanoscale Forces and Their Uses in Self-Assembly. *Small* **2009**, *5* (14), 1600-1630.
229. Min, Y. J.; Akbulut, M.; Kristiansen, K.; Golan, Y.; Israelachvili, J., The Role of Interparticle and External Forces in Nanoparticle Assembly. *Nature Materials* **2008**, *7* (7), 527-538.
230. Hynninen, A. P.; Christova, C. G.; van Roij, R.; van Blaaderen, A.; Dijkstra, M., Prediction and Observation of Crystal Structures of Oppositely Charged Colloids. *Physical Review Letters* **2006**, *96* (13), 4.
231. Bartlett, P.; Campbell, A. I., Three-dimensional binary superlattices of oppositely charged colloids. *Physical Review Letters* **2005**, *95* (12), 4.
232. Bartlett, P.; Ottewill, R. H.; Pusey, P. N., Superlattice Formation in Binary-Mixtures of Hard-Sphere Colloids. *Physical Review Letters* **1992**, *68* (25), 3801-3804.
233. Eldridge, M. D.; Madden, P. A.; Frenkel, D., Entropy-Driven Formation of a Superlattice in A Hard-Sphere Binary Mixture. *Nature* **1993**, *365* (6441), 35-37.
234. Cottin, X.; Monson, P. A., Substitutionally Ordered Solid-Solutions of Hard-Spheres. *Journal of Chemical Physics* **1995**, *102* (8), 3354-3360.
235. Orejon, D.; Sefiane, K.; Shanahan, M. E. R., Stick-Slip of Evaporating Droplets: Substrate Hydrophobicity and Nanoparticle Concentration. *Langmuir* **2011**, *27* (21), 12834-12843.
236. Balasubramanian, K. K.; Cammarata, V.; Wu, Q., Langmuir-Schaefer Films - Head Group Influence on Orientation of Substituted Styryl Bipyridines. *Langmuir* **1995**, *11* (5), 1658-1665.
237. Lambert, K.; Capek, R. K.; Bodnarchuk, M. I.; Kovalenko, M. V.; Van Thourhout, D.; Heiss, W.; Hens, Z., Langmuir-Schaefer Deposition of Quantum Dot Multilayers. *Langmuir* **2010**, *26* (11), 7732-7736.
238. Mogensen, K. B.; Kneipp, K., Size-Dependent Shifts of Plasmon Resonance in Silver Nanoparticle Films Using Controlled Dissolution: Monitoring the Onset of Surface Screening Effects. *Journal of Physical Chemistry C* **2014**, *118* (48), 28075-28083.
239. Peng, S.; McMahon, J. M.; Schatz, G. C.; Gray, S. K.; Sun, Y. G., Reversing the Size-Dependence of Surface Plasmon Resonances. *Proceedings of the National Academy of Sciences of the United States of America* **2010**, *107* (33), 14530-14534.

240. Ansar, S. M.; Mohammed, F. S.; von White, G.; Budi, M.; Powell, K. C.; Mefford, O. T.; Kitchens, C. L., Effect of Postsynthesis Purifications on Gold and Silver Nanoparticle Ligand Coverage. *Journal of Physical Chemistry C* **2016**, *120* (12), 6842-6850.
241. Miller, J. B.; Usselman, A. C. P.; Anthony, R. J.; Kortshagen, U. R.; Wagner, A. J.; Denton, A. R.; Hobbie, E. K., Phase Separation and the 'Coffee-Ring' Effect in Polymer-Nanocrystal Mixtures. *Soft Matter* **2014**, *10* (11), 1665-1675.
242. Majumder, M.; Rendall, C. S.; Eukel, J. A.; Wang, J. Y. L.; Behabtu, N.; Pint, C. L.; Liu, T. Y.; Orbaek, A. W.; Mirri, F.; Nam, J.; Barron, A. R.; Hauge, R. H.; Schmid, H. K.; Pasquali, M., Overcoming the "Coffee-Stain" Effect by Compositional Marangoni-Flow-Assisted Drop-Drying. *Journal of Physical Chemistry B* **2012**, *116* (22), 6536-6542.
243. Bhardwaj, R.; Fang, X. H.; Somasundaran, P.; Attinger, D., Self-Assembly of Colloidal Particles from Evaporating Droplets: Role of DLVO Interactions and Proposition of a Phase Diagram. *Langmuir* **2010**, *26* (11), 7833-7842.
244. Moffat, J. R.; Sefiane, K.; Shanahan, M. E. R., Effect of TiO₂ Nanoparticles on Contact Line Stick-Slip Behavior of Volatile Drops. *Journal of Physical Chemistry B* **2009**, *113* (26), 8860-8866.
245. Nguyen, T. A. H.; Hampton, M. A.; Nguyen, A. V., Evaporation of Nanoparticle Droplets on Smooth Hydrophobic Surfaces: The Inner Coffee Ring Deposits. *Journal of Physical Chemistry C* **2013**, *117* (9), 4707-4716.
246. Wang, L. M.; McCarthy, T. J., Covalently Attached Liquids: Instant Omniphobic Surfaces with Unprecedented Repellency. *Angewandte Chemie-International Edition* **2016**, *55* (1), 244-248.
247. Shanahan, M. E. R., Simple Theory of Stick-Slip Wetting Hysteresis. *Langmuir* **1995**, *11* (3), 1041-1043.
248. Erbil, H. Y.; McHale, G.; Newton, M. I., Drop Evaporation on Solid Surfaces: Constant Contact Angle Mode. *Langmuir* **2002**, *18* (7), 2636-2641.
249. Baranov, D.; Fiore, A.; van Huis, M.; Giannini, C.; Falqui, A.; Lafont, U.; Zandbergen, H.; Zanella, M.; Cingolani, R.; Manna, L., Assembly of Colloidal Semiconductor Nanorods in Solution by Depletion Attraction. *Nano Letters* **2010**, *10* (2), 743-749.
250. Zanella, M.; Bertoni, G.; Franchini, I. R.; Brescia, R.; Baranov, D.; Manna, L., Assembly of Shape-Controlled Nanocrystals by Depletion Attraction. *Chemical Communications* **2011**, *47* (1), 203-205.
251. Henzie, J.; Grunwald, M.; Widmer-Cooper, A.; Geissler, P. L.; Yang, P. D., Self-Assembly of Uniform Polyhedral Silver Nanocrystals into Densest Packings and Exotic Superlattices. *Nature Materials* **2012**, *11* (2), 131-137.

252. Zou, S. L.; Janel, N.; Schatz, G. C., Silver Nanoparticle Array Structures that Produce Remarkably Narrow Plasmon Lineshapes. *Journal of Chemical Physics* **2004**, *120* (23), 10871-10875.
253. Guerra, R. E.; Kelleher, C. P.; Hollingsworth, A. D.; Chaikin, P. M., Freezing on a Sphere. *Nature* **2018**, *554* (7692), 346-350.
254. Ryu, D. S.; Inoue, T.; Osaki, K., A Birefringence Study of Polymer Crystallization in the Process of Elongation of Films. *Polymer* **1998**, *39* (12), 2515-2520.
255. Marentette, J. M.; Brown, G. R., Polymer Spherulites: 1. Birefringence and Morphology. *Journal of Chemical Education* **1993**, *70* (6), 435-439.
256. Park, J.; An, K. J.; Hwang, Y. S.; Park, J. G.; Noh, H. J.; Kim, J. Y.; Park, J. H.; Hwang, N. M.; Hyeon, T., Ultra-Large-Scale Syntheses of Monodisperse Nanocrystals. *Nature Materials* **2004**, *3* (12), 891-895.
257. Sun, Y. G.; Xia, Y. N., Shape-Controlled Synthesis of Gold and Silver Nanoparticles. *Science* **2002**, *298* (5601), 2176-2179.
258. Stoeva, S.; Klabunde, K. J.; Sorensen, C. M.; Dragieva, I., Gram-Scale Synthesis of Monodisperse Gold Colloids by the Solvated Metal Atom Dispersion Method and Digestive Ripening and their organization into Two- and Three-Dimensional Structures. *Journal of the American Chemical Society* **2002**, *124* (10), 2305-2311.
259. Prasad, B. L. V.; Stoeva, S. I.; Sorensen, C. M.; Klabunde, K. J., Digestive Ripening of Thiolated Gold Nanoparticles: The Effect of Alkyl Chain Length. *Langmuir* **2002**, *18* (20), 7515-7520.
260. Shimpi, J. R.; Sidhaye, D. S.; Prasad, B. L. V., Digestive Ripening: A Fine Chemical Machining Process on the Nanoscale. *Langmuir* **2017**, *33* (38), 9491-9507.
261. Nozik, A. J., Quantum Dot Solar Cells. *Physica E-Low-Dimensional Systems & Nanostructures* **2002**, *14* (1-2), 115-120.
262. Stohs, S. J.; Bagchi, D., Oxidative Mechanisms in the Toxicity of Metal-Ions. *Free Radical Biology and Medicine* **1995**, *18* (2), 321-336.
263. Derfus, A. M.; Chan, W. C. W.; Bhatia, S. N., Probing the cytotoxicity of semiconductor quantum dots. *Nano Letters* **2004**, *4* (1), 11-18.
264. Valko, M.; Morris, H.; Cronin, M. T. D., Metals, Toxicity and Oxidative Stress. *Current Medicinal Chemistry* **2005**, *12* (10), 1161-1208.
265. Gidlow, D. A., Lead toxicity. *Occupational Medicine-Oxford* **2004**, *54* (2), 76-81.

266. Papanikolaou, N. C.; Hatzidaki, E. G.; Belivanis, S.; Tzanakakis, G. N.; Tsatsakis, A. M., Lead Toxicity Update. A Brief Review. *Medical Science Monitor* **2005**, *11* (10), RA329-RA336.
267. Jiang, W.; Kim, B. Y. S.; Rutka, J. T.; Chan, W. C. W., Nanoparticle-Mediated Cellular Response is Size-Dependent. *Nature Nanotechnology* **2008**, *3* (3), 145-150.
268. Colvin, V. L., The Potential Environmental Impact of Engineered Nanomaterials. *Nature Biotechnology* **2003**, *21* (10), 1166-1170.
269. Yu, J.; Patel, S. A.; Dickson, R. M., In vitro and Intracellular Production of Peptide-Encapsulated Fluorescent Silver Nanoclusters. *Angewandte Chemie-International Edition* **2007**, *46* (12), 2028-2030.
270. Richards, C. I.; Choi, S.; Hsiang, J. C.; Antoku, Y.; Vosch, T.; Bongiorno, A.; Tzeng, Y. L.; Dickson, R. M., Oligonucleotide-Stabilized Ag Nanocluster Fluorophores. *Journal of the American Chemical Society* **2008**, *130* (15), 5038-+.
271. Crooks, R. M.; Lemon, B. I.; Sun, L.; Yeung, L. K.; Zhao, M. Q., Dendrimer-Encapsulated Metals and Semiconductors: Synthesis, Characterization, and Applications. *Dendrimers III: Design, Dimension, Function* **2001**, *212*, 81-135.
272. Yu, J. H.; Choi, S. M.; Richards, C. I.; Antoku, Y.; Dickson, R. M., Live Cell Surface Labeling with Fluorescent Ag Nanocluster Conjugates. *Photochemistry and Photobiology* **2008**, *84* (6), 1435-1439.
273. Diez, I.; Pusa, M.; Kulmala, S.; Jiang, H.; Walther, A.; Goldmann, A. S.; Muller, A. H. E.; Ikkala, O.; Ras, R. H. A., Color Tunability and Electrochemiluminescence of Silver Nanoclusters. *Angewandte Chemie-International Edition* **2009**, *48* (12), 2122-2125.
274. Diez, I.; Jiang, H.; Ras, R. H. A., Enhanced Emission of Silver Nanoclusters Through Quantitative Phase Transfer. *Chemphyschem* **2010**, *11* (14), 3100-3104.
275. Walter, M.; Akola, J.; Lopez-Acevedo, O.; Jadzinsky, P. D.; Calero, G.; Ackerson, C. J.; Whetten, R. L.; Gronbeck, H.; Hakkinen, H., A Unified View of Ligand-Protected Gold Clusters as Superatom Complexes. *Proceedings of the National Academy of Sciences of the United States of America* **2008**, *105* (27), 9157-9162.
276. Kohn, W.; Sham, L. J., Self-Consistent Equations Including Exchange and Correlation Effects. *Physical Review* **1965**, *140* (4A), A1133-A1138.
277. Kaduk, B.; Kowalczyk, T.; Van Voorhis, T., Constrained Density Functional Theory. *Chem. Rev.* **2012**, *112* (1), 321-370.
278. Yao, G.; Berry, M. T.; May, P. S.; Kilin, D., DFT Calculation of Russell–Saunders Splitting for Lanthanide Ions Doped in Hexagonal (β)-NaYF₄ Nanocrystals. *The Journal of Physical Chemistry C* **2013**, *117* (33), 17177-17185.

279. Parr, R. G.; Yang, W., Density-Functional Theory of Atoms and Molecules. *Oxford University Press*: 1994.
280. Vogel, D. J.; Kryjevski, A.; Inerbaev, T. M.; Kilin, D. S., Photoinduced Single- and Multiple- Electron Dynamics Processes Enhanced by Quantum Confinement in Lead Halide Perovskite Quantum Dots. *The Journal of Physical Chemistry Letters* **2017**.
281. Hammes-Schiffer, S.; Tully, J. C., Proton Transfer in Solution -- Molecular Dynamics with Quantum Transitions. *J. Chem. Phys.* **1994**, *101* (6), 4657-4667.
282. Redfield, A. G., On the Theory of Relaxation Processes. *IBM Journal of Research and Development* **1957**, *1* (1), 19-31.
283. Bae, G. T.; Aikens, C. M., Time-Dependent Density Functional Theory Studies of Optical Properties of Ag Nanoparticles: Octahedra, Truncated Octahedra, and Icosahedra. *Journal of Physical Chemistry C* **2012**, *116* (18), 10356-10367.
284. Shafai, G.; Hong, S. Y.; Bertino, M.; Rahman, T. S., Effect of Ligands on the Geometric and Electronic Structure of Au-13 Clusters. *Journal of Physical Chemistry C* **2009**, *113* (28), 12072-12078.
285. Furche, F.; Ahlrichs, R.; Weis, P.; Jacob, C.; Gilb, S.; Bierweiler, T.; Kappes, M. M., The Structures of Small Gold Cluster Anions as Determined by a Combination of Ion Mobility Measurements and Density Functional Calculations. *Journal of Chemical Physics* **2002**, *117* (15), 6982-6990.
286. Meng, Q. G.; May, P. S.; Berry, M. T.; Kilin, D., Sequential Hydrogen Dissociation from a Charged Pt₁₃H₂₄ Cluster Modeled by Ab Initio Molecular Dynamics. *International Journal of Quantum Chem.* **2012**, *112* (24), 3896-3903.
287. Blochl, P. E., Projector Augmented-Wave Method. *Physical Review B* **1994**, *50* (24), 17953-17979.
288. Kresse, G.; Joubert, D., From Ultrasoft Pseudopotentials to the Projector Augmented-Wave Method. *Physical Review B* **1999**, *59* (3), 1758-1775.
289. Perdew, J. P.; Burke, K.; Ernzerhof, M., Generalized Gradient Approximation Made Simple. *Physical Review Letters* **1996**, *77* (18), 3865-3868.
290. Kohn, W.; Sham, L. J., Self-Consistent Equations Including Exchange and Correlation Effects. *Physical Review* **1965**, *140* (4A), 1133.
291. Heyd, J.; Scuseria, G. E.; Ernzerhof, M., Hybrid Functionals Based on a Screened Coulomb Potential. *Journal of Chemical Physics* **2003**, *118* (18), 8207-8215.
292. Becke, A. D., Density-Functional Thermochemistry. III. The Role of Exact Exchange. *Journal of Chemical Physics* **1993**, *98*, 5648-5652.

293. Lee, C. T.; Yang, W. T.; Parr, R. G., Development of the Colle-Salvetti Correlation-Energy Formula into a Functional of the Electron-Density. *Physical Review B* **1988**, *37* (2), 785-789.
294. Meng, Q. G.; May, P. S.; Berry, M. T.; Kilin, D., Sequential Hydrogen Dissociation from a Charged Pt₁₃H₂₄ Cluster Modeled by Ab Initio Molecular Dynamics. *International Journal of Quantum Chemistry* **2012**, *112* (24), 3896-3903.
295. Kilin, D. S.; Micha, D. A., Relaxation of Photoexcited Electrons at a Nanostructured Si(111) Surface. *Journal of Physical Chemistry Letters* **2010**, *1* (7), 1073-1077.
296. Englman, R.; Jortner, J., The Energy Gap Law for Radiationless Transitions in Large Molecules. *Molecular Physics* **1970**, *18* (2), 154-164.
297. Van Rysselberghe, P., Remarks Concerning the Clausius-Mossotti Law. *Journal of Physical Chemistry* **1932**, *36* (4), 1152-1155.
298. Ball, P., A New Kind of Alchemy. *New Scientist* **2005**, *186* (2495), 30-33.
299. Knight, W. D.; Clemenger, K.; Deheer, W. A.; Saunders, W. A.; Chou, M. Y.; Cohen, M. L., Electronic Shell Structure and Abundances of Sodium Clusters. *Physical Review Letters* **1984**, *52* (24), 2141-2143.

APPENDIX A. EQUIPMENT

The purpose of this appendix is to give details on the main pieces of equipment used within this report. The complexity of many of these instruments is too great to give every detail, yet it is within the scope of this appendix to highlight the instruments main applications and how they can be used efficiently.

A1. Upright Microscope

The upright microscope is a versatile instrument that can be used to take a sample's spot dependent PL, absorption, lifetime, and image while the stage can be easily equipped with a thermal stage to probe a sample's temperature response as well. **Figure A1** shows a basic diagram of the excitation source's path and how it travels through the microscope. The filters, objective, stage height and position of the top mirror (inline or outline) are used for various measurements.

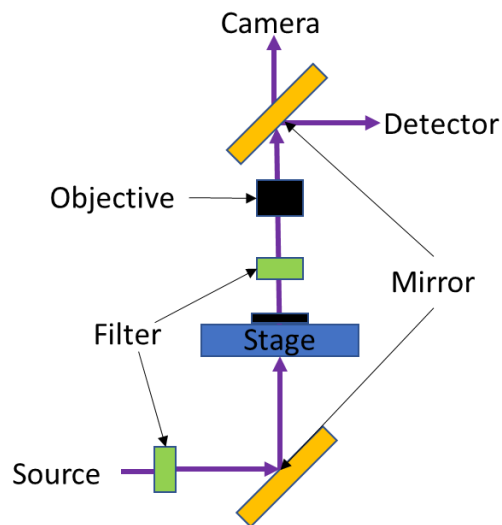


Figure A1. Typical light path for the upright microscope.

The numbers in **Figure A2** correspond to the spatial location on the upright microscope of each switch, nob or lever that can be used to change the filters, objective, stage height and position

of the top mirror. Going in numerical order, the following list details each part's operation and function.

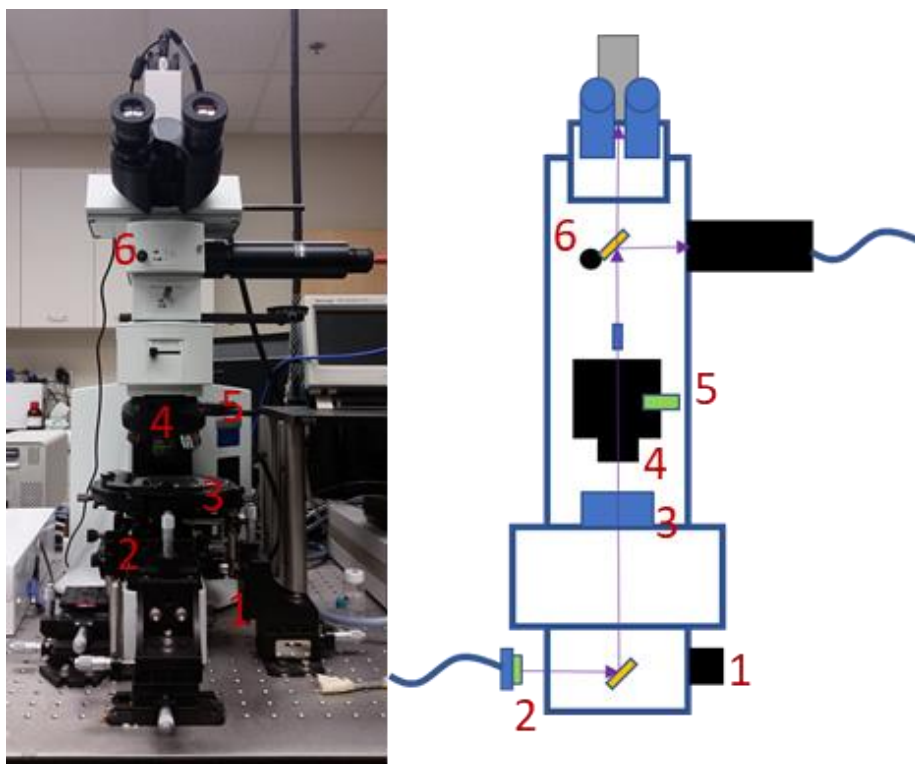


Figure A2. The various controls that can be changed for each measurement: (1) Fine and Course Focus, (2) Pre-sample filter, typically a notch or band pass filter, (3) Sample stage, (4) Objective, (5) Post sample filter, typically a long pass filter, (6) Pull used to direct signal to the camera or detector.

- 1.) Knob on the lower right side of the scope is used to adjust the coarse and fine focus.
- 2.) The first filter is used to manipulate the excitation source (typically a notch or neutral density filter).
- 3.) The stage can be changed from a standard to a thermal stage.
- 4.) The objective can be changed with magnifications ranging from 4x to 100x.
- 5.) The downstream filter is placed in the tray and then inserted on the front right side of the scope right above the turret. Typically, a 405 nm or 500 nm long pass filter is used to block

the excitation source. Note: the arrow on the side of the filter should be pointing toward the excitation source.

- 6.) The top pull is used to place the top mirror in or out of the light path. When pushed in, the mirror will direct the signal to the detector (spectrometer or photomultiplier tube) and when pulled out it will direct the signal to the camera.

A2. Inverted Microscope

Like the upright microscope, the inverted microscope is a versatile tool that can be used to take spot dependent PL, lifetime, and transmission data while it can also take images with a standard or a high-resolution camera. Because of the inverted microscope's EPI-illumination configuration, only reflected or fluorescent light will reach the detector. The source light first travels to a dichroic mirror where the light is directed through the objective and to the sample. Fluorescence or reflection from the sample then travels back through the objective, past the dichroic, and to the detector. With this microscope, the main things that can be changed are the filters, detector, source, and objective. The following numerical list gives a description of each control and operation. Also note that the numbers of this list correspond to the numbers in **Figure A4**.

- 1.) Knob on the lower front right side is used to control the fine and coarse focus.
- 2.) The bottom knob on the lower front side is used to control the microscopes internal light source. Note that the square button on the left of the knob must be pressed to turn on the light before the intensity can be controlled.
- 3.) The switch is used to direct the signal to the camera or the detector.

4.) There are several parts that can be manipulated in close vicinity of 4. They are the a. turret, b. objective, c. filters and dichroic lens housing, d. downstream filter, and e. switch to let source light in from the back or side of the scope.

- a. The turret is used to easily switch between various objectives.
- b. The objectives are screwed into the turret and can be used to magnify the sample from 4x to 100x. Note that because of the inverted set up a water or oil immersion objective can be used, which is typically better for spectral detection.
- c. Underneath of the turret is the filter and dichroic housing. To change the filters and dichroic lenses a small hex key must be used to loosen a small internal bolt on the right side of the scope as seen in **Figure A3**.

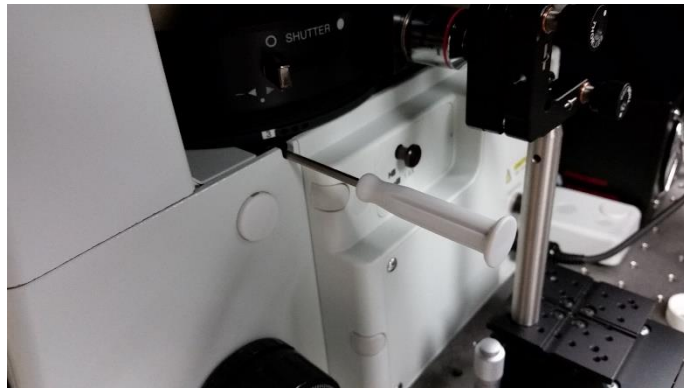


Figure A3. Hex wrench and hidden hex bolt used to loosen the filter and dichroic lens housing.

- d. A filter such as a long pass can be placed in a black tray and positioned in the beam path.
 - e. A switch at the base of the dichroic housing that can be moved forward or backward to change whether light enters from the back or side port.
- 5.) A filter upstream of the sample can be placed to manipulate the excitation source, typically a notch filter is used.

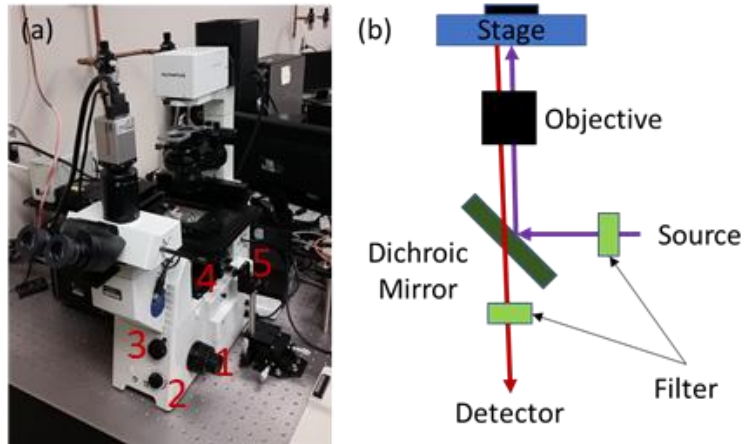


Figure A4. (a) The upright microscope with numbers highlighting the various controls mentioned in the text. (b) The source and signal path for the upright microscope

A3. Ultracentrifuge

An ultracentrifuge is used to separate particles of different densities or sizes from each other. The centrifuge is basic to use but due to the high speeds of the rotor, it will be important to make sure it is properly balanced. In terms of controls, a digital touch screen is used to dictate rotor speed, spin duration, temperature, and acceleration/deceleration rate. More details on this are given for a specific spin in **Appendix B5**. Note that the on and off switch is located on the right side.



Figure A5. Ultracentrifuge with rotor.

A4. 3D Printers

3D printers are very valuable assets in research and can greatly enhance the speed of experimental setup. **Figure A6** shows several examples of various 3D printed parts that were used to conduct the research contained within this report. In this report only fused deposition modeling (FDM) printers were used such as the Makerbot® printer. FDM printers do not have the resolution of a stereolithography (SLA) printer but are considerably more economical. In terms of computer modeling software, the free version of Sketchup® is economical and fully capable of designing basic parts. With the .stl extension, one can easily export a model to be printed at a local printing hub.

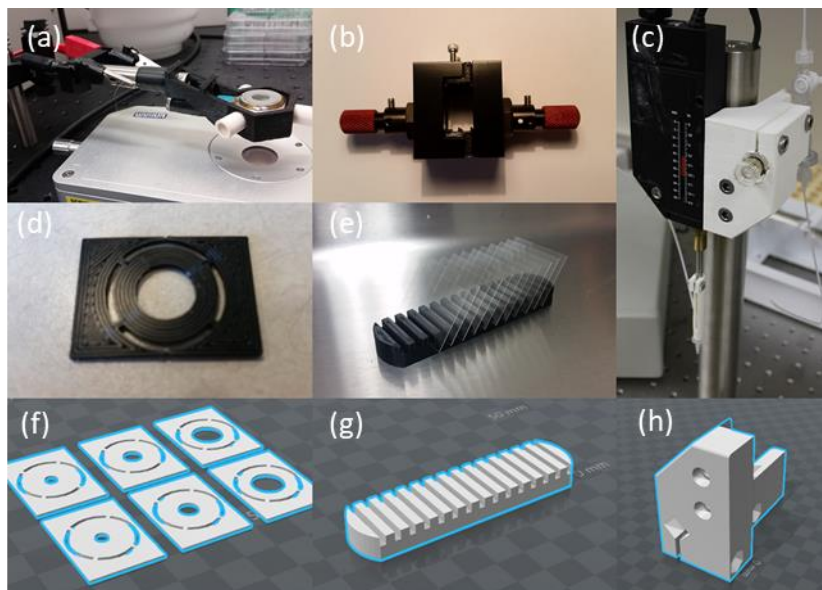


Figure A6. 3D printing has been used to engineer several pieces to help develop and optimize processes in this report. (a) Printed attachment to help control the evaporation rate of sessile drops. (b) 3D printed attachments are made to retrofit different linear variable filters with various filter holders (c) 3D printed components to a jig used to extract size-specific fractions after DGU. (d) A mask used in the process outlined in **Appendix B5**. (e) A glass cover slip holder; (f), (g), and (h) are images of the stereolithography or .stl files used to print (d), (e) and (c), respectively.

A5. Linear Variable Filters

Long pass filters are used to cutoff light below a certain wavelength. For instance, a 500 nm long pass filter will block light with a wavelength smaller than 500 nm while letting light with a wavelength greater than 500 nm pass. A short pass filter does just the opposite. A long pass LVF will let one adjust the wavelength cutoff based on the position of the beam along the length of the filter. As before, a short pass LVF will do just the opposite. When placing both a short pass and long pass LVF in series, a tunable band pass filter is thus created. Much like a monochromator, one can select distinct parts of a spectrum for more specific and detailed characterization. Although the resolution is not as good as a monochromator, a set of LVFs in series is more customizable, with the ability to create distinct band-passes with differing width and center locations.

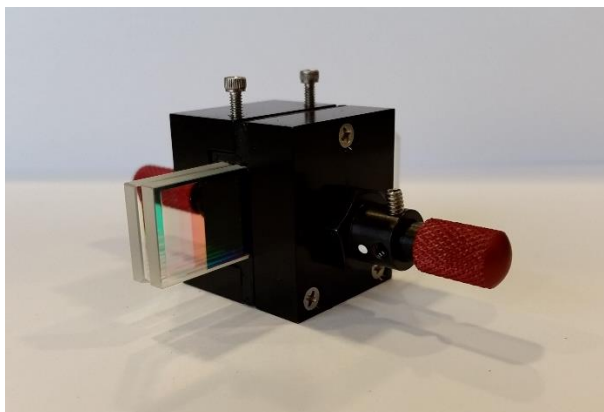


Figure A7. Linear variable filters in a retrofitted housing.

A6. Excitation Source

An excitation source is used to probe the sample and depends on the type of measurement that is desired. PL and lifetime measurements typically use a monochromatic high-energy Gaussian photon source to excite electrons into the valence band of a material and probe the excited state electron dynamics of the system. For a transmission or absorption measurement, the source

needs to span a broad range of wavelengths to measure the intensity before and after it passes through a material. The broader the source, the more information that can be obtained. **Figure A8** shows four of the main sources used in this report.

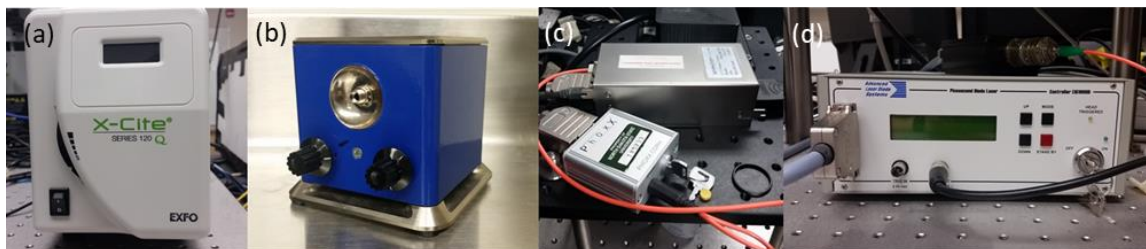


Figure A8. (a) The Xcite lamp produces broad-spectrum white light. (b) The blue housing excitation source can contain two different LED drivers, a blue 365 nm LED and a broad-spectrum white light. (c) The PhoxX 375 nm laser is typically used during quantum yield measurements, while (d) the pulse laser is used for lifetime measurements.

A7. Detector

The detector collects the signal after it has interacted with the sample. In this report, there are three main types of detectors, a spectrometer, a photomultiplier (PM) tube and a CCD camera. The spectrometer from **Figure A9** is used for three primary applications: PL, transmission, and QY measurements.



Figure A9. Fiber coupled spectrometer.

The PM tube imaged in **Figure A10** is used to calculate the lifetime of a sample.

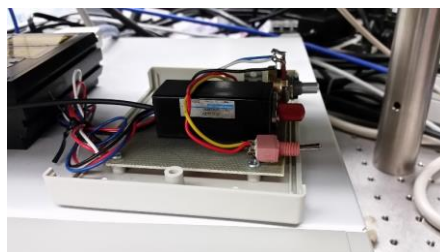


Figure A10. Photomultiplier tube used to measure a sample lifetime.

Two cameras are connected to the inverted microscope (standard and low-light) while one (standard) is connected to the upright microscope.

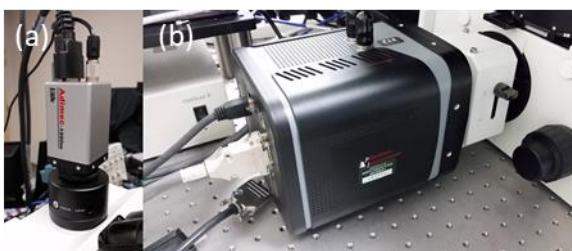


Figure A11. (a) Standard and (b) ProEM low-light resolution camera

APPENDIX B. METHODS AND PROCEDURES

The methods and procedures described in this section are intended for the operation and use of the instruments and equipment listed in **Appendix A**.

B1. Photoluminescence Measurement

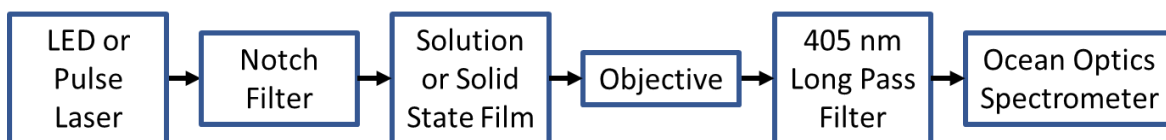






Figure B1. Light path for a photoluminescence measurement.

The following procedure outlines the basic setup and operation for measuring the PL.

- 1.) Ensure a proper set up with an LED or pulse laser coupled upstream of the sample in accordance with **Figure B1**. Note that for precise measurements, a notch filter should be placed after the excitation source and before the sample to eliminate any excitation source tail that bleeds past the downstream cutoff.
- 2.) Plug in the Spectrometer to start the cooling fan.
- 3.) Open the OceanOptics SpectraSuite software.
- 4.) Remove a dark background by clicking on the dark lightbulb  followed by the dark light bulb with a minus sign . Note that the lights should be off during this time.
- 5.) Start the camera software.
- 6.) With both software packages running, place the sample on the microscope stage and bring the sample into focus.
- 7.) With the sample in focus, direct the signal to the spectrometer.
- 8.) Turn on the excitation source and increase to the maximum desired power. The fluorescence peak should now be visible on the OceanOptics SpectraSuite software. Ensure that the signal does not saturate the detector.

- 9.) Maximize the signal by slightly adjusting the focus and changing the position of the sample.
- 10.) Once the signal is maximized, save the spectra. The spectra can be saved as a text file by clicking the button that looks like a brown disc  or by clicking the copy button  and pasting the raw data into an excel file.

B2. Lifetime Measurement

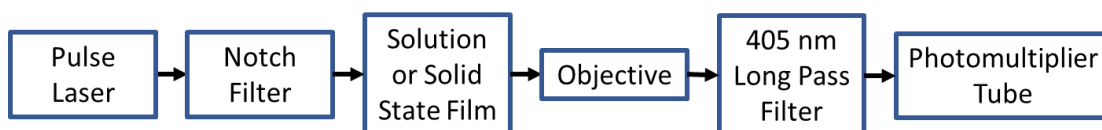


Figure B2. Light path for a lifetime measurement.

- 1.) First ensure a proper set up according to **Figure B1**. Note that a notch filter should always be placed after the excitation source and before the sample to eliminate any excitation source tail that bleeds past the long pass filter. This is important in lifetime measurements, especially when measuring nanosecond decays.
- 2.) In accordance with **B1**, maximize the PL of the sample in question using the pulsed laser with a power of up to 100 % (tune) and a modulation frequency of up to 1 MHz.
- 3.) With maximum fluorescence achieved, turn off the pulsed laser (or block its path to the sample) and close SpectraSuite and the camera software.
- 4.) Unplug the spectrometer.
- 5.) Switch the optical set up to **Figure B2** by changing the detector from the spectrometer to the PM tube.
- 6.) Set the pulsed laser to a power of up to 100% and 1 kHz repetition rate (Do not turn on yet). Note that this is a base frequency setting and can be changed for different experiments if necessary.

- 7.) Turn on the oscilloscope. This will also automatically turn on the LabView digital oscilloscope software.
- 8.) Within LabView select 'Add Step', 'Processing', 'Analog Signal' and 'Time averaging'
- 9.) On the right side select 'Tek TDS 1000/2000'.
- 10.) In this window select 'Horizontal'
- 11.) In the 'Horizontal' window change the scale and position to the appropriate time scale. For instance, a nanosecond decay can be accurately captured by setting the scale and position to 50 and 200 ns, respectively.
- 12.) On the right side select 'Time Averaging'.
- 13.) In this window change the 'Weighting Mode' to 'Linear' and the 'Number of ave.' to the desired duration in seconds i.e. for a 15-minute lifetime measurement enter 900.
- 14.) Click "Run" in the upper left corner.
- 15.) Once the software says, 'Waiting for Trigger', start the pulsed laser.
- 16.) To collect the data, under the 'Time Averaging' block right click 'time ave. signal'. Go to 'Export To' and then select the preferred location.

B3. Quantum Yield Measurement

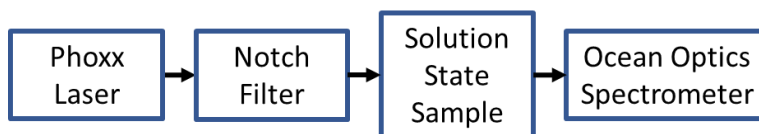


Figure B3. Light path for a quantum yield measurement. Note that the sample is inside of an integrating sphere.

Note: Steps 1 – 10, 14 – 15, and 17 – 24 are done on the upright microscope computer while steps 11 – 13 and 16 are done on the inverted microscope computer.

- 1.) Open OceanOptics SpectraSuite.

- 2.) Click “File”, “New”, “New Absolute Irradiance Measurement”.
- 3.) Select “Next Spectral Acquisition”.
- 4.) Select “Next”.
- 5.) Select “Next”.
- 6.) Select “Next”.
- 7.) Search and select the file LampPlacedonTop2.
- 8.) Click “Next”.
- 9.) Check “Using Integrating Sphere”.
- 10.) Click “Next”.
- 11.) Turn on the Phoxx Laser by turning the key.
- 12.) Open the Phoxx software package and turn on the laser.
- 13.) Select “Set Automatic” for the integration.
- 14.) Click “Next”.
- 15.) Turn Off Laser.
- 16.) Select “Store Dark Background”.
- 17.) Click “Next”.
- 18.) Place the reference sample under the integrating sphere and collect two baseline spectra,
B.
- 19.) Place the sample under the integrating sphere and collect two emission spectra, *S*. (Note:
Use the same volume and solvent in both the reference and emission samples.)
- 20.) To calculate the QY plot the following function:

$$f(\lambda) = \lambda(S_{average} - B_{average})$$

- 21.) In LoggerPro integrate $f(\lambda)$ over all positive values, giving the number of emitted photons, E .
- 22.) Also, in LoggerPro integrate $f(\lambda)$ over all negative values, giving the number of absorbed photons, A . (Note: the integrated absorption spectra will be negative so multiply by -1 to return a positive value.)
- 23.) Determine the QY by dividing the total number of emitted photons by the total number of absorbed photons, $QY = \frac{E}{A}$.

B4. Preparation of a Self-Assembled Monolayer

The following procedure describes the preparation of perfluorodecyltriethoxysilane coated slides.

- 1.) Clean a glass cover slips, using soap and deionized water.
- 2.) Thoroughly rinse the cover slip to ensure all soap has been removed.
- 3.) Dry the cover slip with nitrogen.
- 4.) Ensure that there is no visible debris on the glass slide. If debris is present repeat steps 1 – 3.
- 5.) Place clean dried cover slips on the tray as shown in **Figure B4** below.

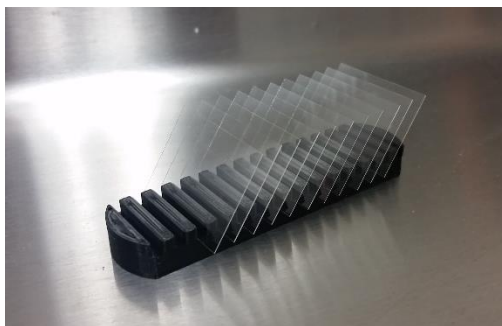


Figure B4. Tray to hold clean glass cover slips during self-assembled monolayer coating.

- 6.) Place the tray with cover slips in the desiccator containing a pool of perfluorodecyltriethoxysilane in the bottom.
- 7.) Pull to a vacuum of 15 – 20 mm Hg.
- 8.) Close the valve and place the desiccator under the hood and wait at least 8 hours for proper coating. Note it is best to do this at the end of the day and let the samples sit overnight.

The following procedure describes how to selectively remove different area of a SAM to dictate the wetting pattern. It will generally follow **Figure B5** below.

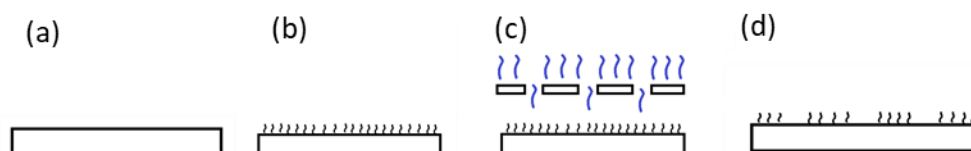


Figure B5. A (a) clean glass cover slip is coated with a (b) self-assembled monolayer. (c) Ultraviolet oxygen plasma exposure of a treated glass slide and mask will (d) effectively remove specific areas of the monolayer.

- 1.) Create a SAM slide according to the previous procedure.
- 2.) Place the SAM slide in the ultraviolet oxygen (UVO) plasma chamber.
- 3.) Place a mask on top of the SAM slide in the UVO chamber. Note: the mask can be just about anything ranging from loose change to laser cut Kapton masks.
- 4.) Gently close the UVO chamber door ensuring not to move the mask.
- 5.) Expose the glass slide to UVO plasma for at least 20 minutes.
- 6.) Once completed the patterned slide can be dip coated in various solvents revealing the SAM pattern, **Figure B6**.

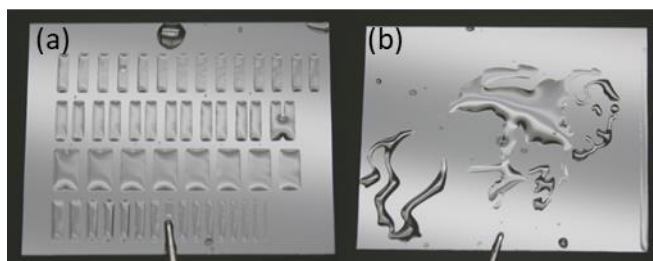


Figure B6. Patterned self-assembled monolayers on glass cover slips revealing a (a) series of lines and (b) the NDSU Bison mascot after dip coating in solvent.

B5. Density Gradient Ultracentrifugation

The following procedure describes the preparation and execution of a nanoparticle separation by density gradient ultracentrifugation.

- 1.) Turn on the ultracentrifuge (Switch on the right-side panel).
- 2.) Using the digital interface, set the centrifuge to precool at 0 °C.
- 3.) As the centrifuge is cooling, prepare the density gradient.

Note that the following instructions describe the preparation of a gradient for nonpolar nanoparticles using the Ti-41 rotor with a five-step density gradient of xylene and chloroform.

- 4.) Five stock solutions of various concentration of xylene and chloroform are made and stored (Stock solutions: 50 %, 60 %, 70 %, 80 %, and 90 % chloroform in xylene)
- 5.) Carefully prepare two gradients in two centrifuge tubes by layering 1.5 mL of each stock solution on top of one another, ensuring that the denser layer is on bottom. Note that letting the solvent run down the inside of the centrifuge tube works best in ensuring limited mixing at the layer interfaces of each stock solution.
- 6.) Carefully layer onto the top of the gradient the nanoparticle solution. Note that a typical nanoparticle volume and concentration to use is 0.300 mL and ~3 mg/mL, respectively.

- 7.) Measure the mass of the centrifuge tube, gradient and nanoparticles.
- 8.) Replace the centrifuge tube containing the nanoparticle with the blank gradient.
- 9.) Fill this gradient with enough solvent so that the blank and sample gradient match to 1/100th of a gram.
- 10.) Taking care to not disturb the sample, place it in the rotor bucket.
- 11.) Screw on the stainless-steel bucket top.
- 12.) Attach the bucket to the rotor. Note: gently press on the bucket ensuring it freely swings and is properly attached.
- 13.) Open the rotor chamber on the centrifuge by first releasing the vacuum (press the button labeled 'Vacuum' under the digital screen). Once the vacuum has been released open the chamber door.
- 14.) Carefully move the rotor into the chamber and onto the drive shaft.
- 15.) Once on the drive shaft slowly spin the rotor listening for a small click. Once the click is heard the rotor has been engaged.
- 16.) Close the rotor chamber door.
- 17.) Select the appropriate speed and duration using the touch display.
- 18.) Once the appropriate settings are made select "Enter" and then "Run".
- 19.) The centrifuge will begin to evacuate the rotor chamber as it ramps up to a speed of 3000 RPMs. The centrifuge will hold this speed of 3000 RPMs until the rotor chamber has been fully evacuated, and then it will accelerate to the set speed. Note that it is good practice to watch the centrifuge as it is accelerating to max speed to ensure a proper balance was achieved and minimal vibrations occur.

- 20.) The centrifuge will continue to spin until the selected time is complete or the “Stop” button is pressed.
- 21.) Once stopped, release the vacuum to the rotor chamber and open the rotor chamber door.
- 22.) Carefully remove the rotor and place on the counter.
- 23.) Carefully remove the bucket with centrifuge tube.
- 24.) Carefully remove the centrifuge tube.
- 25.) Once removed, place the centrifuge tube in the designated spot to separate into fractions.

APPENDIX C. MATHEMATICA DISCRETE EXPONENTIAL CODE

```
(*StretchedExponentialParameters*)
```

```
 $\beta := 0.88529$ 
```

```
Acc := 120
```

```
(*//ManyExponentialsParameters*)
```

```
LowerLimit := 0.68
```

```
UpperLimit := 0.73
```

```
Res := 0.01
```

```
 $\tau_{str} := 0.0000354968$ 
```

```
B := 0.000
```

```
(*ProbabilityDistributionFunction*)
```

```
P1[s_,  $\beta$ _] :=
```

$$\frac{1}{\pi} \sum_{n=1}^{\text{Acc}} ((-1)^{(n+1)} * \text{Gamma}[n * \beta + 1]) / (n! * s^{(n * \beta + 1)}) * \text{Sin}[n * \pi * \beta]$$

```
P2[s_,  $\beta$ _] :=
```

$$\frac{1}{\pi} \sum_{n=1}^{\text{Acc}} ((-1)^{(n+1)} * \text{Gamma}[n * \beta + 1]) / (n! * s^{(n * \beta + 1)}) * \text{Sin}[n * \pi * \beta]$$

```
P3[s_,  $\beta$ _] := 1/2 * (P1[s,  $\beta$ ] + Abs[P2[s,  $\beta$ ]])
```